Pore-Scale Transport Physics: Insights into Fluid Flow and Interfacial Dynamics

A Thesis submitted to

Indian Institute of Technology Guwahati

For the award of the degree

of

Doctor of Philosophy

by

Prateechee Padma Behera

(196103022)

under the supervision of

Dr. Pranab Kumar Mondal

And

Dr. Ravi Kumar Arun (IIT Jammu)

Department of Mechanical Engineering

Indian Institute of Technology Guwahati

Guwahati - 781039, India

May 2026

DECLARATION

May 2026

I, **Prateechee Padma Behera**, would like to declare that the thesis titled "**Pore-Scale Transport Physics: Insights into Fluid Flow and Interfacial Dynamics"** submitted to "**Indian Institute of Technology Guwahati**" for the degree of "**Doctor of Philosophy**" is a work of pure authenticity carried out under the supervision of **Dr. Pranab Kumar Mondal and Dr. Ravi Kumar Arun (IIT Jammu)**. To the best of my knowledge, the content of this thesis has not been submitted elsewhere for a degree. The contents of this thesis are free from any act of plagiarism. The investigations and observations reported in this thesis are carried out in the Department of Mechanical Engineering, Indian Institute of Technology Guwahati, during the period of July 2019 to January 2026.

Prateechee Padma Behera (196103022),
Research Scholar,
Department of Mechanical Engineering,
Indian Institute of Technology Guwahati,
Guwahati-781039, Assam, India.

CERTIFICATE

It is certified that the work contained in the thesis entitled "**Pore-Scale Transport Physics: Insights into Fluid Flow and Interfacial Dynamics**" by **Prateechee Padma Behera** (Registration no. 196103022) has been carried out under my supervision and that this work has not been submitted elsewhere for a degree.

Dr. Pranab Kumar Mondal,
Associate Professor,
Department of Mechanical Engineering,
Indian Institute of Technology Guwahati,
Guwahati-781039, Assam, India.

Dr. Ravi Kumar Arun
Associate Professor,
Department of Chemical Engineering,
Indian Institute of Technology, Jammu,
Jammu & Kashmir-181221, India.

Date: May 2026
Place: Guwahati

Above all, I bow in reverence to Thakur Maharaj, for His divine guidance and for granting me strength and perseverance through every difficult phase of this journey. JAYAGURU.

This thesis is dedicated to my Maa, Baba, Aja, Aayi, Bhai(s), my husband and all my family members for their constant support, encouragement, and motivation throughout this journey.

ACKNOWLEDGEMENT

I would like to express my sincere appreciation to all those who supported me throughout the long and challenging journey of my Ph.D. I was fortunate to receive guidance, encouragement, and motivation from many individuals, whose academic insights, thoughtful discussions, moral support, and presence during difficult times left a lasting impact on my journey. While it is not possible to acknowledge everyone individually, I take this opportunity to mention a few who stood by me at the forefront during my doctoral research at the Indian Institute of Technology Guwahati.

I am deeply thankful to my thesis supervisor, **Dr. Pranab Kumar Mondal**, and my co-supervisor, **Dr. Ravi Kumar Arun** (IIT Jammu), for their immeasurable guidance, invaluable technical advice, and emphasis on critical thinking. Their ideas and thought processes significantly shaped the methodology and outcomes of my research. The independent yet competitive research environment fostered under their mentorship enriched my academic experience and contributed profoundly to my personal and professional growth.

I sincerely thank my doctoral committee chairman, **Dr. Niranjan Sahoo**, and committee members, **Dr. Bhaskar Kumar** and **Dr. Rishikesh D. Kulkarni**, for their constructive criticism and valuable suggestions throughout my research work.

I extend my sincere thanks to Dr. Sumit Kumar Mehta (NPDF) for his constant guidance, mentorship, and support during critical stages of my research, and for his patience and thoughtful advice.

I am grateful to the Department of Mechanical Engineering, IIT Guwahati, for providing excellent research facilities and a conducive working environment. I also acknowledge the support of the staff of the Central Workshop; Mr. Saiffuddin Ahmed (Materials Science Laboratory, ME); Dr. Deepmoni Deka and Mr. Kaustubh Rakshit (Analytical Lab, Centre for the Environment); and the staff of the Analytical Laboratory, Department of Chemical Engineering, for their assistance with experimental work.

I would like to thank my friends Rupresha, Shivani, Apoorva, Onkar, Abhishek, Suraj, Arman, Nikhil, Rahul, Ashok, Bhavesh, Samrat, Giridhar, Chandan, Monika, Jenny, Dhruv, Rameswar, Puspita, Naina, Shipra, Gargi, and Himanshi for their constant encouragement and companionship throughout this journey. I am especially grateful to my seniors, Dr. Shweta and Dr. Swarna, for their unwavering support, motivation, and encouragement, and I sincerely appreciate their patience and willingness to listen whenever I needed support. I also thank my Odia family, Aparimita Di, Sunil Bhai, Kabita Di, Priyabrata Bhai, Tapashi, Subhashree, Siddharth, Dhrutiman, Amrit, Limashree, Soumya, and Anandita for creating a warm and supportive environment on campus. I further extend my sincere thanks to my seniors, lab mates, and juniors for their insightful discussions, valuable suggestions, and unwavering support. A special mention to my best friend, Rituparna, and BTS, whose healing words and music provided comfort and strength during a crucial period of my journey.

I owe my deepest affection and respect to my parents, Mrs. Laxmipriya Behera and Mr. Pravakar Behera; my grandparents; my brothers, Pradatta, Neptune, and Dipak; my husband, Dr. Bikash R. Behera; my aunt, Mrs. Kanaklata Sahoo; and all my family members for their unconditional love, sacrifices, and unwavering encouragement. Their blessings have been the foundation of my perseverance and success.

Finally, I extend my appreciation to the Department of Mechanical Engineering and the institute for their consistent guidance and support, which were instrumental in the successful completion of this research.

Sincerely,
Prateechee Padma Behera
Indian Institute of Technology Guwahati

ABSTRACT

Capillary-driven transport in porous media is a crucial phenomenon that underpins various natural processes and technology applications, such as paper-based microfluidics, lateral flow assays, and cost-effective diagnostic platforms. Further studying the effects of solute concentration, multiphase dynamics, fluid rheology, and reaction-transport coupling on capillary imbibition on fibrous porous substrates is crucial for the methodical development of efficient paper-based devices. This dissertation systematically examines capillary transport phenomena in paper-based porous media through experiments, analytical modeling, and numerical simulations, focusing on permeability, immiscible pore-scale dynamics, non-Newtonian fluid behavior, and optimization of lateral flow assays.

The first objective emphasizes on concentration-dependent solute imbibition in gel blot paper. The capillary wicking of aqueous dye solutions at different concentrations is examined through both experimental and analytical methods employing a Brinkman-extended Darcy framework. A modified permeability equation is presented to incorporate solute-pore interactions, facilitating estimation of concentration-dependent effective permeability from empirical data. The findings indicate that both wicking length and permeability decrease at lower solute concentrations and increase at elevated concentrations, attributable to the competing influences of flow resistance and capillary pressure rise caused by pore obstruction. The utilization of thick paper substrates enables direct observation of the progressing fluid front, demonstrating clear changes in interfacial angle during imbibition. Capillary pressure and permeability parameters, dependent on saturation, are empirically determined using Brooks-Corey correlations and integrated into Richards' equation for numerical simulations. The predicted saturation levels demonstrate strong concordance with experimental findings, creating a solid foundation for modeling solute-driven imbibition in paper-based porous media.

The second objective addresses immiscible interfacial transport and passive generation of droplets in paper microfluidic systems. A cost-effective, external actuation free method for droplet generation has been devised utilizing a Y-shaped paper strip, wherein oil droplets are produced within a water and oil wicking medium via capillary action. Experiments are conducted by altering paper grade and inclination angle to investigate their impact on droplet size and transport. Capillary pressure of Grade 1 paper surpasses that of Grade 4 paper at elevated saturation levels, facilitating the generation of smaller droplets due to diminished pore size. Droplet generation proceeds via pore-scale

merging and elongation mechanisms influenced by water-induced capillary forces, while gravitational effects enhance droplet size homogeneity. Three unique regimes of temporal droplet generation were identified based on the behavior of capillary pressure dependent on saturation. The temporal stability of the generated droplets has been established, indicating that they are useful for chemical and biological studies including micro- and nanoscale analytes.

The third objective investigates the combined effect of fluid rheology and analyte entrapment on wicking behavior in paper-based lateral flow experiments employing NaCMC solutions and human blood as non-Newtonian fluids. Saturation-based numerical modeling is conducted with experimentally determined effective viscosity and Brooks-Corey parameters. Increasing NaCMC concentration results in augmented liquid entry pressure and increases the flow heterogeneity, alongside decreased wicking velocity and length. Raman spectroscopic study indicates that higher NaCMC concentrations lead to enhanced hydrogen bonding, as seen by increased hydroxyl group intensity, which significantly elevates the effective viscosity within the paper matrix. The effective viscosity ratio is observed to be below unity for reduced NaCMC concentrations over extended durations, attributed to predominant shear-thinning activity. Analyte trapping study reveals that diffusion and interception mostly govern particle retention while imbibition, whereas inertial processes are insignificant. Both diffusion and overall trapping efficiency demonstrate a non-monotonic relationship with NaCMC concentration, with increased concentrations resulting in lower ideal test-line positions on the test strip. In human blood, an increase in hematocrit decreases wicking velocity and length while augmenting effective viscosity, exhibiting non-monotonic temporal fluctuation. The optimal arrangement of test lines is established by a criterion based on the critical Damköhler number, offering quantitative design instructions for effective lateral flow experiments.

The fourth objective outlines the development and validation of a paper-based lateral flow assay for the quick, economical colorimetric identification of methanol in alcoholic drinks. A Grade 1 paper microfluidic strip with dry-stored chemical reagents is engineered for portable and straightforward testing. The detection of methanol is accomplished by a chromotropic acid-based colorimetric technique, resulting in a pronounced purple colour. Experimental validation confirms accurate detection of methanol concentrations between 5% and 30% (v/v) utilizing minimal sample volumes. Integrated experimental and numerical analyses are performed to investigate wicking dynamics and reaction kinetics, resulting in the development of a normalized colorimetric

index for methanol measurement. The index has been verified through the use of both branded and locally manufactured alcoholic beverages, validating the dependability of the suggested detection method.

This dissertation offers a comprehensive knowledge of capillary transport in paper-based porous media by correlating pore-scale physics with device-level performance. The results provide empirically based design principles for paper microfluidic devices and lateral flow assays that manage non-Newtonian fluids, multiphase transport, and integrated reaction-transport processes.

LIST OF ABBREVIATIONS AND SYMBOLS

Abbreviations

SEM	Scanning electron microscope
LFA	Lateral flow assay
NaCMC	Sodium Carboxyl-methyl cellulose
PARDISO	PARallel DIrect SOlver

English symbols

K	permeability of porous media
G	pressure gradient in x-direction
U	velocity in x-direction
y	vertical axis
x	horizontal axis
t	time
h	thickness of the paper strip
$Uavg$	average velocity in x-direction
p_c	capillary pressure
p_{en}	entry pressure
r_p	pore radius
r_f	average fibre radius
p_f	final pressure
p_i	initial pressure
p	pressure
w	weight of the sample after every desired rpm
w_{dry}	dry weight of sample
r_1	nearest radius of rotation of centrifuge tube from axis of rotation
r_2	farthest radius of rotation of centrifuge tube from axis of rotation
$\boldsymbol{u}_i$	velocity field in numerical modelling for different phases *i*
k_{eq}	equivalent permeability of porous medium for the saturation level
$k_{rs_{e_i}}$	permeability ratio for the saturation level

p_{s_i}	pressure for the saturation level
$k_{rs_{e_w}}$	permeability ratio of wetting phase
$k_{rs_{e_n}}$	permeability ratio of non-wetting phase
F	Corrected concentration dependent constant
$(\overline{S_e})$	normalized saturation level
C_{NaCMC}	concentration of NaCMC solution
s_{e_i}	Saturation level
Pe	Peclet number
D	Diffusion coefficient
d_{pt}	particle diameter
d_p	Pore diameter
K_B	Boltzmann Constant
Da	Damköhler number
Y	Values of coefficient
Cn	Cahn number
Ca	Capillary number
M	Mobility
Bo_θ	Bond number
u_{ref}	Reference velocity
G	Chemical potential
R_i	Reaction rate
c_i	Concentration of species

Greek symbols

ϕ	Porosity of porous media
μ	Dynamic viscosity
ω	Angular velocity
λ_b	degree of heterogenity
η_B	Brownian trapping efficiency

η_I	interception trapping efficiency
η_{IN}	inertial trapping efficiency
η_o	overall theoretical trapping efficiency
α	trapping probability
μ_0	Zero shear rate viscosity
μ_∞	Infinite shear rate viscosity
λ	Relaxation time parameter
μ	Dynamic viscosity
ρ	Density
σ	Surface tension
$\dot{\gamma}$	Shear rate
φ	Phase field order parameter
Ψ	Free energy density
ε	Interface thickness
χ	Mobility tuning parameter

LIST OF FIGURES

LIST OF TABLES

CONTENTS

CHAPTER 1

INTRODUCTION AND LITERATURE REVIEW

This chapter provides an overview of paper-based microfluidics, its applications, and the fundamental role of capillary imbibition in enabling fluid transport in porous pathways. This is followed by a concise review of the literature reported in the domain of paper-based microfluidics. Subsequently, the aim, scope, and structure of the present thesis are outlined based on the insights gained from the literature review.

1.1. CAPILLARY IMBIBITION

Capillary-driven flow or capillarity is characterized by the movement of a wetting liquid spontaneously imbibed into pores under capillary pressure. This is a natural occurring phenomenon in porous systems and includes the rise of groundwater in soil (Bachmann *et al.* 2007; Tuller and Or 2004), oil displacement by brine in reservoir rock (Takahashi and Kovscek 2010; Yang *et al.* 2019), water transport in plant tissue (Bewley *et al.* 2013; Louf *et al.* 2018), and the diffusion of water into a fabrics/paper. Capillary imbibition is primarily governed by the microstructure of porous systems, interfacial tension, fluid properties, and fluid-solid interactions, and it plays a crucial role in multiphase flow through porous media. Indeed, for more than a century, the mechanisms of basic static and dynamic processes underlying capillary imbibition in porous systems have received ongoing attention in both engineering and basic sciences, including groundwater transportation, petroleum, and civil engineering as well as soil physics, engineering geology, and building materials.

1.2. PAPER MICROFLUIDICS

Paper as a substrate material has distinct advantages over conventional devices/systems comprising passive, power-free capillary transport of fluid, enhanced sensitivity in colorimetric detection owing to high surface area to volume ratio, and the capability to immobilize and store reagents in the fibrous matrix of the paper (Cate *et al.* 2015). The surface tension force at the liquid-air-pore interface acts as a driving force for the underlying flow in paper strips, causing induced capillary action (cf. Fig. 1.1 (a)) (Elizalde *et al.* 2015, 2016; Gillespie 1959; Patari and Mahapatra 2020a). Notably, paper-based fluidic assays have emerged as particularly advantageous for deployment in resource-limited or remote settings, as they exploit passive capillary-driven fluid transport, thereby eliminating the need for external power sources or bulky equipments (Yager *et al.* 2006).

High-performance field-deployable tests are required for public health diagnosis, veterinary medicine and environmental monitoring applications. A controlling factor in developing high-performance paper-based devices is the ability to manipulate fluid flow within the device configuration (Fu and Downs 2017). In 2007, Whitesides'(Martinez *et al.* 2007) achieved a major breakthrough by introducing paper patterned with photoresist for channel formation and the colorimetric detection of glucose and albumin. This innovation stimulated extensive research owing to the widespread availability of paper, the simplicity of patterning, and the capacity to facilitate fluid flow and reactions without the need for external power sources or instrumentation. Robust fluid control is necessary to functionalize paper as a substrate for quick diagnostic tests with optimum analytical performance (Byrnes *et al.* 2013). Researchers have worked on various modifications to enhance the functionality of paper-based analytical devices, including changes in channel geometry to adjust flow rates, network topology for sequential delivery of multiple fluids, on-switches or delays for flow regulation, and spatio-temporal controls for manipulating rehydrated reagents (Flow *et al.* 1905; Fu *et al.* 2012; Lutz *et al.* 2013; Mendez *et al.* 2010; Noh and Phillips 2010). Channel geometry is a key control parameter for fluid transport in paper-based devices. Modifying the width and length of porous paper pathways allows deliberate acceleration or retardation of fluid flow under wet-out conditions (Fu *et al.* 2010). Complex paper shaping has demonstrated success in regulating flow rates, as the addition of downstream fan-shaped structures after a rectangular strip facilitates quasi-stationary flow in lateral flow devices utilizing cellulose wicking pads (Mendez *et al.* 2010). In addition to single-channel geometric control, paper-based devices have been designed as interconnected networks, where multiple inlets converge at a common outlet to provide the automatic sequential delivery of various fluids to a detecting region. Sequential delivery has been accomplished with a Pseudo-1D paper network, including a linear porous strip coupled with several fluid-filled wells functioning as source reservoirs (Dharmaraja *et al.* 2013). Subsequent to these developments, paper-based technologies witnessed a rapid progress in device design, performance optimization, and widespread application (Cate *et al.* 2015; Kumar *et al.* 2016; Li *et al.* 2017).

Traditionally, the classical Lucas-Washburn equation (Dimitrov *et al.* 2007; Heiranian and Aluru 2022; Steinik *et al.* 2024) has been used to describe the wicking phenomena in paper-based porous media. Although the classical Lucas-Washburn model (Gorthi *et al.* 2020; Washburn 1921) is partially applicable for describing the capillary flow through bundles of tiny tubes, a fairly accurate mathematical model capturing the intricate flow

phenomenon in complex porous medium can be framed via Darcy's equation as well (Aminpour *et al.* 2018; Masoodi and Pillai 2010a). The L-W equations, which are appropriate for one-dimensional wicking phenomena, provide a description of time-dependent wicking length. On the other hand, Darcy's model connects the average fluid front velocity and pressure gradient in a fully saturated porous medium. Additionally, numerous studies have explored the dependency of the

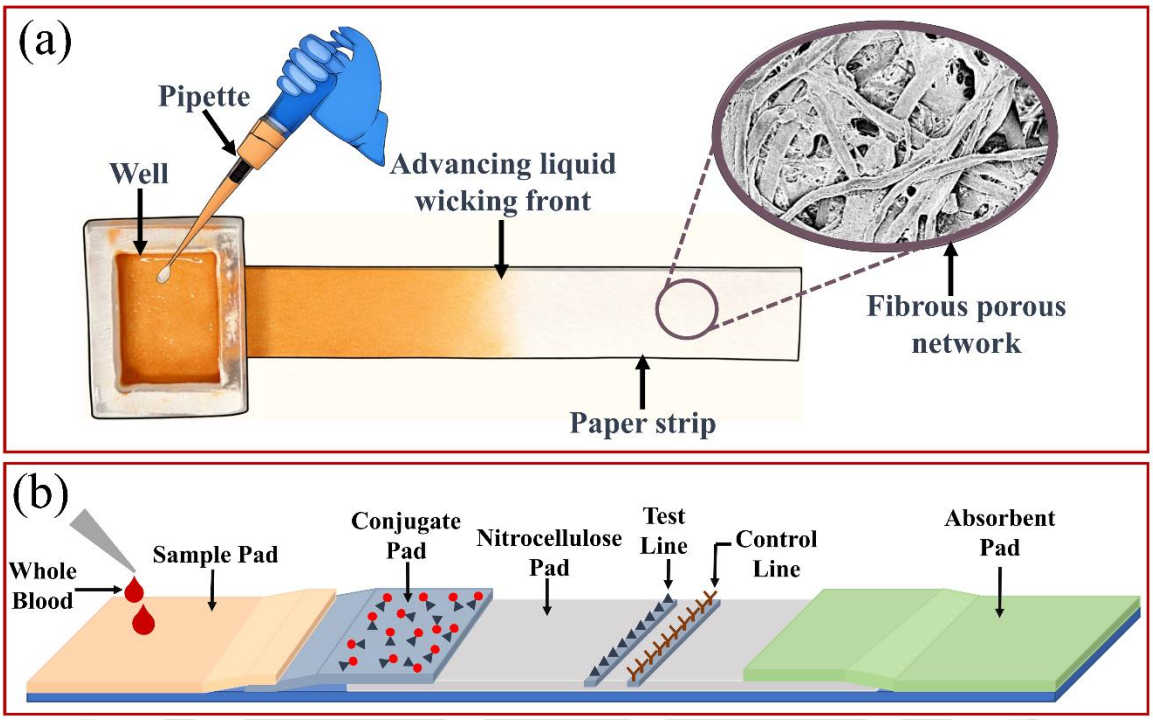

Figure 1.1. Schematic representation of (a) Capillary imbibition in a paper-based porous substrate, illustrating liquid dispensing at the intake and capillary-driven transport through the fibrous pore network, accompanied by a propagating wetting front; (b) A paper-based lateral flow assay (LFA), depicting the sample pad, conjugate pad, nitrocellulose membrane including test and control lines, and the absorbent pad, displaying capillary-driven lateral flow across specified assay regions.

-flow resistive term as both a linear and non-linear function of the velocity field using the Brinkman-Forchheimer extended Darcy equation (Hsu and Cheng 1990) . However, both the Lucas-Washburn and Darcy models are deemed valid for full saturation cases. It is worth to mention here that the capillary pressure in paper-based flow is highly dependent on the liquid saturation level, and it is because of the liquid saturation fraction dependent capillary pressure, the Richards model (Patari and Mahapatra 2020b) is deemed pertinent to predict the wicking phenomenon in paper-based porous media with a certain degree of accuracy. While the Lucas-Washburn equation has been reported to significantly overestimate the wicking length, results predicted by the Richards model closely align with experimental observations. For this part, the Brooks and Corey and van Genuchten models

(Hassler and Brunner 1945; van Genuchten 1980) are commonly used for establishing correlations between saturation level and capillary pressures from the experimental data. However, it is worth noting that the use of Richards' equation for simulating intricate porous materials is computationally expensive (Farthing and Ogden 2017).

1.3. LATERAL FLOW ASSAY (LFA)

A lateral flow assay (LFA) is a paper-based diagnostic tool engineered for the rapid and economical detection of target analytes in complicated samples, mostly utilized in point-of-care diagnostics and field environments (Hu *et al.* 2014; Ngom *et al.* 2010). Over the past few decades, the use of lateral flow assays for qualitative and quantitative diagnosis have expanded quickly and reached a relatively mature state of technology (Sajid *et al.* 2015). Their widespread usage can be attributed to advantages including reduced sample volume requirements, compact size, ease of operation and disease surveillance in both developing and developed countries (Wang *et al.* 2017). LFAs operate based on capillary-driven flow, wherein a liquid sample traverses laterally across a nitrocellulose membrane that has been modified with unique biorecognition components (Wong and Tse 2008). A standard LFA test strip comprises a sample pad for sample (and buffer) introduction, a conjugate pad containing detection reagents, an analytical membrane with immobilized test and control lines, and an absorbent pad for removal of excess fluid (cf. Fig. 1.1 (b)). The outcome of an LFA is typically determined by the optical signal produced at the test line (Bishop *et al.* 2019). The location of the test line where antigen-antibody interactions take place is a critical design variable for LFA. Note that efficient antigen-antibody interactions, which demands a judicial balance between the convective transport of the sample and reaction kinetics, is crucial for proper sample detection. The axial distance of the test line between the sample and conjugate pads directly influences reaction kinetics and the resultant signal strength. The ideal positioning of the test line is significantly affected by the capillary flow properties of the membrane: membranes exhibiting extended capillary flow times require the test line to be located nearer to the conjugate pad, while membranes with rapid flow necessitate relocating the test line further downstream (Ragavendar and Anmol 2012).

1.4. PERMEABILITY OF THE PAPER-BASED POROUS MEDIA

Permeability (K) within porous media depends on geometric factors, such as pore connectivity, pore size distribution, pore arrangement, and particle entrainment, transport,

and deposition within pore systems (Elrahmani *et al.* 2023; Erol *et al.* 2017; Pazdniakou and Adler 2013). Also, partial saturation during the flow of liquid inside the porous media affects the capillary pressure and the permeability of the porous material as the extent of saturation changes (Rath *et al.* 2018a). Van der Westhuizen and Prieur Du Plessis (1996) and Hommel *et al.* (2018) represented permeability of a porous medium on the scale of a representative elementary volume (REV), where an averaging concept is employed to make details of each pore's geometry non-essential. The effect of permeability on porosity was investigated by Masoodi and Pillai (2010b) and expressed the involved relations through several permeability models. The general form of the expression for permeability formulas is found as: $K = (2r_f)^2 f(\phi)$, where, r_f and $f(\phi)$ are fibre radius and function of porosity (ϕ) (Masoodi and Pillai 2010b; Rodriguez *et al.* 2004). It is noted that the expression for $f(\phi)$ is estimated using theoretical and empirical correlations, assuming porous structure as bundles of spherical particles and bundles of fibres. Moreover, the classical permeability expression, the Kozeny-Carman (KC) equation (Xu and Yu 2008): $K = \frac{\phi^3}{c(1-\phi)^2} S^2$, has been widely used for different types of porous media, as well as, for fibrous paper-based microfluidics. Here, c and S denote the Kozeny constant and the specific surface area based on the solid volume, respectively (Xu and Yu 2008). The value of c is found to be 2.5 for beds packed with spherical particles, however, for complex fibrous geometries, its values can be obtained experimentally. It is important to note that the KC equation is only suitable for isotropic fibrous materials. In this context, the expression for transverse permeability $\left(K = \frac{r_f^2 \pi \phi \left(1-\sqrt{1-\phi}\right)^2}{24(1-\phi)^{1.5}}\right)$, as established by Westhuizen, and Plessis (Van der Westhuizen and Prieur Du Plessis 1996), has been found to be suitable for random unidirectional porous matrices. Notably, this expression of transverse permeability is appropriate for studying the wicking phenomenon of water within filter papers (Liu *et al.* 2015). Furthermore, using numerical simulations, the influence of particle concentration on permeability in porous media featuring randomly arranged spherical pores has been investigated. It has been found that permeability decreases as particle concentration increases (Feng *et al.* 2020). Recently, the effect of suspended particle size on permeability in gravel and zeolite columns has been explored, and it was found that permeability increases as particle size increases (Tang *et al.* 2020). However, for the porous microfluidic papers-based media, no such attempt has been made yet.

1.5. SATURATION-BASED CAPILLARY PRESSURE IN PAPER-BASED POROUS MEDIA

In paper-based porous media, capillary pressure is defined as the pressure difference between the non-wetting and wetting phases and is inherently a function of wetting-phase saturation. The saturation of the wetting phase varies throughout the porous medium during fluid imbibition, resulting in a capillary pressure that is not spatially uniform but rather distributed over the pore network. Conventional interpretations of capillary pressure, represented by the Hassler-Brunner method, assume a static pressure-saturation relationship predicated on inlet circumstances, which may insufficiently represent the dynamic saturation and interface dispersion in heterogeneous paper-based substrates (Douglas Ruth; Sidney Wong 1991). The Hassler-Brunner model seems to be limited in its accuracy in estimating the capillary pressure in the centrifuge method, according to research by Xu *et al.* (2022). Instead, they proposed a more precise method for estimating saturation-based capillary pressure in centrifuges, known as the double integral method. According to the double integral approach, the saturation dependent capillary pressure can be represented as:(Xu *et al.* 2022) $p_c = \Delta\rho\omega^2\left(\frac{RL}{4} + \frac{5L^2}{72}\right)$, where, $\Delta\rho$ is the difference in the densities of wetting and non-wetting fluids. The parameters R and L represent characteristic length scales, corresponding respectively to the effective distance from the reference axis and the length of the porous domain under consideration. Researchers have performed experiments and developed analytical tool to estimate saturation-level dependent capillary pressure for describing wicking phenomenon in paper-based porous pathways (Rath *et al.* 2018b; Rath and Toley 2021; Verma and Toley 2024).

1.5.1. CENTRIFUGE METHOD

To examine capillary pressure as a function of liquid saturation in paper-based porous media, cellulose-based paper substrates such as Whatman Grade 1 and Grade 4 are commonly employed in strip geometries. These substrates can be saturated with single-phase liquids, such as Milli-Q water, as well as with immiscible two-phase systems, for example, mineral oil–water mixtures, to establish controlled saturation states. Centrifugal loading provides an effective means of imposing a spatially varying pressure field within the porous network, enabling systematic modulation of liquid saturation. The resulting liquid content within the paper substrate may be quantified gravimetrically, and the average saturation is defined as the fraction of pore volume occupied by the liquid phase relative to the fully saturated state. Such an approach allows capillary pressure–saturation

relationships to be examined in fibrous paper networks under well-defined saturation conditions. An increase in capillary pressure results in a corresponding decrease in wetting-phase saturation, thereby controlling the relative distribution of the two phases within the porous network. In the presence of an applied pressure field, capillary pressure exhibits spatial variation throughout the porous medium, leading to a non-uniform saturation profile. As a result, the saturation measured through experiments indicates an average value across the domain instead of a localized measurement, which requires an interpretation of capillary pressure–saturation relationships that is based on saturation averages (Ayappa *et al.* 1989).

1.5.2. BROOKS AND COREY MODEL PARAMETERS

The Brooks–Corey capillary pressure model has been shown to possess a theoretical foundation rooted in fractal descriptions of pore-space geometry (Li 2010). Furthermore, the following Brook and Corey correlation is an expression for the relationship between capillary pressure and normalized saturation ($\overline{S_e}$) (Hassler and Brunner 1945; van Genuchten 1980):$p_c = p_{en}\overline{S_e}^{-\frac{1}{\lambda_b}}$, where, the Brook and Corey model parameters are p_{en} and λ_b, termed as entry pressure when the fluid enters the porous medium displacing the air in the pores and the degree of heterogeneity, respectively. Capillary-driven flow under partial saturation in porous media is typically characterized by Richards' equation, which integrates Darcy's law with mass conservation principles to effectively describe liquid transport in conditions of partial saturation, considering the saturation-dependent characteristics of capillary pressure. The saturation-based Richards equation effectively models the nonlinear progression of wetting fronts, the redistribution of liquid, and transient wicking in paper substrates under specified external boundary conditions. Nonetheless, the governing equation remains open unless specific constitutive relationships that connect capillary pressure and permeability to saturation are defined. The Brooks-Corey model is commonly utilized due to its straightforward and physically relevant formulations for the capillary pressure–saturation relationship, along with the related saturation-dependent transport properties. The Brooks-Corey formulation, when integrated with Richards' equation, facilitates the depiction of saturation-driven flow dynamics, while maintaining responsiveness to variations in pore-size distribution and heterogeneity (Perez-Cruz *et al.* 2017b). Experimental data obtained from the centrifuge method are fitted to the Brooks-Corey model, providing a compact parameterization of saturation-dependent capillary behavior. These parameters are critical inputs for numerical models of partially

saturated flow, where they dictate the shape and slope of the capillary pressure versus saturation curve. This framework has been effectively expanded beyond soils to include fibrous porous materials, thereby enhancing its applicability for characterizing liquid imbibition in paper-based substrates (Gasperino *et al.* 2018a).

1.6. NON-NEWTONIAN FLUID FLOW IN POROUS MEDIA

Paper-based fluidic platforms are extensively utilized in point-of-care diagnostics, especially in lateral flow assays (LFAs) (Behera *et al.* 2023b; Spreinat *et al.* 2025), due to their straightforward design and manifolds benefits. Several diagnostic fluids used in LFAs demonstrate non-Newtonian rheological behavior. Among the non-Newtonian biofluids, shear thinning nature of blood is strongly influenced by the hematocrit level (Mehri *et al.* 2018), while saliva exhibits non-Newtonian behavior owing to the presence of a dilute polymer (mucin) solution with long entangled chains (Helton and Yager 2007; Schwarz 1987). On the other hand, polymeric solutions, such as NaCMC, utilized in the food and pharmaceutical industries have a non-Newtonian nature because of the long polymeric chains (Lopez *et al.* 2015). Considering promising potential of low-cost paper-based devices in applications mentioned above, it is imperative to understand the rheology modulated wicking phenomenon of bio-samples on the paper strips.The flow behavior of non-Newtonian fluids in porous media differs significantly from that of classical Newtonian fluids, attributed primarily to the influence of shear-rate-dependent viscosity and the geometric deformations occurring within the pore structure (Sochi 2010a). It may be mentioned here that Newtonian models are unable to account for the flow resistance instigated by the substantial stretching of fluid constituents caused by the converging–diverging geometry and tortuosity of pore networks. Consequently, it is necessary to extend and modify Darcy's law by incorporating a modified permeability and an apparent viscosity that are influenced by the flow behavior index and the properties of the porous medium to characterize non-Newtonian flow (Silva *et al.* 2016). Based on the Darcy's law, Wada et al. (WADA *et al.* 1985) first presented the modified Darcy law for non-Newtonian liquid flow in porous media. The experimental investigation by Comiti et al.(Comiti *et al.* 2000) suggests that the Darcy's law is even valid for the non-Newtonian liquid up to the critical pore Reynolds number ~ 4.3. In this context, it is noted that Brandão et al.(Brandão *et al.* 2021) provided the Darcy-Carreau-Yasuda rheological model for non-Newtonian fluid flow in porous media. They have defined effective apparent viscosity using the effective consistency index. Moreover, the viscosity of non-Newtonian liquid inside the complex

pore is very difficult to estimate because of its strong dependency on shear rate, which in turn, depends on the flow field. Jang et al.(Jang *et al.* 2025) demonstrated that the mobility factor of a non-Newtonian fluid in porous media, defined as the ratio of permeability to effective viscosity, analogous to the Newtonian liquid, as the ratio of permeability to constant viscosity. Research on non-Newtonian flows in porous media shows that the premise of effective viscosity arises from the heterogeneous distribution of deformation rates experienced by the fluid elements at the pore level (Eberhard *et al.* 2019; Jang *et al.* 2025). The effective viscosity can be explained as a spatially averaged measure derived from the viscosity fields at the pore scale, as it responds locally to the constitutive characteristics of the fluid (Eberhard *et al.* 2019). In this context, Pearson and Tardy (2002) emphasized that non-Newtonian effects in porous media cannot be accurately represented by a universal effective shear rate, as the apparent viscosity is highly dependent on pore geometry and flow configuration. It has been demonstrated that Darcy-scale behavior may also be influenced by residence-time effects, flow history, and pore-scale deformation modes, especially in the case of shear-thinning and viscoelastic fluids. Therefore, effective viscosity must be considered a parameter that depends on configuration, capturing the complexities of rheology at the pore scale, rather than being solely a function of bulk rheology.

1.7. ANALYTE TRAPPING MECHANISM IN POROUS MEDIA

The design of paper-based diagnostic devices requires a clear understanding of the transport of micron-sized interacting particles through the pores of porous paper substrates. In the context of lateral flow assays, detailed insight into particle-particle interactions and collisions is essential for effective control of species reactions. A longer residence time of the working sample in the porous pathway increases the probability of particle collisions and entrapment between reacting species, which improves reaction efficiency. From the perspective of transport phenomenon, the diffusive Péclet number, which represents the ratio of convective to diffusive transport, acts as a key scaling parameter for species transport governed by convection-diffusion during reactions. At sufficiently low diffusive Péclet numbers, transport is dominated by diffusion, whereas at higher values convection becomes the primary mode of species transport. Reactant species characterized by very high diffusive Péclet numbers generally experience reduced residence times, often resulting in inefficient reaction outcomes. In addition, the Damköhler number, defined as the ratio of the reaction rate to the characteristic flow rate, plays a critical role in determining reaction efficiency. Larger Damköhler numbers typically correspond to faster reaction

kinetics. Therefore, identifying conditions favorable for efficient reactions requires a thorough understanding of the coupled effects of advection, diffusion-driven transport, and trapping of colloidal reactants.

To account for particle transport and deposition under combined advective and diffusive mechanisms, colloid filtration theory (CFT) is commonly employed to analyze particle capture at the level of individual pores. Within this framework, Nelson and Ginn (2005) have examined analyte trapping at the pore scale by resolving particle trajectories near solid surfaces within the pore network using colloid filtration theory. These investigations demonstrated that analyte capture is governed by transport mechanisms such as Brownian diffusion, hydrodynamic retardation, and interception, and highlighted the dominant role of pore-scale geometry and residence time in determining trapping efficiency rather than size exclusion alone. Building on this pore-scale perspective, Wang *et al.* (2012) examined analyte entrapment in fibrous porous media by explicitly addressing the interplay between fluid flow and particle transport through a lattice-based numerical framework. Their findings showed that particle capture takes place via diffusion, interception, and inertial effects, while trapping efficiency varies dynamically as particles deposit on pore-scale solid surfaces. The results suggested that deposited particles alter the local pore geometry and flow pathways, which subsequently enhances trapping by increasing residence time and expanding capture zones. In line with these observations, Wang and Otani (2013) presented a comprehensive review of fibrous filtration approaches for nanoparticle removal from gas streams. The review emphasized the potential of multilayer fibrous filters as an effective and economical strategy for nanoparticle capture. It was further highlighted that nonwoven filters composed of fibers with distributed diameters exhibit superior filtration performance compared to filters with uniform fiber sizes. Gasperino *et al.* (2018b) highlighted the importance of particle trapping in enhancing the sensitivity of lateral flow assays and demonstrated that colloidal particles employed in such assays exhibit distinct transport characteristics within paper-based porous substrates. The study noted that much of the theoretical basis for describing particle transport in porous media originates from hydrogeological research. In this regard, colloid filtration theory (CFT) was emphasized as a framework that incorporates both mechanistic and empirical considerations to describe particle binding. Unlike mass-action kinetics, which assumes a constant association rate for particle attachment to pore surfaces, CFT accounts explicitly for factors such as particle size, pore geometry, and flow conditions. Through this approach, CFT offers valuable insight into particle trapping dynamics and the interactions between

analytes or colloids and paper-based porous media. Such understanding is crucial for optimizing residence time during interactions between the sample and dry-stored reagents, thereby enabling the development of highly sensitive lateral flow assays. Overall, trapping efficiency plays a key role in determining particle attachment behavior in lateral flow assays, as it quantifies the probability of particle adhesion to pore surfaces and is typically evaluated using normalized concentration fields. Despite aforementioned progress in the field, numerical investigations exploring particle trapping mechanisms in detail remain relatively limited (Boccardo *et al.* 2014; Fan *et al.* 2022; Gasperino *et al.* 2018b).

In this framework, particle trapping in porous media is commonly interpreted in terms of a limited number of fundamental physical mechanisms that govern particle-pore interactions during transport. In paper-based porous media, particle trapping arises from three dominant mechanisms: diffusion-based trapping, interception and inertial impaction. Diffusion-based trapping originates from the stochastic thermal motion of particles, which promotes contact with pore surfaces, particularly for small particles and low transport velocities. Interception occurs when particles following streamlines come into contact with pore walls due to their finite size relative to the pore dimensions, resulting in the formation of a capture region upstream of the pore. The third mechanism, inertial impact, becomes significant when particles possess sufficient inertia to deviate from streamlines and collide with pore walls. Together, these mechanisms provide a comprehensive physical basis for describing particle trapping behavior in porous media under combined advective and diffusive transport conditions (Nelson and Ginn 2005; Payen *et al.* 2012; Wang and Otani 2013; Wang *et al.* 2012b).

1.8. DROPLET GENERATION IN POROUS MEDIA

Confining reactions within discrete droplets provide multiple benefits. Droplets act as isolated reaction compartments and are often monodisperse, enabling quantitative analysis and rapid processing of very small volumes, including single cells or molecules (De Jonghe *et al.* 2023). Micro- and nanoscale droplets are gaining significance in various domains, including material synthesis (Banerjee *et al.* 2021; Xiong *et al.* 2021), chemical engineering (Bai *et al.* 2020; Meissner *et al.* 2017; Michelin 2023), medical diagnostics (Ahmed *et al.* 2023; Li *et al.* 2021; Zec *et al.* 2014), cellular research (Ai *et al.* 2020; Bashirzadeh and Liu 2019; Palit *et al.* 2018; Xi *et al.* 2023), pharmaceuticals (Cun *et al.* 2021), food industry (Ding *et al.* 2020; Goudappel *et al.* 2001) and enhanced oil recovery (Lu *et al.* 2018). Their elevated surface-to-volume ratio and smaller size significantly enhance reaction rates,

improve heat transfer efficiency, facilitate high-throughput parallel studies, and reduce reagent consumption. Microfluidic technology enables the reproducible generation of such droplets and allows for the exploration of complex fluidic interactions under precisely controlled conditions (Kaneelil *et al.* 2024; Malik *et al.* 2024; Paul *et al.* 2024; Satpathi *et al.* 2024; Yadav and Pathak 2024). The micro-sized water droplets have been generated in the T-junction geometries. At a capillary number on the order of $\sim 10^{-2}$, the dominant droplet breaking mechanism shifts from pressure-dominated to shear-dominated.(Garstecki *et al.* 2006) The polydimethylsiloxane (PDMS) based diverging microfluidic device, fabricated through oxygen plasma treatment, have demonstrated the ability to produce monodispersed droplets.(Tan *et al.* 2006) The utilization of diverging passages results in alterations in both velocity and pressure gradient, enabling precise localization of droplet generation points for subsequent fusion or sorting. Avraam and Payatakes (1995) observed that the drop-traffic flow regime exists for chamber and throat type glass porous medium with capillary numbers in the order of $\sim 10^{-5}$ with lower water saturation levels. Beyond channel-based microfluidic systems, droplets can also be generated intrinsically within porous media through capillary-driven instabilities associated with pore-scale geometry. Early theoretical and experimental work by Roof (1970) demonstrated that when a non-wetting fluid emerges from a water-wet pore throat into a larger pore body, interfacial forces may cause the fluid to undergo snap-off, leading to droplet formation. The energy balance criterion by Roof suggests that the droplet snaps off from the liquid stream at the throat of the geometry when the curvature of growing droplet's radius becomes twice the radius of the throat, highlighting the dominant role of pore geometry and capillary pressure distribution. Such findings establish porous media as passive droplet generators, where breakup is governed by geometric and interfacial conditions rather than external flow control. Subsequent pore-scale investigations by Armstrong *et al.* (2016) further examined droplet breakup and snap-off phenomena in constricted geometries representative of porous media. Using numerical simulations capable of resolving interfacial dynamics, the study demonstrated that droplet snap-off occurs preferentially at pore constrictions and is strongly governed by local capillary pressure variations imposed by the geometry. The results showed that the onset of snap-off and the resulting droplet size are consistent with the Roof criterion, while also indicating that dynamic effects such as viscous and inertial stresses can influence the breakup process under flowing conditions. To address the high costs associated with conventional microchannel-based droplet generation, paper-based porous substrates offer a promising alternative. The interconnected fibrous network of microscale

pores within paper substrates can promote breakup of the dispersed phase during capillary-driven wicking of the continuous phase (Behera *et al.* 2023c, 2024; Patari *et al.* 2023; Rath *et al.* 2018b).

1.9. MOTIVATION AND RESEARCH GAP IN THE EXISTING LITERATURE

Capillary-driven flow in paper-based porous media has been widely employed for low-cost microfluidic applications due to its self-driven nature, ease of fabrication, and suitability for chemical and biological assays (Asadi *et al.* 2022; McClure *et al.* 2020; Tokihiro *et al.* 2023). Prior studies have primarily focused on modeling imbibition in paper using classical frameworks such as the Lucas–Washburn equation, Darcy's law, and saturation-based formulations (Kumar *et al.* 2019; Mehrabian *et al.* 2011; Patari *et al.* 2023). However, experimental observations indicate that the presence of species within the working fluid can substantially influence the wicking dynamics by altering effective pore radius and flow resistance. In thicker paper substrates, enhanced liquid–solid interaction leads to measurable variations in wicking length and effective permeability with changing solute concentration. Despite these observations, the permeability of paper is often treated as a constant property in existing models, neglecting its dependence on species concentration. Furthermore, saturation-dependent flow modeling in paper-based systems requires accurate estimation of capillary pressure and permeability parameters, which are not readily available for aqueous solutions with species. Experimental determination of these parameters and their incorporation into analytical and numerical frameworks remain obscure and limited. Furthermore, non-uniform interfacial advancement produced by pore-scale trapping and concentration-induced changes in effective pore radius is observed by visualizing the fluid front within thicker paper; these phenomena are not sufficiently represented by traditional one-dimensional models. These limitations motivate the need for a systematic investigation of concentration-dependent permeability, saturation-based flow behavior, and capillary-driven imbibition in paper substrates following combined efforts of experimental investigations, analytical methodology, and numerical simulations.

In addition to solute effects, capillary-driven transport in paper often involves non-Newtonian fluids and multiphase systems that exhibit complex pore-scale dynamics. Many biologically relevant fluids, including polymer solutions and blood, demonstrate shear-dependent viscosity, which directly affects imbibition velocity, saturation evolution, and residence time within the porous network. Existing studies have shown that non-Newtonian rheology alters effective viscosity during wicking, yet a generalized framework to describe

rheology-modulated imbibition in paper-based porous media remains incomplete. Additionally, capillary-driven flow in paper with two immiscible fluid phases can induce interfacial phenomena such as droplet breakdown, snap-off, and entrapment, facilitating passive droplet generation without requiring external force. These processes, although well studied considering rigid microchannels, have received limited focus from the perspective of fibrous paper substrates. The lack of low-cost platforms for controlled pore-scale multiphase transport in paper pathways represents a notable gap. Furthermore, while paper-based lateral flow assays are extensively used for point-of-care detection and biochemical analysis, their design often relies on empirical placement of reaction zones and test lines. Experimental and numerical studies indicate that flow velocity, saturation, and species residence time strongly govern reaction kinetics and colorimetric signal development. However, the integration of transport physics with assay design, including optimized reagent storage and index-based quantification, has not been comprehensively addressed. For advanced applications that demand multiplexing capability, enhanced sensitivity, quantitative readout, and user-friendly operation, the individual components of paper-based microfluidic systems require further technological refinement. Consequently, a deeper understanding of species transport mechanisms in aqueous media is essential to enable rational design and optimization of paper-based microfluidic platforms, including lateral flow assays (Kim *et al.* 2015; Mahmoudi *et al.* 2019; Tang *et al.* 2024).

1.10. AIM OF THE PRESENT WORK AND PROBLEM DEFINITIONS

From the preceding discussion, it is evident that current understanding of capillary-driven transport in paper-based porous media remains limited to practical operating conditions from classical models. The effects of analyte mobility, non-Newtonian rheology, and pore-scale immiscible transport on wicking dynamics remain insufficiently understood. Accordingly, the present work aims to systematically investigate concentration-dependent permeability, rheology-modulated imbibition, and capillary-driven multiphase phenomena in paper substrates, and to translate these insights into the rational design and optimization of paper-based microfluidic devices. Following this reasoning, the scope of the present dissertation is outlined below:

1.10.1. Experimental, analytical and numerical investigation of solute-driven imbibition with concentration-dependent permeability in paper-based porous media

The main goals of this first objective are to examine the concentration-dependent wicking behavior and evaluate the concentration-dependent permeability employing both

theoretical models and experimental data. Experiments are conducted on thicker gel blot paper using aqueous food dye solutions at varying concentrations. The temporal evolution of the wicking length is analytically obtained using a Brinkman-extended Darcy formulation, incorporating an effective permeability derived from a modified rectangular unidirectional fiber cell model. In addition, saturation-dependent capillary pressure and permeability are determined experimentally through concentration-dependent Brooks–Corey parameters. These parameters are subsequently employed in numerical simulations based on the Richards equation to describe saturation-dependent flow behavior in thick paper substrates.

1.10.2. Experimental and numerical investigation of capillary-driven low-cost droplet generation in Y-shaped paper-based porous media

In the second objective, we have devised a low-cost droplet-generation method using a Y-shaped paper strip. To study oil droplet generation in a water-wicking medium, we conducted experiments by varying the paper grade (1 and 4) and the strip inclination. Microscopic droplets are generated within the pores and transported to the outlet through two primary mechanisms involving capillary-driven merging and elongation of oil droplets under water imbibition. Gravitational effects significantly reduce droplet size while maintaining high uniformity. Three distinct regimes of temporal droplet generation are identified based on saturation-dependent capillary pressure patterns. Droplet size is strongly influenced by the paper type, with Grade 1 paper producing smaller droplets due to its finer pore structure. Finally, the temporal stability of the generated droplets is established, highlighting their relevance for cellular research.

1.10.3. Experimental and saturation-based numerical investigation into rheology-driven wicking dynamics and analyte trapping in paper-based lateral flow assays

In the third objective, we experimentally investigate the effect of fluid rheology on wicking dynamics in paper-based lateral flow assay (LFA) using both NaCMC-water solution and human blood. We develop a saturation-based numerical framework to simulate the wicking phenomenon in paper-based porous strip using experimentally estimated effective viscosity of the solution. Increasing NaCMC concentration increases liquid entry pressure and flow heterogeneity, thereby reducing average wicking length and imbibition velocity. Higher NaCMC concentrations at lower axial positions enhance trapping efficiency and probability. For human blood, both wicking length and average velocity

decrease with increasing hematocrit, while effective viscosity may exhibit non-monotonic temporal variation. An optimum design guideline for efficient reactions in lateral flow assays has also been identified.

1.10.4. Development and validation of a low-cost paper-based microfluidic platform for colorimetric methanol detection in alcoholic beverages

The fourth objective reports a Grade 1 paper-based fluidic device for rapid, sensitive, and cost-effective methanol detection in alcoholic beverages using a colorimetric reaction involving potassium permanganate, sulphuric acid, sodium bisulphite, and chromotropic acid. The reaction with methanol produces a distinct purple color that can be visually assessed or quantified. Experimental results confirm detection of methanol concentrations from 5 % to 30 % (v/v), encompassing levels associated with methanol poisoning. Besides, numerical simulations support the development of a colorimetric index for this concentration range, which is further validated using both branded and locally produced alcoholic beverages.

1.11. OUTLINE OF THE THESIS

The subsequent chapters of the thesis are organized as follows:

- Chapter 2 presents an experimental, analytical, and numerical investigation of concentration-dependent capillary wicking in thick gel blot paper, focusing on effective permeability estimation and saturation-dependent flow modeling.
- Chapter 3 investigates capillary-driven immiscible oil–water transport in paper-based porous media, revealing pore-scale droplet breakup, snap-off, trapping, and transport mechanisms, and demonstrating low-cost passive droplet generation using graded paper substrates.
- Chapter 4 examines rheology-modulated wicking and analyte trapping in paper strips using both NaCMC solutions and human blood, leveraging experiments, effective viscosity estimation, saturation-based modeling, and design guidelines for optimized lateral flow assay performance.
- Chapter 5 presents the development of a Grade 1 paper-based lateral flow assay for colorimetric detection and quantification of methanol in alcoholic beverages, integrating experiments and numerical modeling to establish a reliable index-based readout.

- Chapter 6 concisely summarizes the principal findings from all of the chapters and also underscores prospective paths for further research relevant to the current thesis.

CHAPTER 2

EXPERIMENTAL, ANALYTICAL AND NUMERICAL INVESTIGATION OF SOLUTE-DRIVEN IMBIBITION WITH CONCENTRATION-DEPENDENT PERMEABILITY IN PAPER-BASED POROUS MEDIA

In this chapter, solute-driven capillary imbibition in paper-based porous media is investigated experimentally, analytically, and numerically, with a focus on concentration-dependent permeability. The significance of solute concentration on wicking dynamics, effective permeability, and interfacial behavior is investigated through controlled experiments. Bases on the Brinkman-extended Darcy framework, an analytical model is developed and validated. A Richards-equation-based computational model incorporates experimentally measured saturation-dependent capillary pressure and permeability, enabling multiscale insights into saturation transport and permeability evolution pertinent to paper-based microfluidic applications.

2.1. OBJECTIVE

Paper-based microfluidic devices have garnered significant interest as cost-effective and rapid diagnostic platforms for investigating interactions between analytes transported through fibrous porous media (Asadi *et al.* 2022; McClure *et al.* 2020; Tokihiro *et al.* 2023). Fluid movement in these devices is facilitated by capillary action due to surface tension forces, displacing the necessity for external actuation (Arun *et al.* 2016; He *et al.* 2022; Kim *et al.* 2020; Lee *et al.* 2016; Narayanamurthy *et al.* 2020). Due to benefits like ease of manufacture, biocompatibility, portability, and cost-effectiveness, paper-based microfluidics have been extensively employed in diagnostics, environmental monitoring, and food safety. The porous paper matrix provides as an efficient medium for analyte transport and interaction, indicating that the species in the carrier liquid can substantially affect the flow behavior (Chang *et al.* 2023; Hao and Cheng 2010; Shi *et al.* 2023; Vasheghani Farahani and Mousavi Nezhad 2022).[1]

Capillary-driven wicking on paper substrates is conventionally explained by the Lucas–Washburn equation and Darcy's law; however, both are applicable mainly at fully

[1] Contents of this chapter is published in the journal of **Physics of Fluids (AIP), Volume 35, Issue 12, Page 122007, December 2023**, https://doi.org/10.1063/5.0177100

saturated situation (Kumar *et al.* 2019; Mehrabian *et al.* 2011; Patari *et al.* 2023). Given that capillary pressure and permeability are significantly influenced by saturation, the Richards equation offers a more suitable framework for simulating wicking in partially saturated paper-based porous media. The Brooks–Corey model is frequently utilized to characterize saturation-dependent capillary pressure and permeability. Permeability is impacted by pore geometry, porosity, particle movement, and partial saturation, and it is frequently described by averaged models like the Kozeny-Carman formulation or transverse permeability expressions for fibrous media.

After a thorough review of the literature, it has become evident that the concentration-dependent permeability of microfluidics paper for various species has not been estimated in the open literature. Additionally, there is no equivalent mathematical model for describing the concentration-dependent wicking behavior of microfluidic paper. Moreover, the relevant concentration-dependent model parameters for Richards' equation, which simulates saturation-dependent flow within paper-based porous media, are also lacking in available literature. The primary objective of this work is to determine the concentration-dependent permeability using experimental data and a theoretical framework utilizing the Brinkman-extended Darcy model. Subsequently, we calculate the saturation-dependent capillary pressure using the Brooks and Corey model and perform numerical simulations while solving the Richards equation. Thicker gel blot paper is intentionally utilized to augment species interaction and enhance the observation of the wicking process.

2.2. MATHEMATICAL MODELLING

In the present work, we investigate the flow of a Newtonian liquid through a single strip of gel-blot paper, assuming incompressible fluid flow. The porous structure of the gel-blot paper is modelled using the Brinkman-Forchheimer extended Darcy model (Hsu and Cheng 1990). Assuming of steady, fully developed, unidirectional flow along the strip, with velocity variation only across the transverse direction, the governing momentum equation reduces to the following one-dimensional form:

$$\frac{\mu}{\phi}\frac{d^2U}{dy^2} - \frac{\mu}{K}U - \frac{C_f \rho U^2}{\sqrt{K}} - \frac{dp}{dx} = 0 \qquad (2.1)$$

Here, the permeability of porous media, porosity, intrinsically averaged pressure and liquid dynamic viscosity are represented by the symbols K, ϕ, p and μ, respectively; C_f is the Forchheimer coefficient and $\frac{dp}{dx}$ is pressure gradient in *x*-direction. The first term represents the Brinkman viscous diffusion accounting for shear effects within the porous structure,

the second term denotes the Darcy viscous resistance offered by the porous matrix, and the third term corresponds to the nonlinear Forchheimer drag, which represents the inertial resistance to flow in a porous medium and arises as a quadratic correction to Darcy's law at higher flow velocities.

The Reynolds number is estimated to be very low (Re << 1) for the characteristic length scale of 0.8 mm and a very low flow velocity (10^{-5} m/s) in a paper-based porous medium (Gaikwad *et al.* 2017a). Consequently, the convective term is neglected in the momentum equation. Additionally, under these conditions, inertial effects are negligible compared to viscous forces, and the quadratic Forchheimer term contributes insignificantly to the overall flow resistance of the porous medium. Therefore, this term is neglected in the present analysis.

Based on these assumptions, we approximate the transport equation as given below.

$$\frac{\mu}{\phi}\frac{d^2U}{dy^2} - \frac{\mu}{K}U + G = 0 \tag{2.2}$$

$G = -\frac{dp}{dx}$ is pressure gradient in *x*-direction. It is now simple to solve the ordinary differential equation (Eq. (2.2)), and the general solution is given by using the following equation:

$$U(y) = \frac{1}{\beta}\left[C_1 e^{\sqrt{\beta}y} + C_2 e^{-\sqrt{\beta}y} + \frac{G\phi}{\mu}\right] \tag{2.3}$$

Where, $\beta = \frac{\phi}{K}$, and C_1, C_2 are arbitrary integration constants. Now, we can impose the following boundary conditions to solve Eq. (2.3) as shown in Fig. 2.1:

no-slip condition at the bottom wall: $U(y)|_{y=0} = 0$ (2.4a)

and no stress jump at the upper part of porous strip (at $y = h$): $\mu \frac{dU}{dy}\Big|_{y=h^+} = \mu \frac{dU}{dy}\Big|_{y=h^-} \approx 0$

(2.4b)

Here, h is the thickness of the paper strip and is taken as 0.8 mm as shown in Fig. 2.1.

Hence, the one-dimensional velocity profile can be obtained as:

$$U(y) = \frac{G\phi}{\mu\beta}\left[A_1 e^{\sqrt{\beta}y} + A_2 e^{-\sqrt{\beta}y} - 1\right] \tag{2.5}$$

Where, $A_1 = \frac{e^{-\sqrt{\beta}h}}{e^{\sqrt{\beta}h}+e^{-\sqrt{\beta}h}}$, $A_2 = \frac{e^{\sqrt{\beta}h}}{e^{\sqrt{\beta}h}+e^{-\sqrt{\beta}h}}$ and h is the thickness of the porous strip.

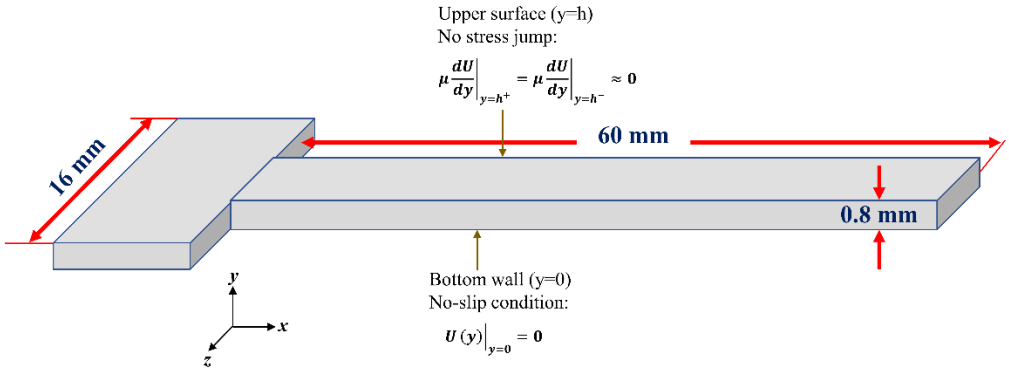

Figure 2.1. 3D schematic of the T-shaped paper channel (width = 0.8 mm) illustrating geometry and boundary conditions. No-slip is imposed at the bottom wall ($y = 0$), and a no stress jump condition is applied at the upper surface ($y = h$).

Accordingly, the average velocity of the liquid through the porous medium can be expressed as:

$$U_{avg} = \frac{\int_0^h U(y)dy}{\int_0^h dy} = \frac{G\phi}{\mu\beta}\left[\frac{-(\sqrt{\beta}h)^2}{1+\sqrt{\beta}h+(\sqrt{\beta}h)^2}\right] \quad (2.6)$$

Now, using $G = -\frac{dp}{dx}$, we can get:

$$U_{avg} = \left(-\frac{dp}{dx}\right)\frac{\phi}{\mu\beta}\left[\frac{(\sqrt{\beta}h)^2}{1+\sqrt{\beta}h+(\sqrt{\beta}h)^2}\right] \quad (2.7)$$

The pressure gradient, $-\frac{dp}{dx}$ can be expressed in finite representation as $\frac{\Delta p}{\Delta x}$. Here, Δp is the difference of pressure at the liquid-air interface (i.e., capillary pressure, p_c) and entry pressure; $p_c = \frac{2\sigma \cos\theta}{r_p}$; σ and θ are surface tension between liquid and water (=0.07206 N/m) and wetting angle is taken as 0^o; Δx is the difference of distance between interface and entry (Kumar *et al.* 2019). Considering origin at entry ($x_i = 0$), we have $\Delta x = x_f - x_i = x - 0 = x$. Also, the atmospheric pressure is same everywhere in the paper strip and one can write $\Delta p = p_f - p_i$; $p_f = p_c + p_{atm}$ and $p_i = p_{atm}$, hence, $\Delta p = p_c$. Therefore, from Eq. (2.7), we can write:

$$U_{avg} = \left(\frac{p_c}{x}\right)\frac{\phi}{\mu\beta}\left[\frac{(\sqrt{\beta}h)^2}{1+\sqrt{\beta}h+(\sqrt{\beta}h)^2}\right] = \frac{B}{x} \quad (2.8a)$$

Where, $B = \frac{p_c\phi}{\mu\beta}\left[\frac{(\sqrt{\beta}h)^2}{1+\sqrt{\beta}h+(\sqrt{\beta}h)^2}\right]$ (2.8b)

Hence, using $U_{avg} = \frac{dx}{dt}$, and integrating, we can get the temporal liquid interface imbibition length as:

$$x = (2Bt)^{\frac{1}{2}} \tag{2.9}$$

2.3. CALCULATION OF SATURATION DEPENDENT CAPILLARY PRESSURE

The sample of gel-blot paper can be rotated in the centrifuge machine at various angular velocities through putting it in a microcentrifuge tube with liquid of various food dye concentrations. Accordingly, the normalized liquid saturation can be defied as $\overline{S_e} = \frac{(w - w_{dry})}{(w_{at\ 100\%\ saturation} - w_{dry})}$. Where, w is the weight of the sample. Moreover, the capillary pressure (p_c) is estimated using the expression given below:(Rath *et al.* 2018b)

$$p_c = \frac{(r_2^2 - r_1^2)\Delta\rho\omega^2}{2} \tag{2.10}$$

The symbols ω and $\Delta\rho$, respectively, stand for the angular velocity and density difference between air and water. The microcentrifuge tube ends' distances from the axis of rotation are measured by r_1 and r_2, respectively.

2.4. NUMERICAL MODELLING

For the i[th] phase, the mass conservation equation in porous media is expressed as (H. and T. 1966):

$$\frac{\partial\left(\phi\rho_{s_{e_i}}\right)}{\partial t} + \nabla \cdot \left(\rho_{s_{e_i}}\boldsymbol{u}_i\right) = 0 \tag{2.11}$$

Where, one may write the volumetric flow per unit width as: $\boldsymbol{u}_i = -\frac{k_{rs_{e_i}}}{\mu_{s_{e_i}}} k_{eq} \nabla p_{s_{e_i}}$; moreover, the equivalent permeability of the porous medium, permeability ratio, dynamic viscosity and pressure field for saturation level, (s_{e_i}) are denoted by k_{eq}, $k_{rs_{e_i}}$, $\mu_{s_{e_i}}$ and p_{s_i}, respectively. The wetting phase and non-wetting phase permeability ratio with respect to 100% saturation case is expressed as $k_{rs_{e_w}} = \overline{S}_e^{\left(3+\frac{2}{\lambda_b}\right)}$ and $k_{rs_{e_n}} = (1 - \bar{S}_e)^2 \left(1 - \left(1 - \overline{S_e}\right)^{\left(1+\frac{2}{\lambda_b}\right)}\right)$, respectively. In addition, the relationship between normalised saturation and capillary pressure can be expressed as follows (Brentrup *et al.* 2008; Genuchten 1980): Using the Brooks and Corey correlation:

$$p_c\left(\overline{S_e}\right) = p_{en}\overline{S_e}^{-\frac{1}{\lambda_b}} \quad (2.12)$$

Where p_{en} and λ_b, respectively, stand in for the Brooks and Corey model parameters.

The following is how to write the continuity equation in its combined version with Darcy's law: (Brentrup *et al.* 2008; Genuchten 1980)

$$\frac{\partial(\phi\bar{\rho})}{\partial t} + \nabla \cdot (\bar{\rho}\bar{\boldsymbol{u}}) = 0 \quad (2.13)$$

Darcy's law gives us $\bar{\boldsymbol{u}} = \frac{k_{eq}}{\bar{\mu}}\nabla p$, averaged density is expressed as $\bar{\rho} = \sum_i s_{e_i}\rho_i$, and dynamic viscosity is written as $\bar{\mu} = \frac{\bar{\rho}}{\sum_i s_{e_i}\frac{\rho_i}{\mu_i}}$.

For a rectangular, two-dimensional paper-strip computational domain with length = 6 cm and width = 8 mm, we use the subsequent set of boundary conditions to numerically solve transport equations [Eqs. (2.11) and (2.13)] as follows: At the inlet: $\boldsymbol{n} \cdot \left(\rho_{s_{e_i}}\boldsymbol{u}_i\right) = 0,\ p_g = 0$; For the top and bottom ends: $\boldsymbol{n} \cdot \left(\rho_{s_{e_i}}\boldsymbol{u}_i\right) = 0$ and $\boldsymbol{n} \cdot (\bar{\rho}\bar{\boldsymbol{u}}) = 0$; where, $\boldsymbol{n}$ is the normal from the wall surface. At the outlet: For Darcy's equation, ensuring capillary pressure equal to zero corresponding to fully saturated paper, we impose $p = -p_c\prod(\overline{S_e})$; here, $\prod(\overline{S_e})$ is smoothed step function. This step function $\prod(\overline{S_e})$ is equal to 1 when $\overline{S_e}$ varies between 0 to 0.9, and smoothly (i.e., without losing differentiability) reaches $\prod(\overline{S_e})$ = 0 with change in $\overline{S_e}$ from 0.9 to 1. This approximation serves as a boundary condition for Eq. (2.13), it ought to be noted. Therefore, to determine the precise flux at that border, weak constraints are used. Also, the Lagrangian multiplayer (LM_p, unit: $\mathrm{kg/(m\text{-}s)}$) for the shape functions of pressure is used at the outlet to calculate the accurate mass flux ($\mathrm{kg/(m^2\text{-}s)}$) therein for Eq. (2.11). Hence, we have $-\boldsymbol{n} \cdot \left(\rho_{s_{e_i}}\boldsymbol{u}_i\right) = \frac{LM_p}{h}$, where, *h* is the thickness of the paper and taken as 0.8 mm. When weak constraints are used, it is observed that LM_p behaves as a new variable.

2.5. EXPERIMENTAL SETUP

2.5.1. Materials and experimental methods

2.5.1.1. Information of the paper strip

For the observation of capillary imbibition, Whatman gel blotting paper (grade GB003) of thickness 0.8 mm was procured. It has uniform wicking capability and capillary action which are important for obtaining good results. To minimize inertial effects, we have

opted for a uniform shape, a long paper strip with a sufficiently sized rectangular well, collectively forming a T-shape as illustrated in Fig. 2.2. This configuration allows for the permeation of a substantial volume of injected liquid inside the pores of the adequately large rectangular well, resulting in a plug-shaped interface during the initial stages of imbibition in the paper strip near the inlet. This plug or uniform interface shape confirms the minimal or insignificant influence of inertial effects. Building on the insights from Perez-Cruz *et al.* (2017b) regarding the imbibition phenomenon in different-sized paper strips, a uniform cross-section of the paper strip, compared to other shapes, leads to a higher imbibition length. This finding is further corroborated by experimental results from Jamshidi *et al.* (2022). Therefore, selecting a sufficiently sized rectangular well helps decrease inertial effects, while the uniform cross-section of the paper strip contributes to a higher imbibition length. Consequently, the T-shape of the paper strip with a suitably larger rectangular well and a uniform cross-section has been chosen due to these aforementioned advantages.

2.5.1.2. Food dye solution and equipment details

The analytical equation is derived by assuming Newtonian fluid. Hence, we have prepared 0.2, 0.5, 1 and 2 % (w/v) of food dye in deionized water. Beyond 2 % (w/v) concentration will lead to non-Newtonian behaviour of the liquid, as reported by Kim and Cho (2003). The viscosity of all the concentrations was measured in the Interfacial rheometer (Anton Paar, Model: MCR 301) and the value came out to be 0.0007 Pa-s. We repeated our experiment three times with each concentration and averaged out the readings. In our experiment, a high-resolution Nikon Z 50 camera, Canon EOS 5D Mark III camera and Schott LED light is used to capture the videos of the capillary-wicking dynamics of paper as shown in Fig. 2.3(a). A liquid dispenser (BRAUN Omnifix® -F) has been used to pour sample of the aqueous solution to the well as shown in the inset of the Fig. 2.3.

2.5.1.3. Software used for Image analysis

Further, the captured videos are transferred to the PC and are then processed in MATLAB R2022a to isolate the frames. The interface of wicking liquid is tracked through the frames corresponding to 1 second and the length of the wicking of the aqueous solution of food dye is measured using ImageJ software.

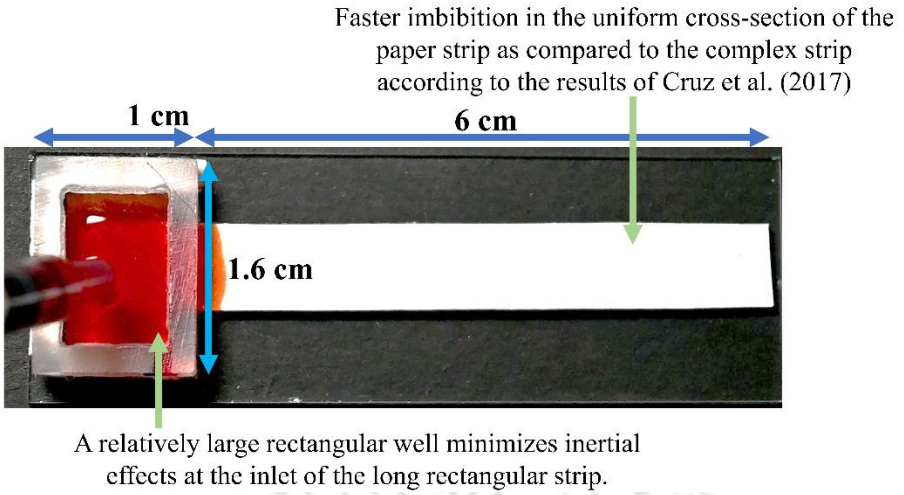

Figure 2.2. T- shape paper strip showing the rectangular well to minimize the inertial effect at the inlet of long rectangular paper strip in the right side. This rectangular shape of long paper strip allows faster imbibition dynamics as compared to the other complex paper strip shapes according to the result obtained by Perez-Cruz *et al.* (2017a).

2.5.1.4. Estimation of pore size

The pore size distribution of the gel blot paper is shown in Fig. 2.3b(i) and the corresponding pore size SEM of gel blot paper image as shown in Fig. 2.3b(ii). It is noted that the pore radius is calculated considering the pores as equivalent circular areas.

2.5.2. Modelling of the permeability of the porous substrate

In the literature, numerous frameworks have been developed for modelling the permeability of the intricate fibre structure using the simpler representative unit cell (Das *et al.* 2018; Maré and Woudberg 2023; Nabovati *et al.* 2009). It is worth adding here that transverse permeability appears to be an essential parameter in mimicking the flow dynamics within a paper strip utilised in microfluidic applications. Van der Westhuizen and Prieur Du Plessis (1996) established a mathematical model for transverse permeability in this regard using a simple rectangular unidirectional fibre cell and pure liquid (for example, water), which is represented as:

$$K_{water} = \frac{r_f^2 \pi \phi \left(1-\sqrt{1-\phi}\right)^2}{24(1-\phi)^{1.5}} \tag{2.14}$$

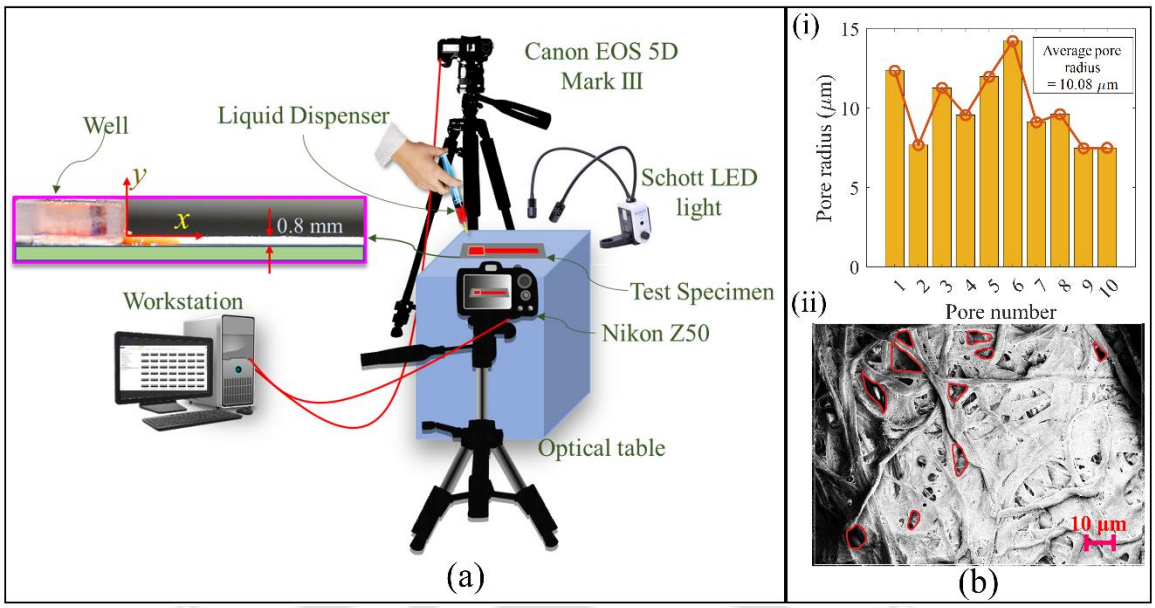

Figure 2.3. (a) The schematic of the experimental setup showing the porous strip as the test specimen on a table with liquid dispenser to insert the food dye solution inside the porous domain. The Scott LED light is used to illuminate the side view of the strip while Nikon Z50 and Canon EO5 5D Mark III camera are used to record the side view and top view of the test paper strip, respectively. The zoomed view of the specimen showing the side view is shown in the inset, (b) (i) The pore size distribution in terms of equivalent pore radius of circular areas of (ii) gel blot pores.

Deduced from the aforementioned equation, the expression of effective permeability for the liquid with species (e.g., aqueous solution of food dye) can be modelled as:

$$K = \frac{r_f^2 \pi \phi \left(1-\sqrt{1-\phi}\right)^2}{24(1-\phi)^{1.5}} F \qquad (2.15)$$

Here, F is a constant that can be calculated from experimental data to account for the influence of species in pure liquid (such as water) in the microfluidics study. In Eqs. (2.14) and (2.15), r_f is the average fibre radius which can be correlated to the pore radius as (Liu *et al.* 2015):

$$r_f = -r_p \, ln \, \phi \qquad (2.16)$$

The flow chart presented in Fig. 2.4 offers a brief overview of the previously discussed process for estimating saturation dependent permeability.

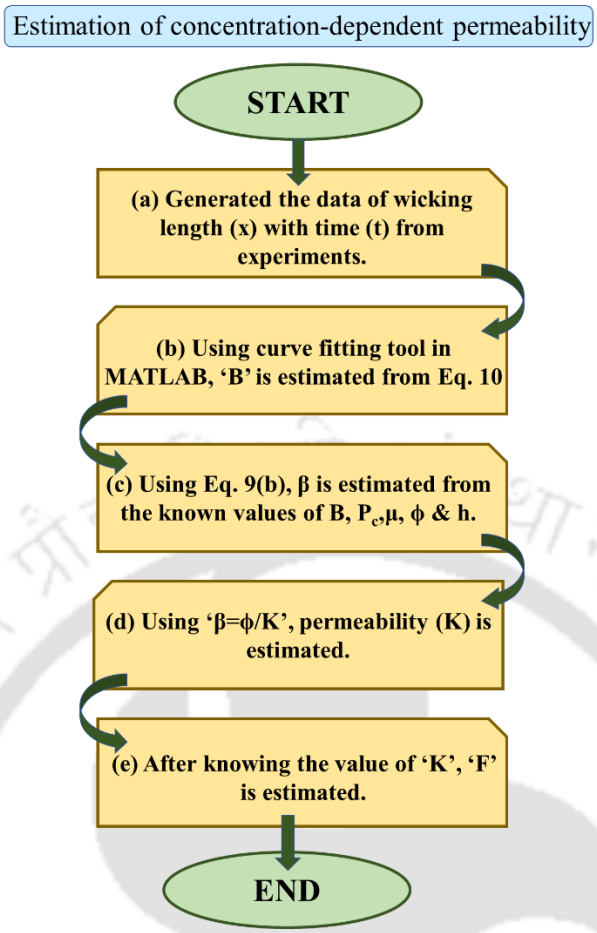

Figure 2.4. The flow chart representing the estimation of concentration-dependent permeability from the experimental data using the mathematical model.

2.5.3. Benchmarking of analytical solution with experiments in limiting case

In this section, we have made an effort to compare the experimental results of pure water (deionized water) being imbibed on a gel blot paper with the wicking length determined from the analytical solution. By changing the time instants, Fig. 2.5 illustrates the same comparison. It should be noted that the value of F has been taken as 1 for pure liquid in the Eq. (2.15). We find a fairly strong match between the experimental and the analytical findings. Hence, this evidence confirms that the existing analytical solution accurately reproduces the dynamics of imbibition within the gel blot paper strip. Additionally, we have made further attempts to determine the wicking length for various concentrations of food dye at different time intervals. Table 2.1, in both tabulated form and bar graphs, offers a comprehensive comparison of the mean wicking length at various time points for water and food dye solutions with varying concentrations. The examination involved three repeated tests for accuracy and consistency.

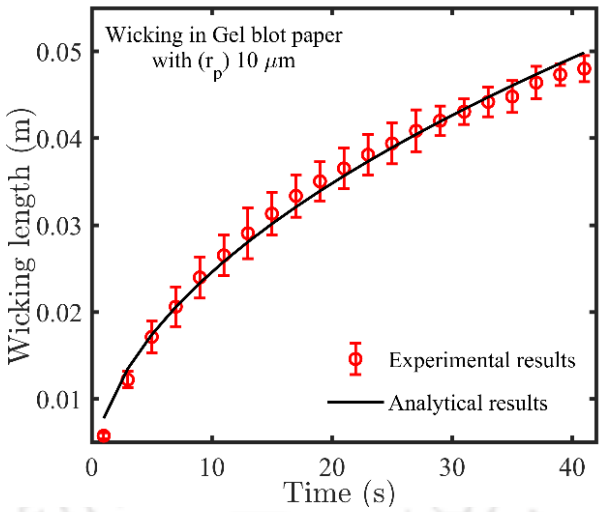

Figure 2.5. Plot showing the temporal variation of the length of the fluid filling column with Milli-Q water as the reference test fluid.

TABLE 2.1. Comparison of the mean wicking length according to the three repeated tests conducted at different times. (Below) The bar plot illustrates the wicking progress at three distinct time intervals (t = 5 s, 10 s, and 40 s), showcasing the effect of concentration on capillary transport over time.

	Wicking length (m)		
Concentration	t = 5 s	t = 10 s	t = 40 s
0.2 % (w/v)	0.016214	0.024492	0.045966
0.5 % (w/v)	0.012022	0.01808175	0.0369007
1 % (w/v)	0.016572	0.023210667	0.043019
2 % (w/v)	0.017589	0.026166	0.04699
0 % (w/v) (Water)	0.017153	0.025482	0.04773

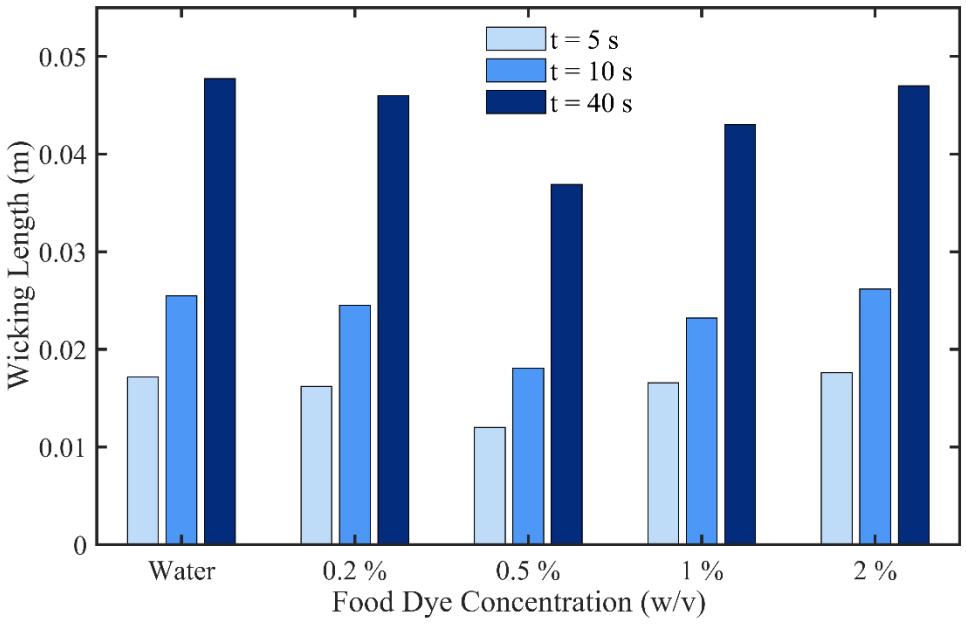

2.6. RESULTS AND DISCUSSION

We employed an aqueous food dye solution with a concentration range of 0 - 2 % (w/v) to examine the dynamics of imbibition within gel blot papers. The liquid column's interfacial dynamics for aqueous dye solutions have also been examined. Further, the concentration-dependent effective permeability is determined, and the value of F is predicted. Additionally, an estimation of the aqueous dye liquid saturation-dependent capillary pressure is conducted. In order to describe the saturation-dependent flow inside the porous strips utilised for numerical simulations, Brooks and Corey model parameters are determined.

2.6.1. Temporal variation of wicking length at different concentrations

At three different times, namely at t = 10 s, 20 s, and 30 s, Fig 2.6(d) shows the impact of dye concentration on the wicking length in the gel blot paper strip. As the concentration of the aqueous solution of food dye in Regime-I (refer to Fig 2.6(d)) increases from 0 to 0.5% (w/v) for all time instants, the plot demonstrates an abrupt decrease in wicking distance. This effect is related to an increase in flow resistance, mainly attributed to dye particle collisions in the microscopic fluid layer. Conversely, in Regime-II (refer to Fig 2.6(d)), the wicking length increases as the concentration increases from 0.5 to 2% (w/v). This could be explained by the pores getting obstructed as a result of the dye particles being entrapped. The capillary pressure increases as a result of this drop in effective pore radius because it is inversely proportional to the same. Additionally, the impact of concentration on capillary pressure is covered in the last sub-section. As a result, in Regime-II, an increase in wicking distance is witnessed at any time instant due to the rise in capillary pressure that occurs with an increase in dye concentration.

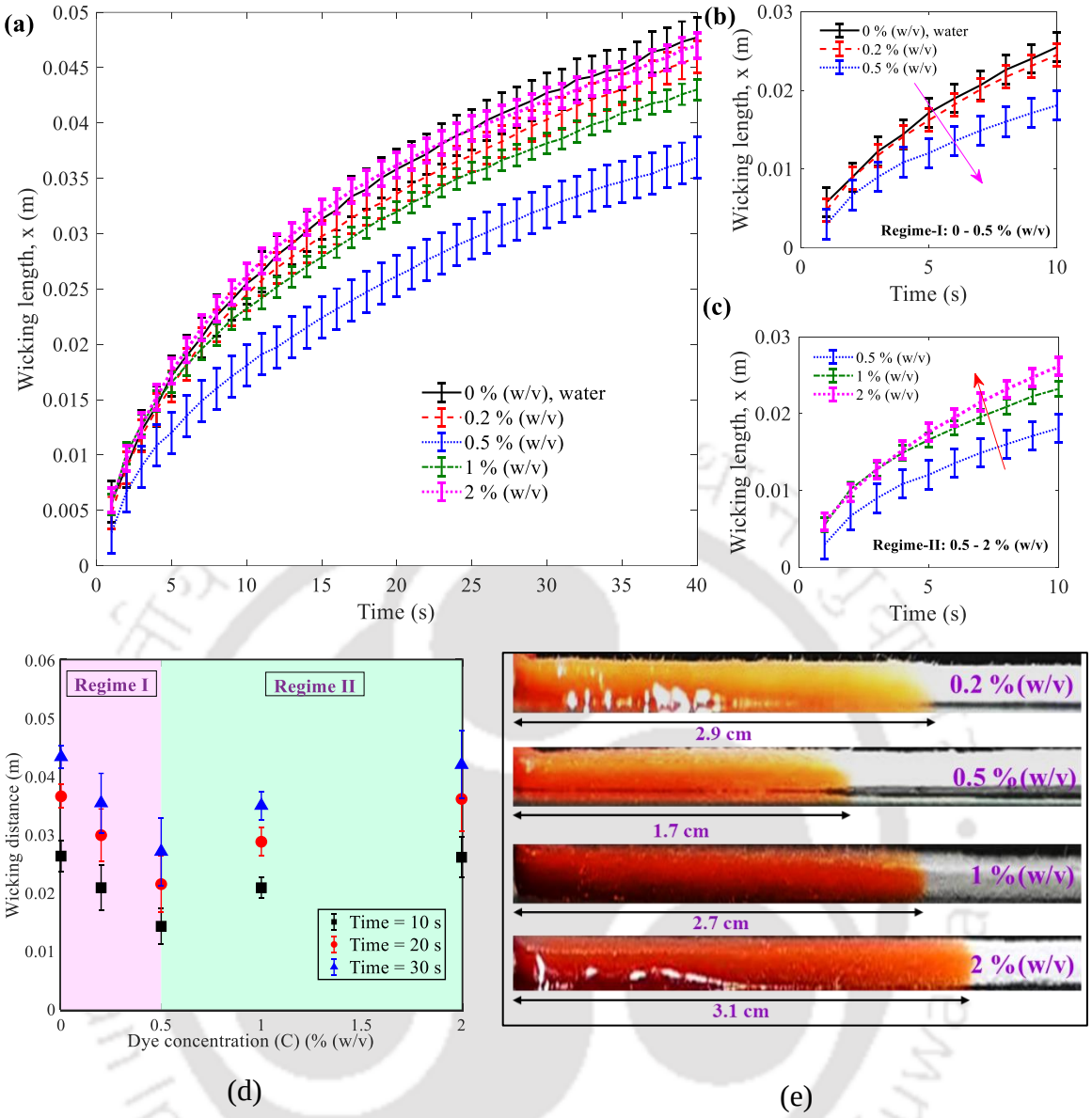

Figure 2.6. (a) Temporal variation of wicking length for different concentrations of food dye in deionized water, (b) the depiction of decrease in wicking length with concentration in Regime-I: 0 - 0.5 % (w/v), (c) the depiction of increase in wicking length with concentration in Regime-II: 0.5 - 2 % (w/v). (d) The variation of wicking length of the food dye solution at various concentrations of food dye in DI water for different time instants, (e) Experimental contours of side view of wicking developments at time = 10 s at various food dye concentrations.

For the solution with higher concentrations (2% w/v), we observe an interesting temporal interfacial phenomenon from the experimental observations. With lower dye concentrations, however, we do not see this phenomenon. We find that over a specified period of time, the side view of the air-liquid interface made an acute angle with the axial direction, as depicted in Fig. 2.7(a). The variation of interfacial angle of fluid front by varying time instants is presented in Fig. 2.7(b) when dye concentration is 2% (w/v).

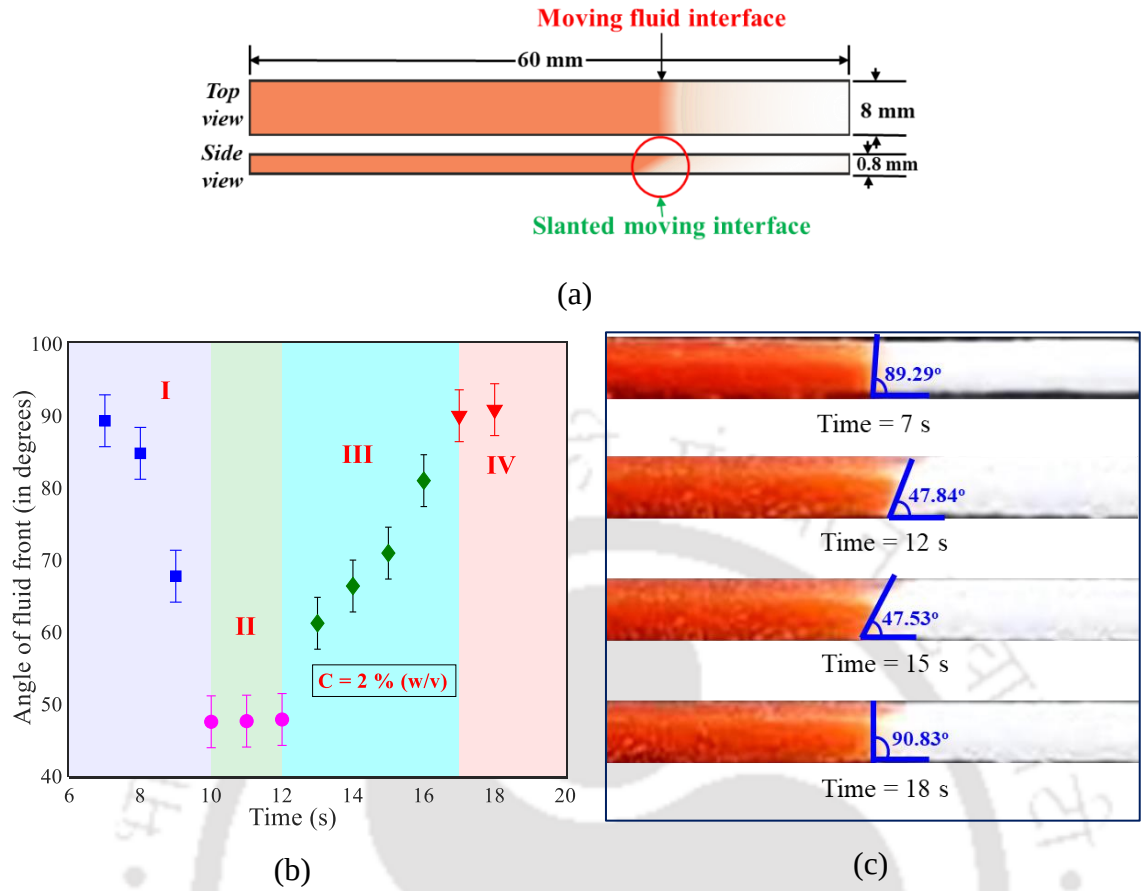

Figure 2.7. (a) Schematic representing the top and side view of liquid front, (b) the variation of angle of fluid front with respect to bottom wall at different wicking length (or time) when food dye concentration is 2 % (w/v), and (c) experimental contours of wicking developments at different wicking length (or time) when food dye concentration is 2 % (w/v).

-In Fig. 2.7(c), we depict the temporal contours of liquid front development. Also, the flow chart depicted in Fig. 2.8 visually represents the impending events associated with the lateral view of the fluid front within the porous strip. Near the entrance, it is observed that the front angle is almost ~90^{o} at initial time instants (refer to Fig. 2.7(c) for a clear view). This effect is attributed to the nearly uniform capillary pressure at initial time instants inside the pores when observed from the side view. On the contrary, we find a reduction in front angle (< 90^{o}) with further increase in time instants in Regime-I and nearly consistent variation in Regime-II. These observations can be explained by the following physical justifications. In Regime-I, the increased concentration leads to trapping of more dye particles in the upper section of the strip compared to the lower section when viewed from the side of paper strip (refer to Fig. 2.7(a)). Consequently, the smaller equivalent pore

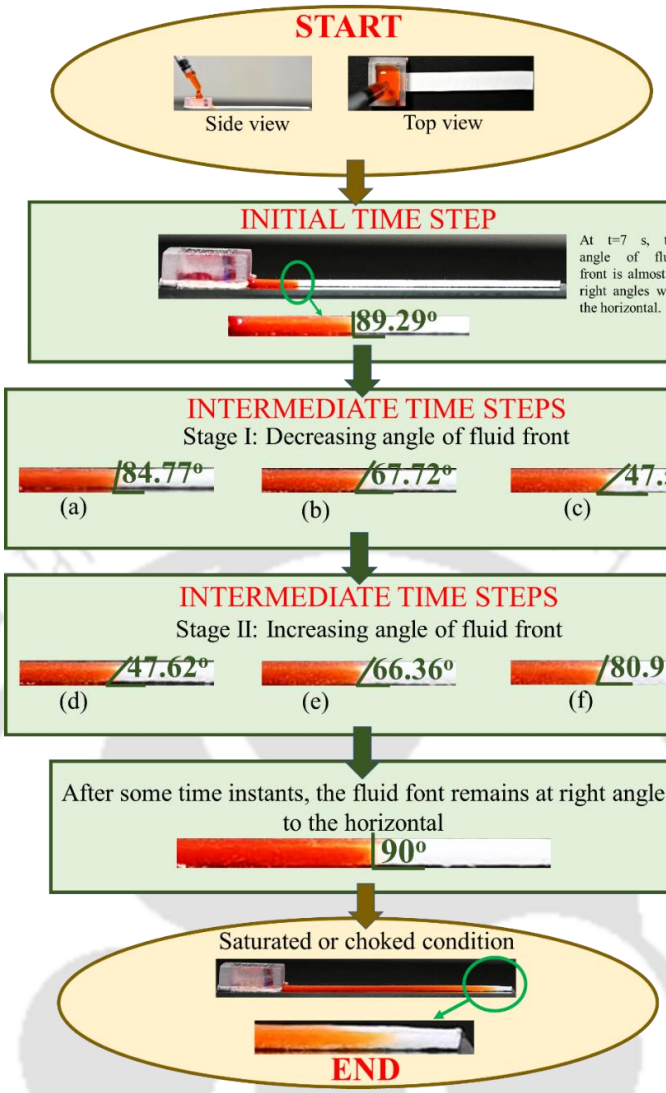

Figure 2.8. The representation of the change in angle of the moving fluid front in the paper strip

-radius at the upper section results in higher capillary pressure compared to the lower section. This discrepancy causes the liquid front to advance more rapidly in the upper section than in the lower section, ultimately resulting in an inclined frontal interface. Therefore, the increase in time in Regime-I leads to a reduction in the front angle. Furthermore, the minimal alteration in the difference of capillary pressure in upper and lower sections allows nearly constant frontal angle in Regime-II. Further increase in the time instants in Regime-III causes enhancement in front angle and eventually approaches ~90^{o} by the end of this regime. This occurs due to the improvement in the uniformity of particle trapping in upper and lower sections when viewed from the side, which in turn, reduces the difference of capillary pressure of the respective zones. Hence, the decrease in flow velocity difference at lower and upper section in Regime-III leads to an increase in

front angle and approaches ~90° towards the end of this regime. Finally, the effect of capillary pressure difference at the upper and lower sections becomes insignificant in Regime-IV. Subsequently, this causes nearly constant frontal angle (~90°) with increase in time instants.

2.6.2. Variation of permeability with different concentrations along the porous channel

The main objective of the present work is to estimate the concentration-dependent effective permeability (refer to Eq. (2.14)) to model the flow dynamics in the paper strip considering the effect of dye particle-pore interaction. Accordingly, an effort has been made to compute the same using Eqs. (2.8b) and (2.9). First, the value $(2B)^{0.5}$ is estimated by fitting the experimental data of the *x* versus *t* graph (refer to Fig 2.6(a)). After that, using values of B, p_c, h, ϕ and μ in Eq. (2.8b), we compute the value of $\beta\left(=\frac{\phi}{K}\right)$ as well as effective permeability, K. We depict the variation of effective permeability with a change in concentration in Fig. 2.8(a). Interestingly, there are two regimes of concentrations (Regime-I and II) are identified according to the variation of effective permeability. The value of K follows the decreasing trend with a change in concentration in Regime-I. It is attributed to the decrease in wicking length with concentration (refer to Fig 2.6(a-c)) because of the augmentation in flow resistance in the fluid layers by dye particle collision in the pores. The similar trend of decrement in permeability with particle concentration is predicted numerically by Feng *et al.* (2020). On the other hand, because of the increase in capillary pressure by a decrease in effective pore radius with concentration enhances the wicking length (refer to Fig 2.6(a-c)). As a result, the faster movement of the liquid front is predicted because of the increase in concentration of dye particles and enhances the effective permeability in Regime-II. As shown in Fig. 2.9(b) and (c), the mathematical correlations have been established for concentration-dependent permeability in both regimes using the second-order polynomial. We have obtained the accurately experimentally fitted expression of permeability in Regime-I and Regime-II as $K = pC^2 + qC + r$ and $K = sC^2 + tC + u$, respectively with $R^2 = 0.99$. The coefficients in these equations are as follows: $p = -2.21 \times 10^{-12}$, $q = -3.785 \times 10^{-13}$, $r = 1.689 \times 10^{-12}$, $s = -3.634 \times 10^{-13}$, $t = 1.398 \times 10^{-12}$ and $u = 3.386 \times 10^{-13}$.

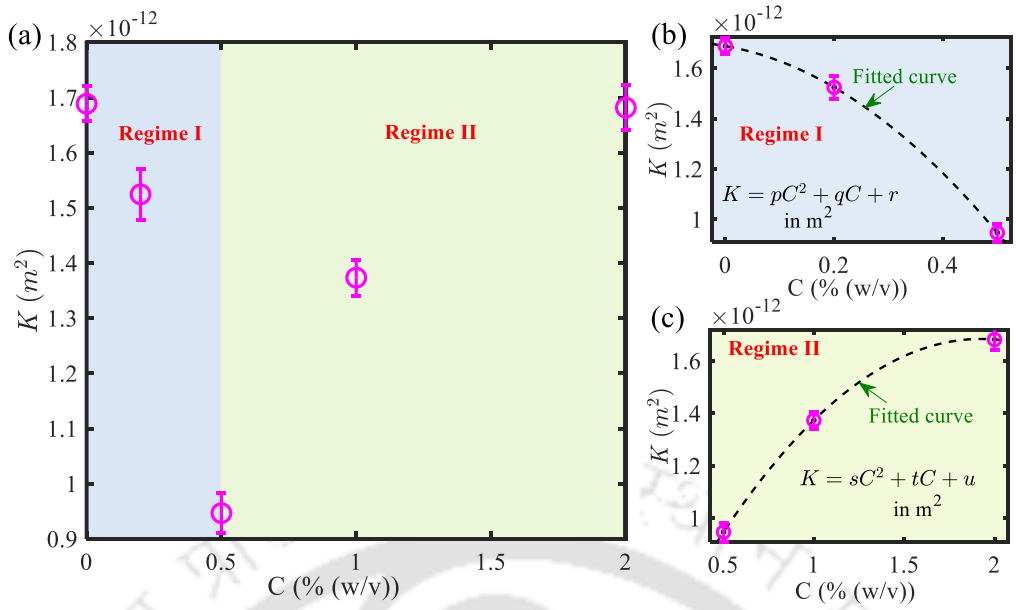

Figure 2.9. (a) The variation of effective permeability (K) of the porous strip with respect to various concentrations of food dye (C), the experimental fit of permeability in (b) in Regime-I and (c) Regime-II. The expression of permeability in Regime-I and Regime-II are obtained as $K = pC^2 + qC + r$ in m^2 and $K = sC^2 + tC + u$ in m^2, with $R^2 = 0.99$. Here, $p = -2.21 \times 10^{-12}$, $q = -3.785 \times 10^{-13}$, $r = 1.689 \times 10^{-12}$, $s = -3.634 \times 10^{-13}$, $t = 1.398 \times 10^{-12}$ and $u = 3.386 \times 10^{-13}$.

Table. 2.2. Estimation of concentration-dependent constant (F) of Eq. (2.15).

Concentration in % (w/v)	K for all concentrations (m^2)	F
0.2	1.52457×10^{-12}	0.903
0.5	9.4692×10^{-13}	0.5613
1	1.37355×10^{-12}	0.8142
2	1.68174×10^{-12}	0.9968

As discussed previously, the expression of permeability of representative elementary volume of porous media proposed by Van der Westhuizen and Prieur Du Plessis (1996) is valid for pure liquid in pores (refer to Eq. (2.14)). Using the same expression of permeability for the case of pure liquid, the expression of effective permeability when liquid having some species (e.g. food dye), is proposed in Eq. (2.15) by introducing a constant, F. The value of F, estimated for different food dye concentrations, is depicted in Table 2.2. This information may help to accurately predict the permeability of complex

paper-based porous media for the transport of analyte and biological species, mimicked by the flow of aqueous food dye particles in this study.

2.6.3. Saturation-dependent capillary pressure and numerical predictions

As we know that the analytical solutions for the wicking phenomenon are based on the Darcy's law and Lucas-Washburn equations, while the interface between liquid and air is assumed to be fully saturated or sharp. However, considering the realistic case for flow of aqueous solution in paper-based porous media, the interface is rather than partially saturated (Rath *et al.* 2018a). In this regard, the Richards equation can be considered to mimic the saturation-based flow modelling inside the paper-based porous media (Rath *et al.* 2018a). This mathematical framework needs model parameters to correlate the saturation dependent capillary pressure and permeability, which can be estimated from the experiments. Generally, the Brooks and Corey model is used to model the saturation-dependent capillary pressure and permeability for complex porous media. Therefore, the capillary pressure is experimentally measured using aqueous food dye solution and gel blot sample in Eppendorf tube by rotating it in the centrifuge at the rotational speed in the range of 100-13000 rpm. The capillary pressure is calculated using the formula: (Rath *et al.* 2018a)

$$p_c = \frac{\Delta\rho\omega^2(r_2^2 - r_1^2)}{2} \tag{2.17}$$

Here, $\Delta\rho$ is the density difference between the food dye solution and air; r_1 and r_2 are the radius of rotation of the sample in the Eppendorf tube close and far from the axis of rotation, respectively. The variation of capillary pressure with change in saturation $(\overline{Se})$ is depicted in Fig. 2.10(a) at different food dye concentrations. It is noted that saturation is defined as: $\overline{Se} = \frac{w - w_{dry}}{w_{sat} - w_{dry}}$. Here, w, w_{dry} and w_{sat} are weight of the sample when it is dry and when it is fully saturated, respectively. Observations indicate a sharp increase in capillary pressure when the value of $\overline{Se}$ decreases toward 0. This phenomenon is attributed to the rise in angular speed, resulting in a greater mass of liquid being drawn from the paper. This increase in angular speed significantly enhances capillary pressure since it is directly proportional to the square of the angular speed, as described in Eq. (2.17). Interestingly, it is observed that the effect of concentration on capillary pressure is significant for the smaller values of $\overline{Se}$. For a given value of smaller $\overline{Se}$, the value of capillary pressure decreases with increase in concentration from 0.2 -0.5 % (w/v). It is because of the increase in flow resistance by collision of dye particles, which is separately verified by the decrease

in wicking length with change in concentration 0.2 -0.5 % (w/v) as depicted in Fig. 2.6(d). On the other hand, an increased in capillary pressure is permitted by a concentration increase from 0.5 to 2% (w/v). This is explained by the particles being trapped, which reduces the effective pore radius and enhances capillary pressure.

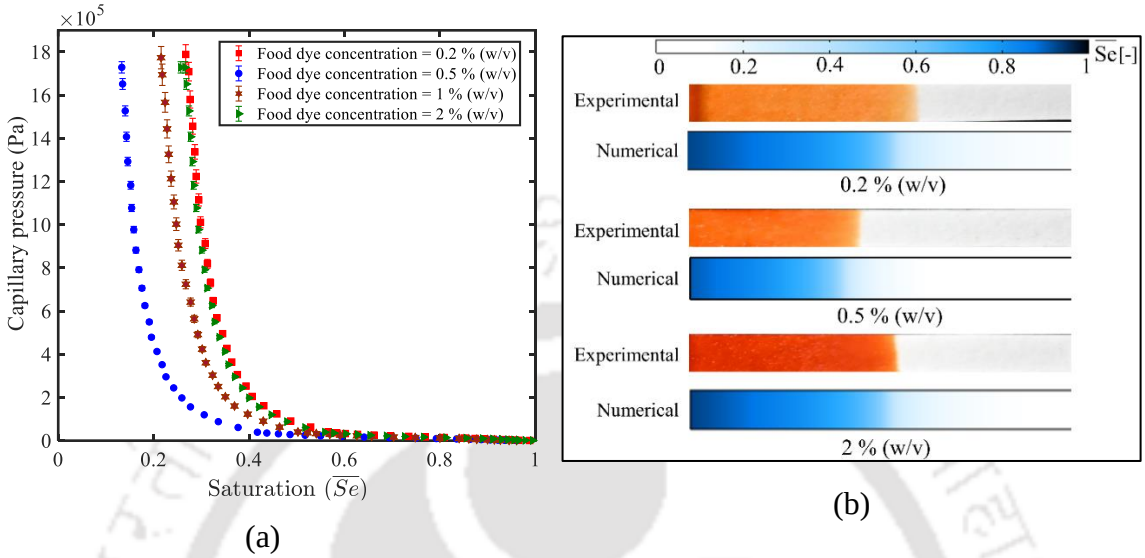

(a) (b)

Figure 2.10. (a) Variation of capillary pressure obtained from experiments by varying the normalized saturation of the liquid in the paper by varying the food dye concentration. (b) The comparison of contours of liquid saturation obtained by the experimental and numerical results when food dye concentrations are 0.2 % (w/v), 0.5 % (w/v) and 2 % (w/v).

After estimating the capillary pressure, the effort has been made to compute the Brooks and Corey model parameters p_{ec} and λ_p, which correlates the saturation and capillary pressure/permeability for Richards' equation. The details of Richards' equation and model parameters are presented in the Section 2.4. Further, the computational model is developed to mimic as well as to analyse the saturation dependent flow of food dye aqueous solution in gel blot paper using the COMSOL Multiphysics software (refer to Section 2.4 for more information about the governing equations and boundary conditions). For the numerical simulations, we use the Brooks and Corey model parameters as given in Table 2.3. From the simulated results, the saturation field is obtained and compared with the experimental results at different food dye concentrations in Fig. 2.10(b), obtained for the time instant, t=10 s. We find a closer match between the experimental and numerically predicted saturation fields in the considered range of food dye concentration. For more clear understanding of concentration dependent saturation, the variation of $\overline{Se}$ at t=10 s in axial direction of central region is depicted in Fig. 2.11. We observe that the capillary pressure decreases with an increase in concentration in the range of 0.2 – 0.5% (w/v) (refer to Fig.

2.10(a)). Conversely, an increase in concentration from 0.5 – 2% (w/v) results in an enhancement of capillary pressure at a given saturation level (refer to Fig. 2.10(a)). In summary, we can say that the predicted model parameters accurately able to predict the flow field in gel blot paper having specific species concentration in solution. This information leads to design of lateral flow assays which handles flow of solutions with analytes.

Table 2.3. Estimation of Brooks and Corey model parameters at different food dye concentration obtained from the capillary pressure versus saturation curve.

C in % (w/v)	p_{ec}	$1/\lambda_p$
0.2	8552	-4.45
0.5	4212	-3.5
1	5066	-3.8
2	7739	-4

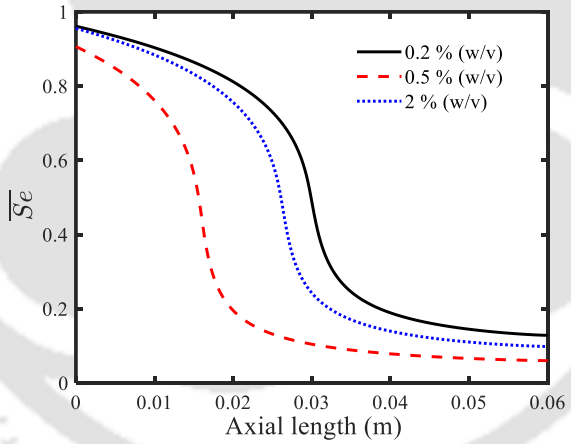

Figure 2.11. Variation of axial saturation level in paper strip by varying the food dye concentration for the time instant 10 s.

2.7. CONCLUSIONS

This investigation delves into the concentration-dependent capillary flow dynamics of aqueous dye solutions within the gel blot microfluidics paper. The gel blot paper chosen for the experiments proves to be an ideal material for studying species interaction due to its superior sample absorbency and volume per unit length compared to grade 1 and grade 4 papers. We have developed an analytical model to predict the capillary wicking process in gel blot paper strips, employing the Brinkman-extended Darcy equation. This analytical framework exhibits a good fit, as confirmed through verification with the case of deionized

water as the flowing liquid. Additionally, experiments involving four distinct aqueous solutions of food dye concentrations (0.2%, 0.5%, 1%, and 2% w/v) have revealed the concentration-dependent wicking phenomenon. The fitting parameters for wicking length versus time were obtained after estimating the time-dependent wicking length. Accordingly, by calculating the unknown constants, denoted as B and β (refer to Eqs. (2.8b) and (2.9)), the effective permeability $\left(K = \frac{\phi}{\beta}\right)$ was determined. Moreover, in the existing model with a simple rectangular unidirectional fibre cell and pure liquid, the expression of concentration-dependent effective permeability was established, introducing a constant, F (refer to Eq. 2.15). The findings reveal a significant influence of food dye concentration on wicking phenomena. In Regime I, an increase in food dye concentration led to a decreased wicking length, while the enhancement was observed in Regime II. Additionally, intriguing observations were made in side-view examinations, particularly with liquid of higher concentration (2% w/v). In this case, the fluid front angle was ~90° at lower and higher time intervals, with an acute fluid front angle at intermediate time intervals. Notably, the liquid front moved more quickly in the upper half than in the bottom half during intermediate time intervals. Subsequently, the effective permeability exhibited a trend of increasing at higher concentrations and decreasing at lower concentrations. Following the calculation of concentration-dependent permeability, we estimated the value of the constant, F (refer to Eq. 2.15). Furthermore, experimental estimations of saturation-dependent capillary pressure have been conducted. It was observed that capillary pressure increases with higher concentrations and follows a decreasing trend with lower concentrations. Estimating the Brooks and Corey model parameters allowed us to numerically model the saturation-dependent Richards' equation and, consequently, the related saturation-dependent flow field. This resulted in estimation of the saturation-dependent capillary pressure and permeability. By solving the mass conservation equation and combining Darcy's law, we conducted numerical simulations to obtain the saturation-dependent fluid flow in gel blot paper using COMSOL Multiphysics. The experimental and numerical results exhibited excellent agreement, suggesting the potential to develop paper-based microfluidics devices with species concentration-dependent flow with greater efficacy. In summary, the results of this study offer significant fresh insights into the concentration-dependent wicking phenomenon in thicker gel blot papers, which is crucial for developing low-cost testing devices for use in environmental and medical diagnostics.

CHAPTER 3

EXPERIMENTAL AND NUMERICAL INVESTIGATION OF CAPILLARY-DRIVEN LOW-COST DROPLET GENERATION IN Y-SHAPED PAPER-BASED POROUS MEDIA

This chapter analyzes pore-scale immiscible interfacial transport in paper-based porous media, focusing specifically on capillary-driven droplet generation. The study investigates the impacts of pore shape, paper grade, liquid saturation, and channel inclination on interfacial dynamics, capillary pressure, droplet formation, and transport mechanisms. We highlight how saturation-dependent capillary pressure and gravitational forces regulate droplet formation, merging, and size consistency within fibrous pore networks. Furthermore, the distinctive interaction between capillary and interfacial forces is demonstrated to govern droplet stability and transport performance. Finally, we demonstrate that micro-sized droplets appropriate for biochemical applications can be passively generated at low-cost through controlled pore-scale forces.

3.1. OBJECTIVE

The increasing demand for accurately sized micro- and nanoscale droplets has generated considerable interest in droplet control within microfluidic systems, owing to their extensive applications in compound synthesis, chemical engineering, medical diagnostics, cellular research, food sector, and the pharmaceuticals industry (Cai *et al.* 2025; Chowdhury *et al.* 2021; Lathia *et al.* 2023). Due to their increased surface-to-volume ratio, droplets expedite reaction rates, promote heat transfer efficiency, facilitate high-throughput experiments, and minimize reagent use. In lab-on-a-chip systems, droplets serve as discrete reaction chambers, allowing for meticulous regulation of minimal volumes and ensuring consistent testing under regulated circumstances.[2]

Recent research has concentrated on the generation of droplets employing microchannels and micro-capillaries, wherein droplet disintegration adheres to energy balance principles, including the Roof snap-off principle, and is influenced by capillary and shear pressures. Diverse geometries, such as T-junctions, diverging channels, and multi-

[2] Contents of this chapter is published in the journal of **Soft Matter, Volume 21, Pages 6891-6909, 2025,** DOI: 10.1039/D5SM00498E

inlet microfluidic devices, have been utilized to produce droplets of precise dimensions. Conventional microfluidic platforms are frequently costly, labour-intensive, and dependent on external pumping systems, which restricts their accessibility and scalability.

Paper-based microfluidic strips provide an inexpensive substitute for droplet generation driven solely by capillary wicking in order to overcome these drawbacks. The intricate microscale pore structure inherent to paper enables dispersed-phase breakdown and droplet transport without the need for external actuation. Prior research demonstrates that pore geometry, saturation, and pore obstruction affect droplet formation and retention in porous media (Azizov *et al.* 2022). Furthermore, the inclusion of cellulose fibers adds complexity to the behavior of two-phase flow. This work aims to examine the essential mechanisms that regulate the generation of microsized droplets in paper-based porous surfaces.

3.2. MATERIALS AND METHODS

3.2.1. Materials

We have fabricated Y shaped (as shown in Fig. 3.1) paper strip using Whatman™ Grade 1 (CAT No. 1001-125; Lot No. 17723247).and Grade 4 filter paper (CAT No. 1004-125; Lot No. 18055904). We fabricated paper strip with desired dimension using a CO_2 laser cutting system (Fusion Edge Laser Series, Epilog Laser) at 3W. The dimensions of the channel are shown the Fig. 3.1. The paper strip was kept on a stack of glass slides as a base to adjust the height of the channel inlets and outlet according to the height of the petri dish. Acrylic cubes were machined in the workshop and were used to produce an inclination angle to the fluidic pathway kept on a glass slide (cf. Fig. 3.1). The cubes were rubbed on sandpaper to even out the rough edges. Mineral oil was procured from Himedia and used as the dispersed phase liquid. We used Milli Q water as the continuous phase liquid. Disposable petri dishes (35 mm dia) were purchased from Tarsons. Images and videos were captured with a high-resolution Nikon mirrorless camera (Nikon Z 50). The oil droplet movement inside the pore structure of the paper-based microchannel was observed and captured using 10x magnification objective lens of upright microscope (make: Nikon, model: ECLIPSE C*i*). We calculated the diameter of the generated droplets from the captured videos by using MATLAB and ImageJ® software (Schneider *et al.* 2012).

3.2.2. Methods

3.2.2.1. Experimental procedure for droplet generation

Figure 3.1 shows the arrangement where the Y-shaped paper-based fluidic pathway is placed on a glass substrate. The height of the paper strip is adjusted such that the petri dishes and the fluidic pathway lie on the same plane. The width of the channel, considered to be 3 mm in this analysis, was maintained throughout the channel. We considered the length of the larger part (3 cm) of the Y-shaped fluidic strip for all experiments conducted in this endeavour. The paper-based strips are first kept in warm DI water to remove impurities, if present any, from therein. Afterward, they are oven dried at 27^{o}C for 20 mins. The tip of the end of the strip is dipped inside the Milli Q water for the collection of generated droplets in the petri dish. During the experimentations, mineral oil was supplied to the right arm of the Y-shaped paper strip, and Milli Q water is supplied to the left arm of the same. Following the capillary imbibition, the water and oil are wicked through the paper-based fluidic pathway. At the Y-junction of the paper strip, the oil coming from the right arm of the Y-shaped paper strip gets sheared-off to form droplets because of the fiber structure of the paper. The water flowing from the left arm takes the oil droplets being generated with it to the end of the Y-shaped paper strip and then to the petri dish containing Milli Q water. Note that, for a given strength of capillarity, the Milli Q water coming from the left arm acquires increased velocity as compared to the imbibition of oil, attributed primarily to a relatively lesser viscosity of Milli Q water. So, the right arm is placed first in the petri dish containing mineral oil and after the oil has reached the bifurcation junction of the channel, water is let through the right arm of the fluidic pathway. After the Y-shaped paper strip is fully saturated, 5mm of the length is then dipped in the petri dish containing Milli Q water as shown in Fig. 3.1. The droplets can be seen coming out of the fluidic pathway. A digital camera, as mentioned before, is used to record videos of the process of droplet generation from the microporous structures of the paper-based fluidic pathway. The videos were converted into images using MATLAB code. The number of droplets are counted and ImageJ®(Schneider *et al.* 2012) software is used to measure the diameter of droplets. A detailed analysis is made to figure out the droplet generation rate.

The experiments are repeated five times to establish the proof-of-concept as well as to ascertain the repeatability of the underlying droplet generation phenomena. Every time the glass slides are cleaned properly with the chloroform and a new Grade 1 paper-based fluidic pathway is used before running an experiment. It is worth mentioning here that we conducted experiments by considering the inclination angle of 0^{o} and 10^{o}.

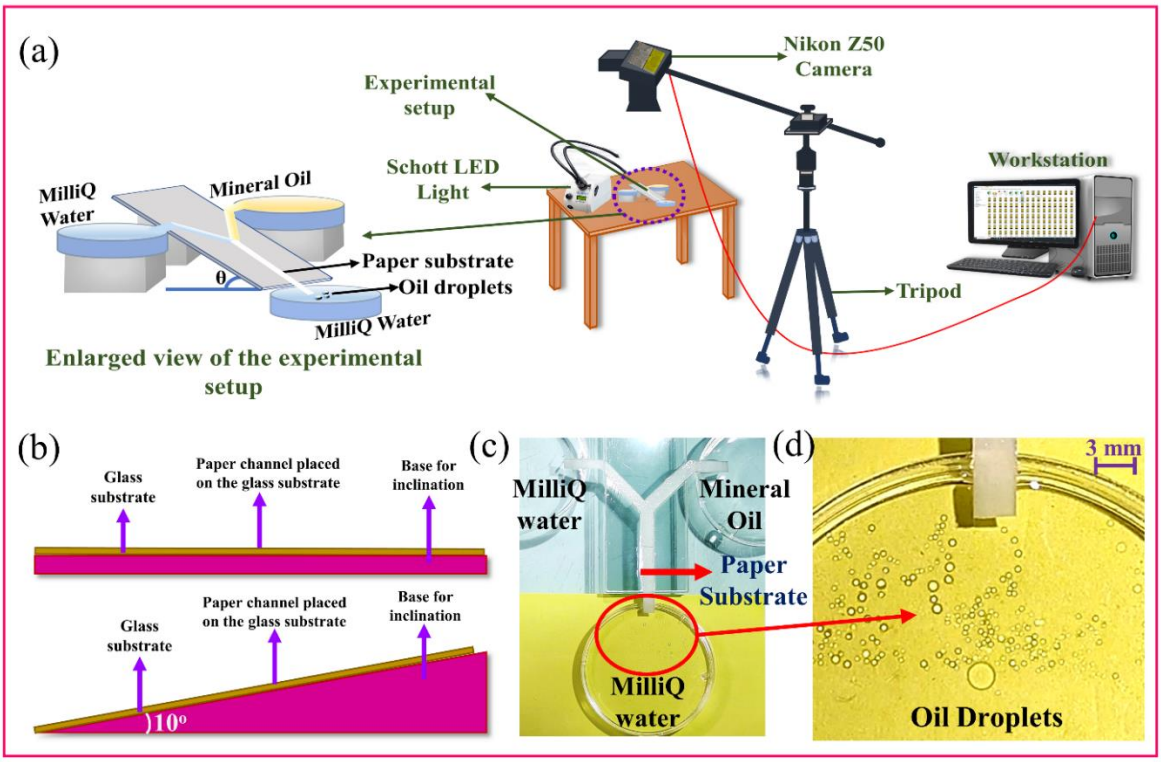

Figure 3.1. (a) Illustration depicts the experimental setup and data analysis for droplet generation using a paper substrate, (b) the glass substrates are angled using acrylic base for studying effect of different paper substrate positions on droplet generation, (c) Top view of experimental arrangement with ongoing droplet generation, (d) zoomed view of the generated droplets in the petri plate.

3.2.2.2. Experimental procedure for measuring the capillary pressure as a function of saturation

In order to determine capillary pressure as a function of liquid saturation, we have cut Whatman Grade 1 and Grade 4 papers into rectangular strips (2.3 cm × 0.5 cm). The fabricated paper strips were then saturated initially with Milli Q water. Subsequently, these strips were saturated with a mixture of mineral oil and Milli Q water. Colloidal form of mineral oil and water was prepared taking 50 % of each by volume and then vortexed (Spinix- Vortex shaker, Tarsons). The saturated rectangular strips were subsequently positioned in a 600 µL Eppendorf tube with a slot at the base. Prior to inserting the tubes into the centrifuge, the 600 µL tube was positioned within a 1.5 mL Eppendorf tube and subjected to centrifugation, starting at 300 rpm and increasing to a maximum of 13,300 rpm with incremental adjustments in speed. After the spin at each speed, the paper strips were removed from the tube and weighed in. These weights were further used to calculate saturation $(\overline{Se})$ of liquid, which is defined as the fraction of the pore volume filled with

liquid. The saturation value was calculated as: $\overline{Se} = \frac{(w-w_{dry})}{(w_{sat}-w_{dry})}$, where w is the weight of the paper strip after each spin, w_{dry} is the dry weight and w_{sat} is the weight at full saturation. The Hassler-Brunner model (Xu *et al.* 2022) seems to be limited in its accuracy in estimating the capillary pressure in the centrifuge method, according to research by Xu *et al.* (2022). Instead, they proposed a more precise method for estimating saturation-based capillary pressure in centrifuges, known as the double integral method. According to the double integral approach, the saturation dependent capillary pressure can be represented as:(Xu *et al.* 2022)

$$p_c = \Delta\rho\omega^2\left(\frac{RL}{4} + \frac{5L^2}{72}\right) \quad (3.1)$$

Where, $\Delta\rho$ is the difference in the densities of wetting and non-wetting fluids. In the present study, $\Delta\rho = 998.79$ kg/m^3 was taken when only Milli Q water is wicked through the paper strips and $\Delta\rho = 933.8$ kg/m^3 was used when the mixture of 50-50 % mineral oil and Milli Q water. Also, R and L denote the distance from the axis of centrifuge rotor to the centre of the core and the length of the core, respectively.

3.2.3. SEM imaging and contact angle measurement

Whatman™ Grade 1 and Grade 4 filter papers were cut into 1 cm ×1 cm square strips. Glass slides were cut into 1 cm × 1 cm square shapes using a glass cutter and the paper strips were pasted on them using carbon tapes. Before being loaded into the instrument for topographical imaging the paper specimens were gold coated. Then the Field Emission Scanning Electron Microscope (FESEM, make: Zeiss, model: Sigma) has been used for the visualization of the pore structure inside the Grade 1 paper and Grade 4 paper at 141x magnification.

For the measurement of contact angle, we have used Grade 4 paper as the base substrate and carefully placed on a glass slide for support. The base was then placed on the stage of Goniometer (make: Apex Instruments) and with the use of a microliter glass syringe (make: Hamilton Co.) and droplet dispensing module (Acam-NSC) 5 µl droplets (oil and water) were put on the grade 4 paper. The image was captured using a CMOS camera (Nikon, D5200) after 80 ms of the droplet contact with the paper and a white light source along with a diffuser was used to illuminate the droplet. The contact angle was then calculated from the captured images using the ImageJ® (Schneider *et al.* 2012) software.

3.2.4. Foundations of droplet generation in porous system

As depicted in Fig. 3.2, which demonstrates two relevant forcing exerted on a droplet at the membrane pore. One being the detaching forces (F_D), which push the droplets away from the pore, and the other is the retaining forces (F_R), which keeps the droplets attached to the pore (Piacentini *et al.* 2014). The detaching force includes capillary force, static pressure force and gravitational force. On the other hand, the retaining force includes to interfacial forces which is able to attract liquid molecule towards the pore surface (Amiri Roodan *et al.* 2020; Norouzi Darabad *et al.* 2024; Sharratt *et al.* 2018; Shenoy *et al.* 2025).

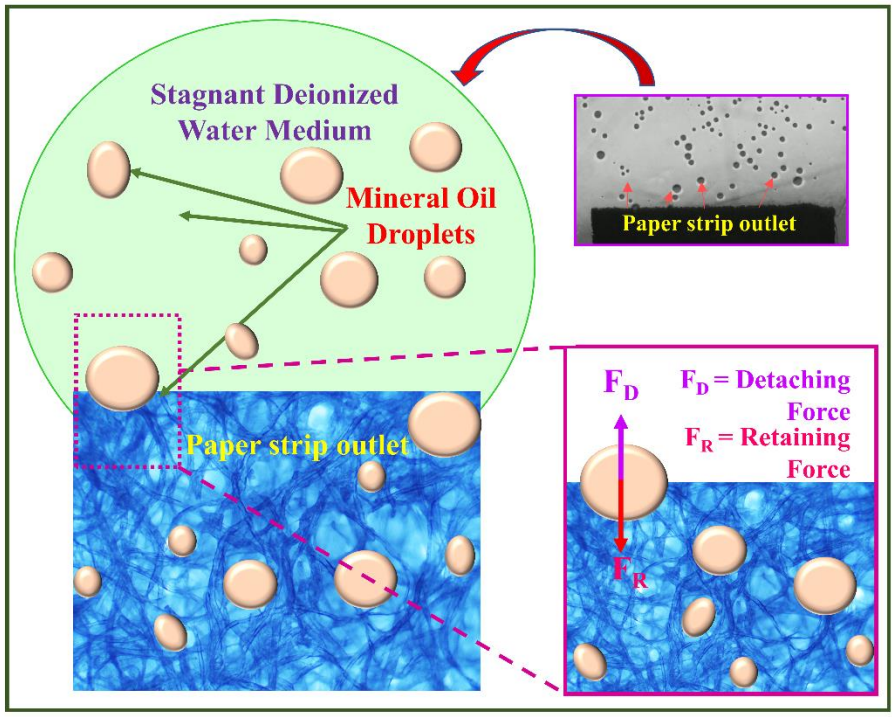

Figure 3.2. The mechanism showing the oil droplet generation under the interaction of detaching and retaining forces.

3.2.5. Dimensionless number analysis associated with droplet generation

For the associated droplet generation, oil and water transported mainly via driving capillary force. During the mixing of water and oil stream after the junction, the order of mean velocity (u_{ref}) for Grade 4 paper strip is obtained as ~10^{-4} m/s using the image analysis of the temporal interface. For mean density (ρ_{mean}) as 935 kg/m^3 and viscosity of oil (μ_B) as 0.0306 Pa-s, the order of Reynold number $\left(Re = \frac{\rho_{mean} u_{ref} r_p}{\mu_B}\right)$ is obtained as ~10^{-5} considering the characteristic length scale as pore size for both Grade 1 and Grade 4 paper. Hence, we can safely say that the underlying flow inside the paper strip is highly viscous force dominated as compared to the inertial counterpart. Moreover, the ratio of

viscous to surface tension force is represented by the capillary number $\left(Ca = \frac{\mu_B u_{ref}}{\sigma}\right)$, where σ (= 0.0583 N/m) is interfacial surface tension coefficient. Hence, the order of Ca is obtained as ~10^{-4}. Hence, the flow is capillary dominated as compared to the viscous counterpart. Furthermore, the influence of gravity on droplet generation can be quantified in terms of the dimensionless Bond number $\left(Bo_\theta = \frac{g \sin\theta(\rho_w - \rho_o)d_p^2}{\sigma}\right)$, which is defined as ratio of relative magnitude of gravitational force acting on wetting phase liquid (compared to non-wetting phase liquid) to the surface tension force (Li *et al.* 2018; Ray *et al.* 2010). For paper strip with inclination angle θ = 0°, 5°, 10° and 20°, the value of Bo_θ is obtained as 0, 2.9×10^{-7}, 5.9×10^{-7} and 1.16×10^{-6}, respectively. Additionally, the Darcy number (Da), which represents the dimensionless form of permeability, is expressed as $Da = \frac{k}{d_p^2}$. Here, permeability of complex pore structure of paper strip is expressed as $k = \frac{r_p^2 \pi\phi\left(1-\sqrt{1-\phi}\right)^2}{24(1-\phi)^{1.5}}$; where r_p and ϕ are pore radius and porosity, respectively. The permeability of Grade 1 ($r_p = 5.66\mu$m, $\phi = 0.68$) and Grade 4 ($r_p = 11.7\mu m$, $\phi = 0.77$) are obtained as 2.8×10^{-12} m^2 and 2.99×10^{-11} m^2, respectively. Hence, the value of *Da* is obtained as $2.1 \times 10^{-2}$and 6.1×10^{-2}, respectively, for Grade 1 and Grade 4 paper.

3.3. MATHEMATICAL MODELLING FOR TWO-PHASE FLOW

The mathematical modelling framework consistent with the phase-field method, as developed in this endeavour to investigate oil droplet formation pertaining to oil-water transport through paper-based fluidic pathway, is described below.

Phase-field method

In the phase-field method, interface separating immiscible liquids is typically considered as diffuse thin layer in which the fluid properties such as viscosity and density vary steeply but continuously. The phase-field method has thermodynamic basis and originated from free energy theory (Liu *et al.* 2013; Moelans *et al.* 2008; Mondal *et al.* 2015a; Yang *et al.* 2021). This method has an inherent feature of alleviating the stress singularity at moving contact line. In the present study, we consider incompressible immiscible transport of binary system, constituted by two Newtonian liquids. The physical domain considered for numerical simulations of a single pore structure is taken as a converging- diverging shape (c.f. Fig. 3.3 (a)) which is in accordance with the pore structure observed through SEM

imaging (c.f. Fig. 3.3 (b)). According to phase-field model, the free energy for system can be written as follows (Liu *et al.* 2013; Mondal *et al.* 2015a; Pismen and Pomeau 2000):

$$F_{fe}(\varphi) = \int_{\Omega}[0.5\Psi(\nabla^2\varphi) + f(\varphi)]\partial\Omega \quad (3.2)$$

In Eq. (3.2), the bulk free energy can be expressed in double-well function as $f(\varphi) = a(\varphi^2 - 1)^2$ with arbitrary constant, a. Now, $f'(\varphi) = b\varphi^3 - c\varphi$; where b and c can be measured by the molecular dynamic simulation as $b = c = \frac{\Psi}{\varepsilon^2}$ with interface thickness, ε and mixing energy density Ψ (Bai *et al.* 2017). The interfacial surface tension is expressed as $\sigma = \left(\frac{2\sqrt{2}}{3}\right)\frac{\Psi}{\varepsilon}$. Accordingly, the chemical potential can be written as $G = \frac{\delta F_{fe}}{\delta\varphi = \frac{3\sigma\varepsilon}{2\sqrt{2}}}\left[-\nabla^2\varphi + \left[\left(\frac{\varphi}{\varepsilon^2}\right)(\varphi^2 - 1)\right]\right]$. Hence, the surface tension force can be expressed as:

$$F_s = G\nabla\varphi = \left[\frac{3\sigma}{(2\sqrt{2}\varepsilon)}\right]\left[-\varepsilon^2\nabla^2\varphi + [(\varphi)(\varphi^2 - 1)]\right]\nabla\varphi \quad (3.3)$$

Now, the much celebrated Cahn-Hilliard equation, also known as the phase-field equation, can be written (Cahn and Hilliard 1958, 1959):

$$\frac{\partial\varphi}{\partial\tilde{t}} + \boldsymbol{u}\cdot\nabla\varphi = \nabla\cdot(M\nabla G) \quad (3.4)$$

Here, $M = \chi\varepsilon^2$ is the mobility parameter that controls the interface thickness. Note that χ plays a role as mobility tuning parameter (Bai *et al.* 2017).

The transport equations governing the flow dynamics through the paper-based fluidic pathway are written below (Liu *et al.* 2013; Mondal *et al.* 2015b):

$$\nabla\cdot\boldsymbol{u} = 0 \quad (3.5)$$

$$\rho\left(\frac{\partial\boldsymbol{u}}{\partial t} + \boldsymbol{u}\cdot\nabla\boldsymbol{u}\right) = -\nabla p + \nabla\cdot\mu(\nabla\boldsymbol{u} + (\nabla\boldsymbol{u})^T) + G\nabla\varphi \quad (3.6)$$

Here, the equivalent density: $\rho = \rho_A\left(\frac{(1-\varphi)}{2}\right) + \rho_B\left(\frac{(1+\varphi)}{2}\right)$, and viscosity:$\mu = \mu_A\left(\frac{(1-\varphi)}{2}\right) + \mu_B\left(\frac{(1+\varphi)}{2}\right)$, p is the pressure field; and A and B corresponds to water and oil, respectively. Note that Eq. (3.4) takes care of the dynamical evolution of the interface in tune with the flow velocity. The last term of Eq. (3.6) accounts for the forcing term that stems from the presence of the interface, dynamically evolves with the flow velocity, in the flow field.

Non-dimensional form of governing equation

The governing equations mentioned above have been normalized using the following scales: $\overline{\nabla} \equiv \left(\frac{1}{r_p}\right)\left(\frac{\partial}{\partial x, \frac{\partial}{\partial y}}\right)$, $\bar{u} = (\bar{u}\hat{\imath} + \bar{v}\hat{\jmath}) = \frac{\boldsymbol{u}}{u_{ref}}$, $\bar{t} = \frac{\boldsymbol{r_p}}{u_{ref}}$, $\bar{p} = \frac{p}{\left(\frac{\mu_B u_{ref}}{r_p}\right)}$, $\bar{\mu} = \frac{\mu_A}{\mu_B}$, $\bar{\rho} = \frac{\rho_A}{\rho_B}$,

$Re = \frac{\rho_B u_{ref} r_p}{\mu_B}$, $Pe = \frac{u_{ref} r_p^2}{\sigma M}$, $Cn = \frac{\varepsilon}{r_p}$, $Ca = \frac{\mu_B u_{ref}}{\sigma}$.

Dimensionless Cahn-Hilliard equation

$$\frac{\partial \phi}{\partial \bar{t}} + (\bar{u} \cdot \overline{\nabla}\varphi) = \frac{3}{2\sqrt{2}} \frac{1}{Pe} \overline{\nabla} \cdot \left[\overline{\nabla}\left(-Cn^2 \overline{\nabla^2}\varphi + [\varphi(\varphi^2 - 1)]\right)\right] \tag{3.7}$$

Dimensionless continuity and momentum equation:

$$\overline{\nabla} \cdot \bar{u} = 0 \tag{3.8}$$

$$Re\bar{\rho}\left(\frac{\partial \bar{u}}{\partial \bar{t}} + \bar{u} \cdot \overline{\nabla u}\right) = -\overline{\nabla p} + \overline{\nabla} \cdot \bar{\mu}(\overline{\nabla u} + (\overline{\nabla u})^T) + \frac{1}{CaCn}\left(-Cn^2 \overline{\nabla^2}\varphi + \varphi(\varphi^2 - 1)\right)\overline{\nabla^2}\varphi \tag{3.9}$$

Here, $\bar{\rho} = \left(\frac{(1-\varphi)}{2}\right) + \left(\frac{(1+\varphi)}{2}\right)\rho_r$, $\bar{\mu} = \left(\frac{(1-\varphi)}{2}\right) + \left(\frac{(1+\varphi)}{2}\right)\mu_r$.

For the numerical simulations, we have imposed $\bar{u}_{inlet} = 1$, $\bar{p}_{outlet} = 0$ and symmetry at the centreline, i.e., the transport variable gradient at the centreline equal to zero. Further, we have also implemented, $Pe = 0.2$ (YUE *et al.* 2010), $Re = 0.0001$, $Cn = 0.01$ (YUE *et al.* 2010), $\frac{\rho_A}{\rho_B} = 1.14$, $\frac{\mu_A}{\mu_B} = 0.033$ for oil-water combination. The capillary number for Grade 4 paper is taken as $Ca = 10^{-4}$ for numerical simulations as discussed in sub-section 3.2.5. Now, using the Hagen–Poiseuille equation, the velocity profile is written as $u = \frac{\Delta p_c (r_p^2 - r^2)}{4\mu_B L}$, with $\Delta p_c = \frac{2\sigma \cos\theta}{r}$. Hence, the reference velocity scale $\left(u_{ref}\right)$ can be written as $u_{ref} = \frac{\Delta p_c (r_p^2)}{4\mu_B L}$. Therefore, the value of u_{ref} for Grade 1 paper will be two times higher than that of Grade 4 paper because r_p of Grade 1 is half of Grade 4 paper. As a result, the Ca for Grade 1 paper is taken as 2×10^{-4} for numerical simulations.

We have used the finite element framework of COMSOL Multiphysics™ (Multiphysics 1998) to solve the dimensionless transport equations with the boundary conditions mentioned above. The domain of computation is divided into triangular domain using the linear shape function for the transport variables. Moreover, the time-dependent segregated type solver is used to compute the velocity field and phase field parameter step-by-step rather than simultaneously. In the segregated stage, the parallel sparse direct solver (PARDISO) is used to compute the velocity, pressure and phase field parameter. Now, we

have presented the grid independent test, as shown in Fig. 3.4, by varying the Cahn number- a dimensionless number that measures the effective grid sizes in this endeavour. Hence, the depicted variation in Fig. 3.4 essentially underscores the effect of grid sizes on the results discussed in this study. We can see that the dynamical shape of the interface becomes independent of Cahn number as its value changes from 0.015 to 0.005. Following this observation, we have used *Cn* = 0.01 (YUE *et al.* 2010) for all simulations performed in this analysis to predict the results of our interest with optimized computational cost.

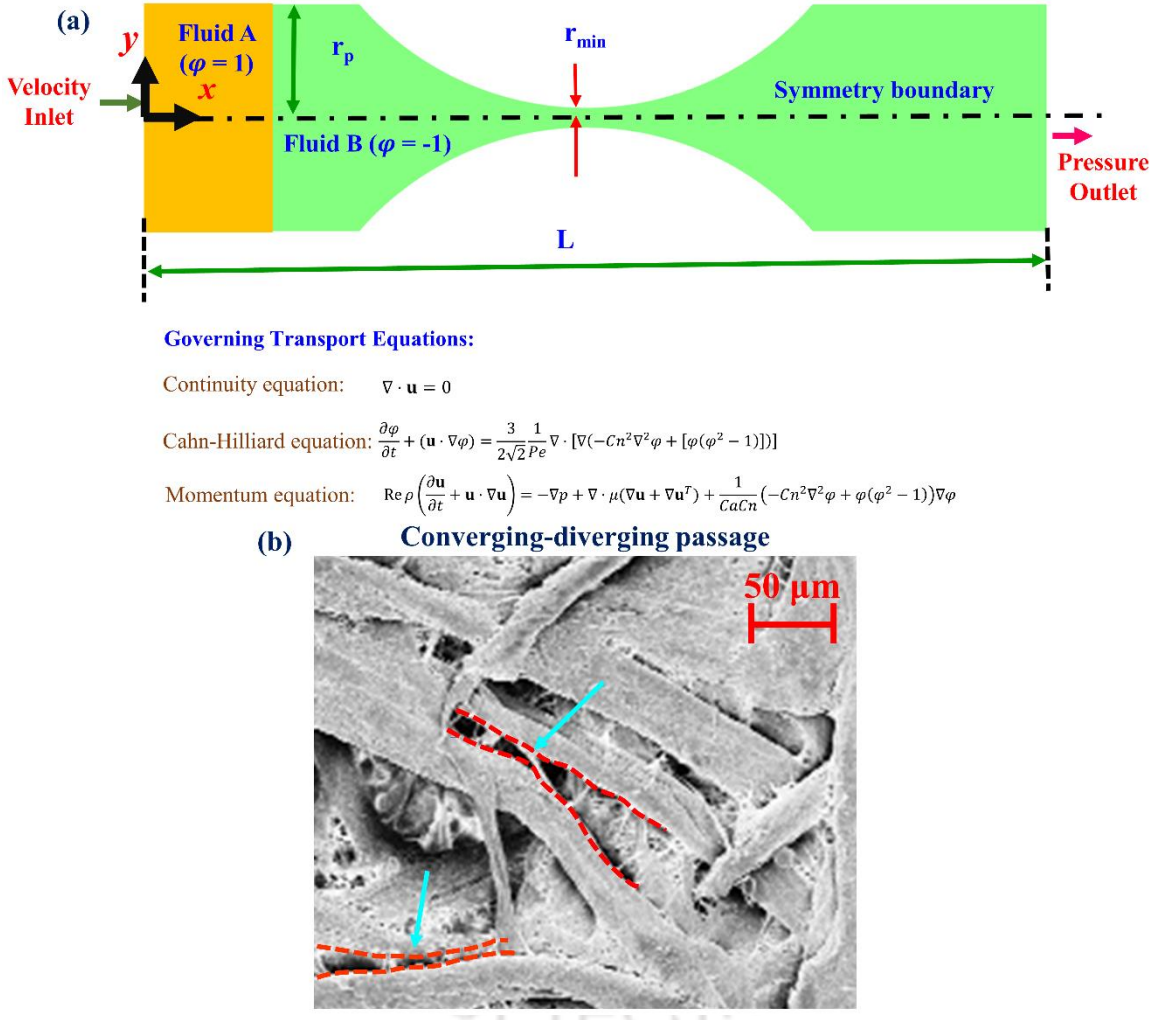

Figure 3.3. (a) Schematic of the solution domain showing the governing transport equations and the appropriate boundary conditions. (b) SEM image of the Grade 4 paper showing the converging-diverging passage in pore structure.

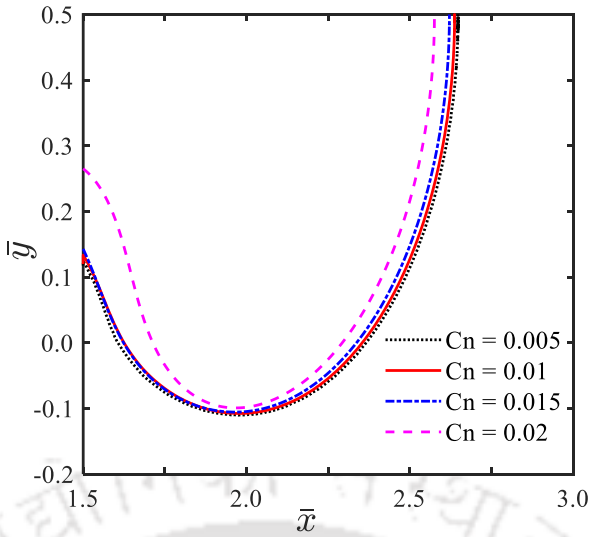

Figure 3.4. Grid Convergence test at different values of Cahn number.

3.4. RESULTS AND DISCUSSION

The innovative Y-shaped paper-based fluidic pathway facilitates precise and continuous droplet formation. The number and size of the generated droplets were examined by altering the paper type, width, and angle of inclination. Furthermore, we conducted a statistical analysis of the distribution of the droplet size and number in relation to the aforementioned input parameters.

3.4.1. Effect of paper type and oil-water mixture on saturation dependent capillary pressure

Droplet generation in a paper-based device occurs primarily due to the prevailing capillary pressure when oil and water come into contact. Accounting for this aspect, we first undertake an effort to analyse the saturation-dependent capillary pressure pertaining to the present flow configuration before moving on to the assessment of droplet generation dynamics. Figure. 3.5 depicts the saturation-dependent capillary pressure for three distinct cases: Milli Q water in Grade 4 paper, a 50-50% mixture of mineral oil and Milli Q water in Grade 4 paper, and a 50-50% mixture of mineral oil and Milli Q water in Grade 1 paper. Here, the saturation based capillary pressure is calculated using Eq. (3.1), which is derived from the double integral method. It is evident that when saturation levels rise, capillary pressure decreases. We attribute this observation to the existence of liquid filled pores in the flow pathway. Notably, some fraction of liquid filled pores resist formation of interface (liquid and air) to provide with the surface tension force in the underlying dynamics. It is observed that droplets generation continues up to the outlet of the fluidic pathway following

the availability of the water-oil mixture therein. This observation indicates that paper-based fluidic pathway is in a state of high liquid saturation. Consequently, in the inset of Fig. 3.5,

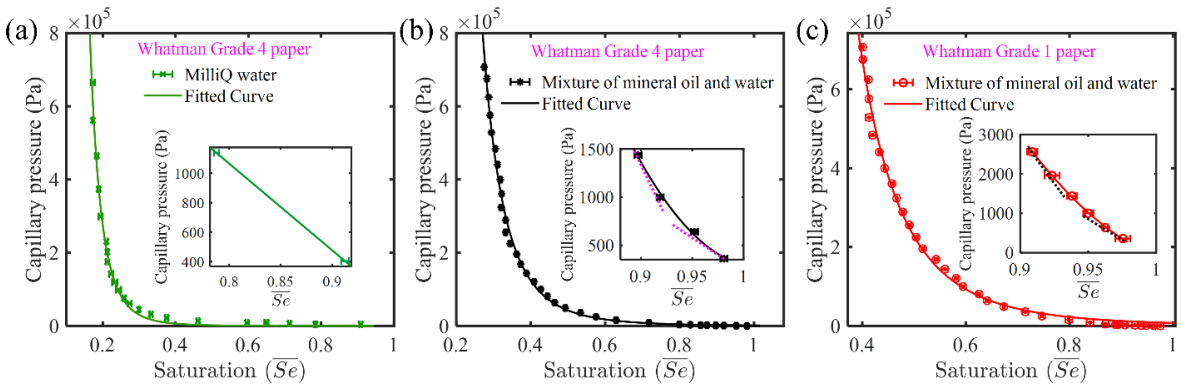

Figure 3.5. Variation of saturation-dependent capillary pressure (using double integral method) obtained via rotation effect for (a) Whatman® Grade 4 paper with Milli Q water, (b) Whatman® Grade 4 paper with mixture of mineral oil and Milli Q water and (c) Whatman® Grade 1 paper with mixture of mineral oil and Milli Q water.

- we have specifically shown the high saturation level regime. It is noted that the addition of oil with water (see Fig. 3.5(b)) allows higher capillary pressure as compared to the case with pure water (see Fig. 3.5(a)) at higher saturation level. This observation is attributed to the requirement for a higher centrifugal force to expel the oil-water mixture compared to water alone, primarily due to the increased viscous resistance provided by the oil. The capillary pressure is observed to be higher for Grade 1 paper [see Fig. 3.5(c)] than for Grade 4 paper (see Fig. 3.5(b)) at higher saturation levels of the oil-water mixture. The increased capillary pressure of Grade 1 paper is attributable to its smaller pore size (11.32 μm) relative to Grade 4 paper (23.4 μm). Consequently, the reduced pore size of Grade 1 paper facilitates an increased surface area to impede the flow of an oil-water mixture when subjected to centrifugal force. Consequently, a greater centrifugal force is necessary to expel the trapped air in Grade 1 paper compared to Grade 4 paper. Thus, Grade 1 paper exhibits a greater capillary force than Grade 4 paper at higher saturation levels for an oil-water mixture.

3.4.2. Liquid imbibition and droplet generation within the fibrous matrix of paper

Generating monodispersed submicron emulsions is challenging because of the substantial energy needed to make small droplets (Tan and Lee 2005). Furthermore, in a controlled experiment, it is crucial to have droplets that do not split or agglomerate over time (Yobas *et al.* 2006). We performed specialized tests of oil droplet generation on Y-shaped paper-based fluidic strip as discussed next.

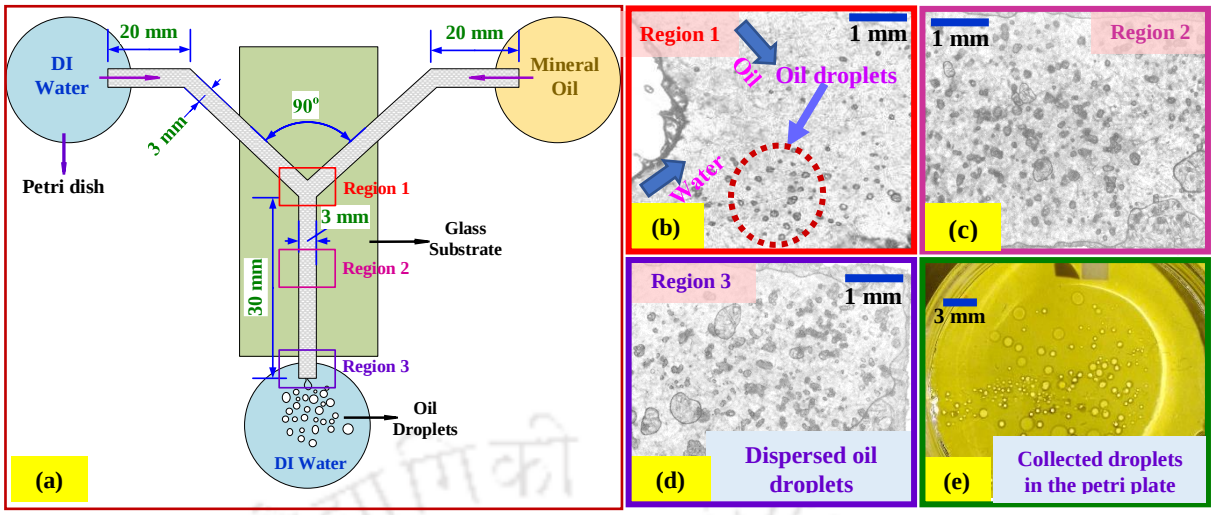

Figure 3.6. (a) Schematic depiction of the set-up for oil droplet generation using a Y-shaped Grade 4 paper strip: Microscopic zoomed view of the oil droplet transport in (b) Region 1, (c) Region 2, (d) Region 3 and (e) inside the petri plate at the outlet of the paper strip.

The spontaneous flow of the wetting liquid through the pores due to the capillary pressure is a highly desirable characteristic of a porous paper matrix. This characteristic feature greatly enhances the paper's ability to handle fluid flow effectively. A porous matrix consisting of a connected network of pore spaces and tortuosity can effectively facilitate the uptake of fluids into the porous material without requiring of any external driving mechanisms (Patari *et al.* 2023; Toley *et al.* 2018). Hence, the Grade 4 paper, as shown in Fig. 3.6, is able to generate the oil droplets because of the capillary pressure (see Fig. 3.5(b)) driven flow of Milli Q water and mineral oil (see Fig. 3.6(a)). It is noted that the oil droplet starts forming at the junction region, called region 1. Due to the capillary force, oil droplets start moving towards the region 3 followed by region 2. Interestingly, it is observed in Figs. 3.6(b) - (d) that the droplets size in paper fluidic strip becomes higher as they move from region 1 to region 3. This observation can be attributed to the enhanced residence time of the droplets because of the reduced capillary pressure owing to the enhancement in saturation level (see Fig. 3.5(b) as they move from region 1 to region 3. The higher residence time allows merging the droplets to become larger in size. Hence, we have critically discussed the phenomenon of merging of the generated droplets in the forthcoming paragraph. Finally, the transported droplet due to the capillary action is collected in petri dish as shown in Fig. 3.6(e).

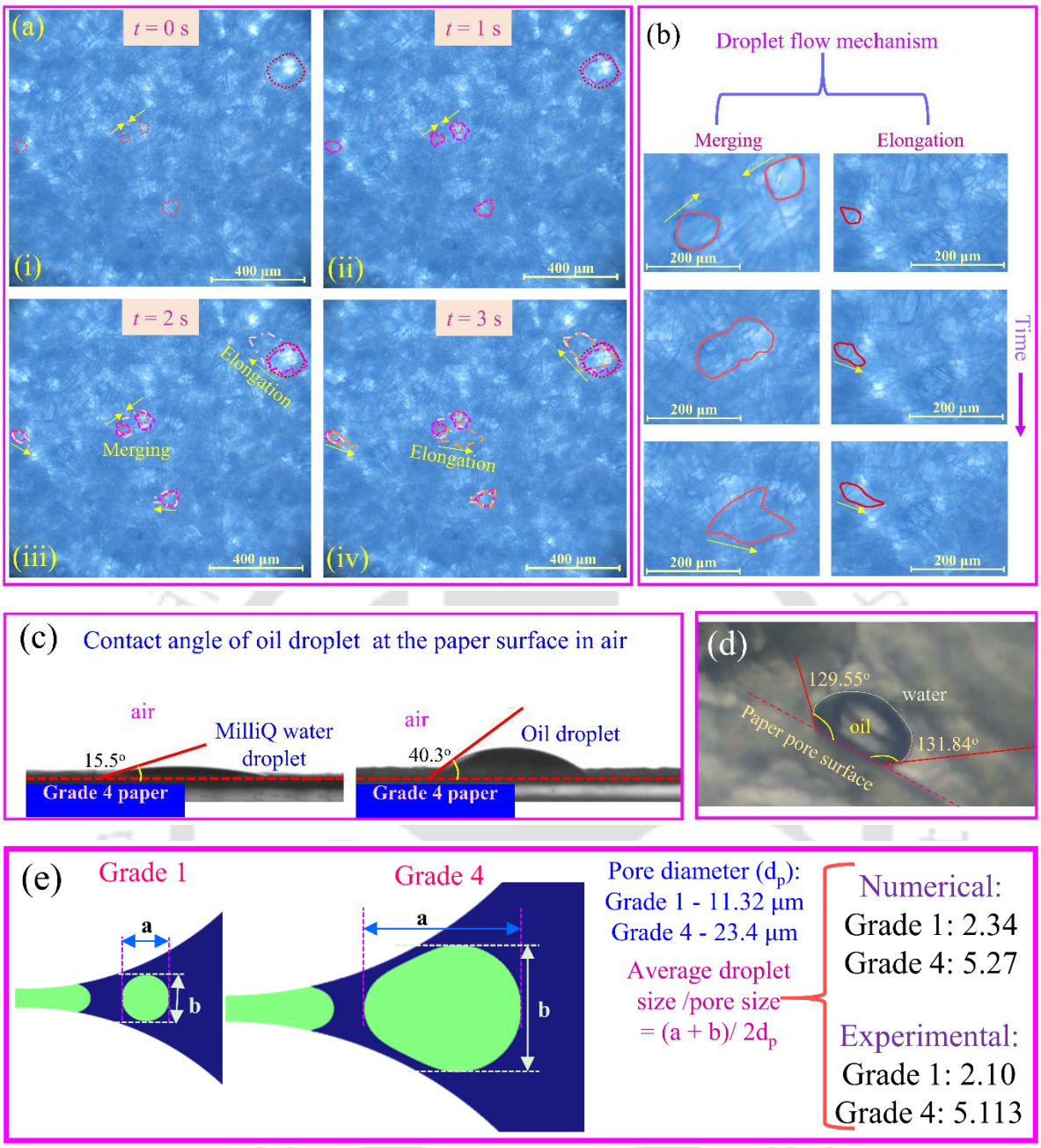

Figure 3.7. (a) Real-time flow images corresponding to Region 2 of Y-shaped Grade 4 paper strip showing the temporal evolution of oil droplets in the porous paper at (a) t = 0 s, (ii) t = 1 s, (iii) t = 2 s and (iv) t = 4 s showing the elongation and merging of oil droplets. (b) The clear view of temporal oil droplet merging and elongation in paper-based porous media. (c) Contact angle obtained for Milli Q water and oil droplet on Grade 4 paper at the end of 80 ms after the contact in air. (d) Contact angle depiction of oil droplet at pore surface in water medium obtained from microscopic image (e) Droplet size prediction from numerical simulations consistent with the phase-field model for Grade 1 and Grade 4 paper pores.

To see the underlying mechanism of droplet formation in paper-based fluidic strip, we have shown the temporal evolution of oil droplets in Fig. 3.7(a). We have observed two types of important mechanisms which also helps to transport droplets along with the

capillary force. These two mechanisms are merging and elongation of the droplets. As shown in Fig. 3.7(b), the droplet merging is possible because of the oleophobic nature of Grade 4 paper having cellulose-rich content. For Grade 4 paper with oil and Milli Q water droplet, three phase contact angles are found to be 40.3^{o} and 15.5^{o} respectively, (see Fig. 3.7(c)), measured in air after 80 ms of contact of oil droplet on pore surface. It is important to clarify that these are transient advancing contact angles; the higher value for oil at this instant is attributed to its higher viscosity delaying the spreading process. Which means oil has relatively less philic nature as compared to the Milli Q water for Grade 4 paper. Therefore, as shown from Fig. 3.7(d), the oil droplet has higher contact angle at the pore surface surrounded by water. Hence, oil droplets are formed due to the oleophobic condition at surrounding and undergoes deformation and merging. The two oil droplets, closer in the pore site, are able to flow because of the prevailing capillary force generated between micro-sized capillaries and gets merged. Afterwards, the merged larger droplet elongates under the capillary flow of continuous phase water.

Moreover, we compared the relative size of the formed droplet derived from the numerical simulations as depicted in Fig. 3.7(e). It may be mentioned here that we have employed the phase-field model in this endeavour to simulate the droplet generation phenomenon (refer to Section 3.3). It is worth to mention here that the droplet generation inside the pore nearly follow the Roof criteria as discussed in the subsequent sub-section. We can clearly see that relative size of the droplet after generation in pore site of the fluidic pathway matches the numerical results for both Grade 1 and Grade 4 paper pores. Consequently, the related local phenomenon of droplet generation can be elucidated using simulated results, as discussed in the subsequent paragraph.

Additionally, in the present study we have not observed any significant swelling of the porous paper strip during the co-wicking of the mineral oil + Milli Q water in the microscopic pore images of the paper strip before and after the biphasic flow. According to literature,(Chang and Kim 2020; Lioumbas *et al.* 2013) water as a polar liquid can cause swelling in cellulose fibres through hydrogen bonding, while non-polar liquids such as oils have limited interaction with cellulose due to the lack of such bonding. In the case of co-wicking, oil presumably mitigates the water swelling by partially filling the pore network and limiting extensive fibre hydration.

3.4.3. Droplet generation in pore: Relevance of Roof criteria

To simulate the oil droplet generation in numerical model, we have taken a converging-diverging shape (see Fig. 3.3 (a)) – a shape of the pore structure obtained from SEM imaging, as shown in Fig. 3.3 (b). The throat radius (r_{min}) of the converging-diverging pore pathway is an important parameter for the generation of droplets following snap-off phenomenon as per the Roof criteria (Roof 1970). According to Roof criteria (Roof 1970), the droplet snaps off from the liquid stream when the evolving droplet curvature radius (r_d) becomes twice the radius of the throat, i.e., $r_d = 2r_{min}$. In order to determine the throat radius, we have obtained the radius of the pore constriction from SEM imaging (see Fig. 3.8 (b)) of the transverse section of the Grade 4 paper and the distribution of the same has been given in the Fig. 3.8 (a).

Figure 3.8(c) shows the 2D and 3D views of the droplet generation from three different normalized values of throat radius r_{min}/d_p= 0.03, 0.045 and 0.06, respectively. The variation of the normalized droplet (generated after the throat) radius with the normalized throat radius is demonstrated in Fig. 3.8 (d). This observation shows that the chosen throat radius (r_{min}) is in nearly accordance with the Roof criteria (Roof 1970) for droplet snap-off (Armstrong *et al.* 2016). Hence, for the representative cases of different throat radii considered for this endeavour, which are consistent with the SEM imaging as well (see Fig. 3.8 (b)), pore structure is deemed capable to produce droplets as we experimentally found (see Fig. 3.7 (a)).

3.4.4. Effect of paper strip orientation on the droplet generation

In Fig. 3.9, we have shown the effect of gravity and the distribution of droplet generation in terms of number and size in the porous structure of the chosen paper strips. We found that with increase in the inclination of the paper strip from 0^o and 10^o, the weighted average of diameter decreases from 0.8323 ± 0.00216 mm to 0.5716 ± 0.00119 mm. This observation can be attributed to the combined effects of gravity as well as capillary force acting in tandem on the droplet formation dynamics as well as underlying water transport. The values of Bo_θ obtained by varying the inclination angle for Grade 1 paper is presented in Section 3.2.5. We can clearly see that the non-zero value of Bo_θ at $\theta = 10°$ enables a smaller average droplet size. This happens because the droplets are able to overcome the adhesive forces (retaining force) more quickly due to the enhanced detaching force stems from the contribution of gravity on wetting liquid, water (see Fig

3.2). It is owing to the larger density of water as compared to oil allows more gravitational forcing to act on the wetting phase liquid, i.e., water. Furthermore, as elaborated in the next paragraph, larger inclinations with θ greater than 10^{o} do not produce any micro-sized droplets.

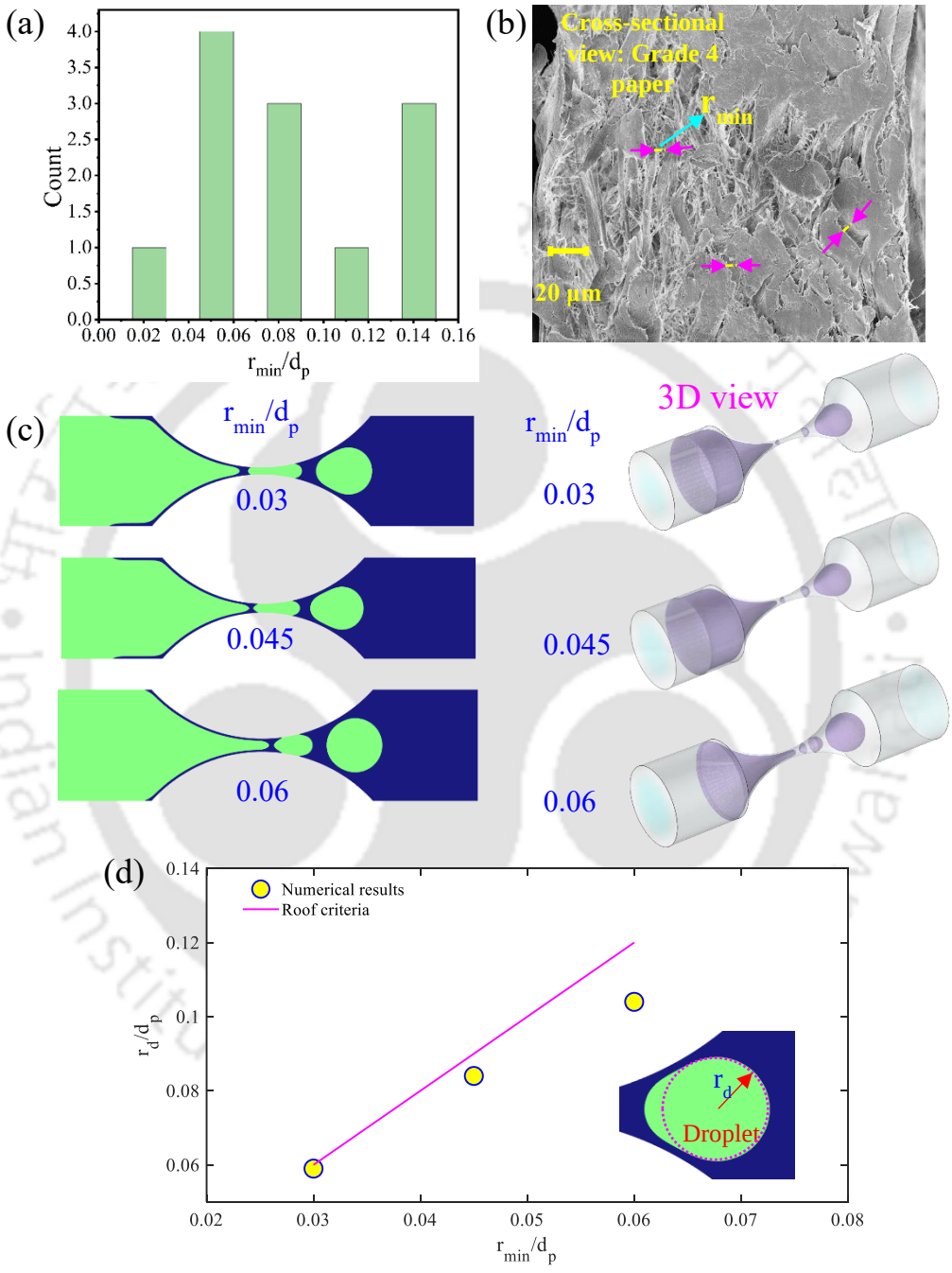

Figure 3.8. (a) Distribution of the minima pore size obtained from (b) SEM image. (c) Droplet generation obtained from the numerical simulation by varying r_p in 2D and 3D view. (d) Variation of normalized droplet curvature radius (r_d/d_p) after throat by varying the throat radius which is nearly consistent with Roof criteria.(Roof 1970)

We varied inclination angles (for paper strip) as 0°, 5°, 10°, and 20° and examined the droplet generation morphodynamics. It has been observed from Fig. 3.10 that droplet size decreased progressively with increasing inclination from 0° to 5° to 10°. However, the variation in droplet size between 0° and 5° was minimal. Additionally, increasing the inclination to 10° resulted in smaller droplet diameters. This trend can be explained by the Bond number (Bo_θ), which at 10° is approximately twice that at 5°, indicating a stronger influence of gravitational forces. At 10°, the enhanced detachment force arising from gravity acting on the wetting liquid, water facilitates faster droplet release (see Fig. 3.2).

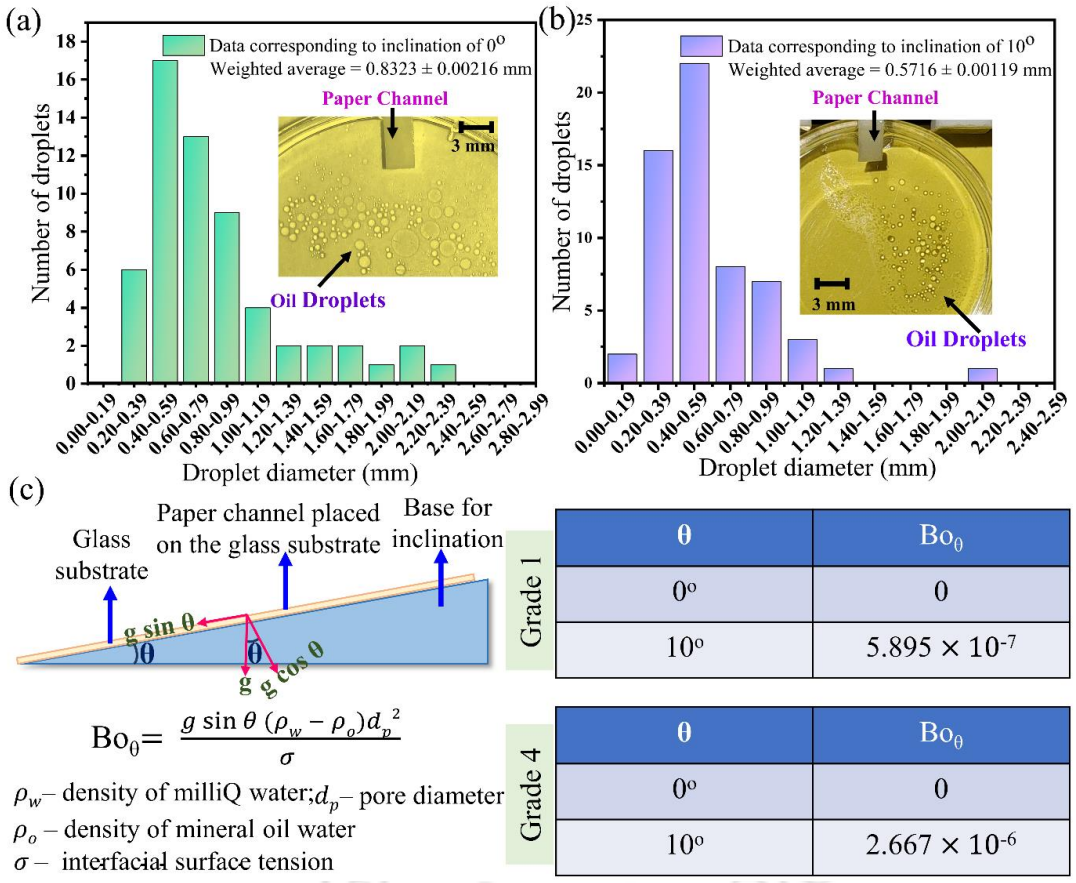

Grade 1

θ	Bo_θ
0°	0
10°	5.895×10^{-7}

Grade 4

θ	Bo_θ
0°	0
10°	2.667×10^{-6}

Figure 3.9. Plots showing the distribution of number of droplets collected and its size in the petri plate generated from the microporous structure of the paper strip when (a) paper channel is horizontal, (b) paper channel is 10° with the horizontal, (c) tabulated Bond number values (Bo_θ) for Grade 1 and Grade 4 paper at different inclination angles (0° and 10°).

When the inclination was further increased to 20°, the oil phase no longer formed discrete droplets but instead developed into a continuous film at the outlet in the Milli-Q water Petri dish as shown in Fig. 3.10 (d). At this angle, the Bond number increases by an order of magnitude compared to 10° (see Section 3.2.5), indicating that gravitational forces now overpower the interfacial retention forces within the pore structure. Additionally, the

residence time becomes too short for neck formation, a critical step in droplet pinch-off, thereby preventing the generation of discrete droplets and resulting in continuous film formation. Hence, from the aforementioned discussion it can be concluded that the droplet generation method from the porous paper strip can be valid upto ~ 10^o inclination.

Consequently, the droplets detach from the pores more rapidly, and get less residence time for merging to form a relatively bigger droplet. Hence, the reduced merging effect results in decreased average droplet size at $\theta = 10°$ as compared to $\theta = 0°$. Also, the enhanced detaching force on droplet as well as enhanced driving force of wetting phase liquid (water) help generation of large number of droplets with average size (see Fig. 3.9a and 3.9b). The larger average pore size of Grade 4 as compared to the Grade 1 paper results in higher magnitude of Bo_θ for Grade 4 paper, as shown in Fig. 3.9(c). From the aforementioned discussion, we can deduce that the fluidic pathway configuration with inclination angle of 10^o is able to produce greater number of uniform sized smaller droplets in the petri dish. It is worth adding here that the smaller droplet sizes enables the reactions at volumes comparable to biologicals activities in cells and may allow precise control over biochemical analyses (Tangen *et al.* 2015). Hence, we have taken 10^o inclination of paper strip for further analysis in this study. It is noted that the percentage deviation in droplet sizes in batch to batch variability is ± 2.31 %, whereas the percentage deviation within batch variability is ± 1.76 %.

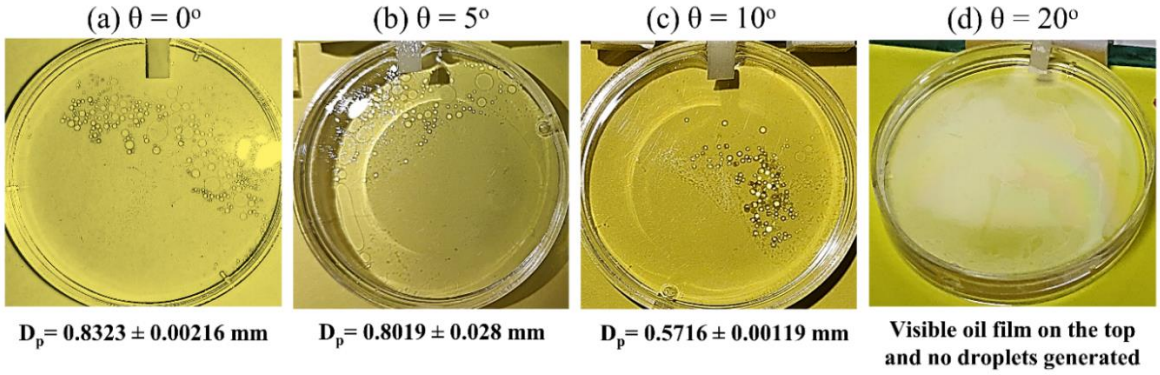

Figure 3.10. Effect of channel inclination angle on droplet generation: (a) θ = 0°, (b) θ = 5°, (c) θ = 10°, and (d) θ = 20°

3.4.5. Effect of oil inlet width and paper strip width on the droplet generation

We have shown, in Fig. 3.11, the effect of width of the oil inlet part of the fluidic pathway on the distribution of droplets generated from the Grade 1 paper strip. As the width of the oil inlet part increases, the average size of the droplets decreases significantly. This can be attributed to the increase in capillary driving force when the oil mixes with water in the paper strip (see Fig. 3.5a and 3.5c). An increase in width (oil inlet part) provides a

greater number of pores for oil transport. Which allows increase in capillary pressure because of the larger fraction of oil as compared to water on wider oil inlet paper strip. Therefore, the increased capillary pressure increases the flow rate at larger widths. Thus, the increased detaching force facilitates a swift generation of smaller-volume droplets in a reduced time span for larger oil inlet width part of paper fluidic strip. Important to add, the micro-sized droplet generation observed in our study (~ 357.5µm) corresponds to existing findings on droplet formation in conventional microchannels as well (Jena *et al.* 2023). Hence, we can say that the low-cost simple paper-based fluidic strip is able to generate micro-sized droplet at very low-cost when compared to costly conventional microfluidic device assisted droplet generators (Jena *et al.* 2023).

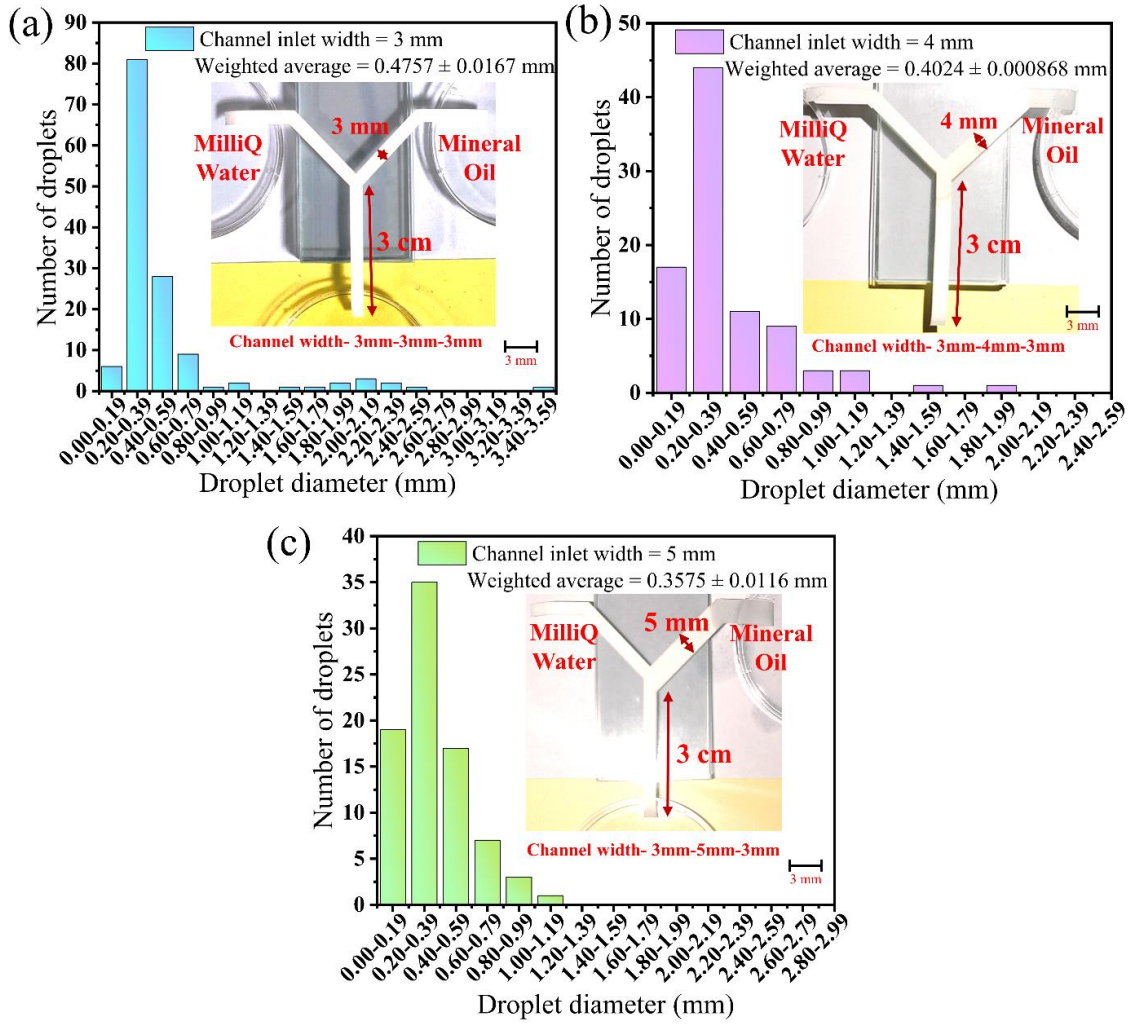

Figure 3.11. Plots illustrating the distribution of number of droplets collected in the petri plate by the microporous structure of the paper fiber. Images were obtained for three different widths of the oil inlet arm of the 'Y' channel, (a) 3 mm, (b) 4 mm, and (c) 5 mm. Here, Grade 1 paper has been used to generate the droplets.

Subsequent to the discussion on the oil inlet width, we demonstrated how paper dimensions impact droplet generation with inlet and outlet widths of 3 mm, 4 mm, and 5 mm in Fig. 3.12. It has been found that micro-sized droplets develop only when the paper width is 3 mm. Whereas, no micro droplets are generated at wider widths (4 mm and 5 mm). The larger the number of pores, the stronger the capillary force and the intensity of the flow field inside the paper strip. Consequently, the oil droplet at the pore throats has a shorter residence period due to the stronger flow field. Because of the shorter residence period, the oil stream travels directly to the outlet without generating any droplets. Furthermore, the longer residence time because of the considerably weaker capillary force due to the smaller number of pores for a 3 mm paper strip width confirms droplet generation. We found that paper strip with 3 mm width facilitates droplet generation, while paper strip with bigger widths does not produce any micro-sized droplets.

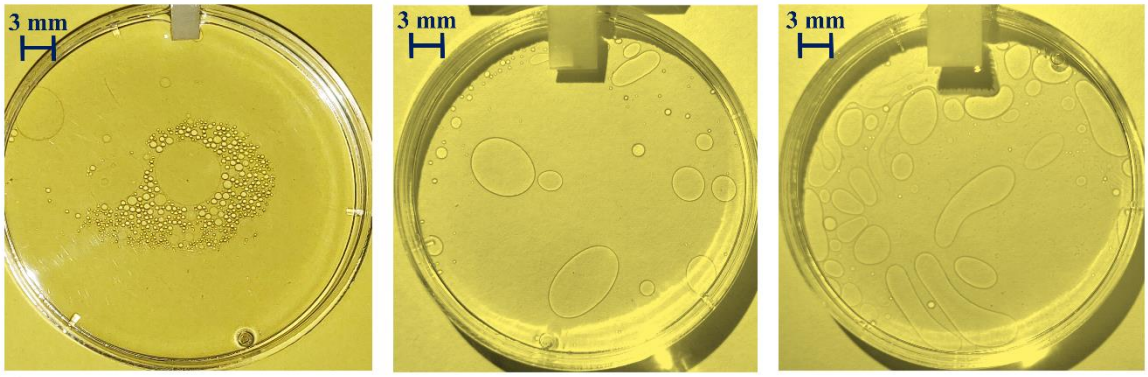

Figure 3.12. Effect of paper dimension on droplet generation: (a) 5 mm, (b) 4 mm, (c) 3 mm. Droplet size decreases significantly as channel width decreases

3.4.6. Temporal distribution of collected droplet

We have shown, in Fig. 3.13(a), the cumulative number of collected oil droplets for each 5 s. Note that the data presented in Fig. 3.13 were obtained using the fluidic pathway fabricated on Grade 1 paper. We found that the cumulative droplet generation enhances with time and gets constant at higher time steps. It is attributed to the existence of capillary force until the paper fluidic strip gets fully saturated (see Fig. 3.5). Hence, the capillary force is able to generate the droplets up to ~ 95 s because of the existence of driving capillary force. Whereas, the absence of capillary driving force allows constant number of droplets at time instance greater than ~ 95s. Moreover, for better visualization on understanding of the temporal droplet generation, the number of generated droplets for each

5 s is shown in Fig. 3.13(b). It is observed that number of generated droplets for each 5s is very high and nearly constant in regime I. The dominating role of higher magnitude of capillary pressure at relatively lower saturation level in the strip (see Fig. 3.5) allows higher driving force and produce greater number of droplets. This regime signifies the high droplet generation rate. In regime II, the reduced capillary pressure (see Fig. 3.5), primarily because of the enhancement in saturation level, sharply reduces the number of droplets for each 5s. This regime signifies the reduction in temporal droplet generation rate. On the other hand, the paper gets fully saturated in regime III with zero capillary pressure (see Fig. 3.5). Hence, the absence of the driving force does not generate any further droplets in regime III. Moreover, the isolated droplet can be storage for the further application using 96 wells culture plate as presented in Section 3.4.9.

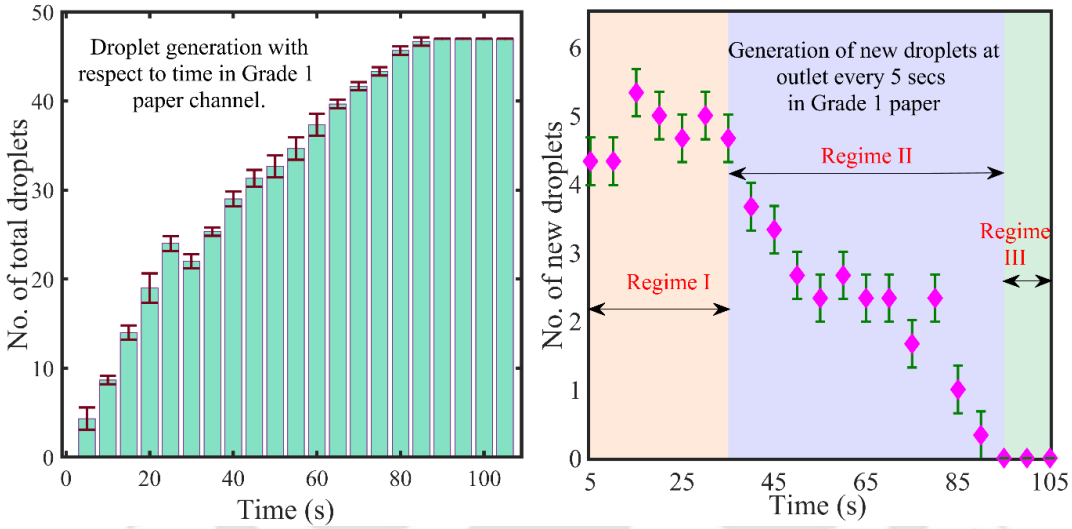

Figure 3.13. (a) The change in cumulative number of the droplets in petri plate over each 5 s for Grade 1 paper strip with an inclination of 10°; (b) Plot depicting the number of droplets collected in petri plate for each 5 s using Grade 1 paper strip.

3.4.7. Effect of paper type on droplet generation

The influence of paper type on droplet size distribution is illustrated in Figs. 3.14(a) and (b). The wetted average droplet size is smaller for Grade 1 paper fluid strip than for Grade 4 paper strip. This finding is attributed to the smaller pore size of Grade 1 paper (11.32μm) compared to Grade 4 paper (23.4μm), which facilitates higher capillary pressure to prevail, as illustrated in Fig. 3.5(b) and (c). The intensity of axial surface tension force is greater in Grade 1 paper pore than in Grade 4 paper pore (see Fig. 3.14(c)). Consequently, the droplet exhibits significantly higher pressure near the throat in Grade 1 paper pore compared to Grade 4 paper pore, as displayed in Fig. 3.14(d). The increased magnitude of the detaching force, mainly due to the elevated axial surface tension force, facilitates rapid

detachment of smaller oil droplets in Grade 1 pores. Consequently, as witnessed in Fig. 3.14(d), the size of collected oil droplets generated from Grade 1 paper strip is found to be smaller in size.

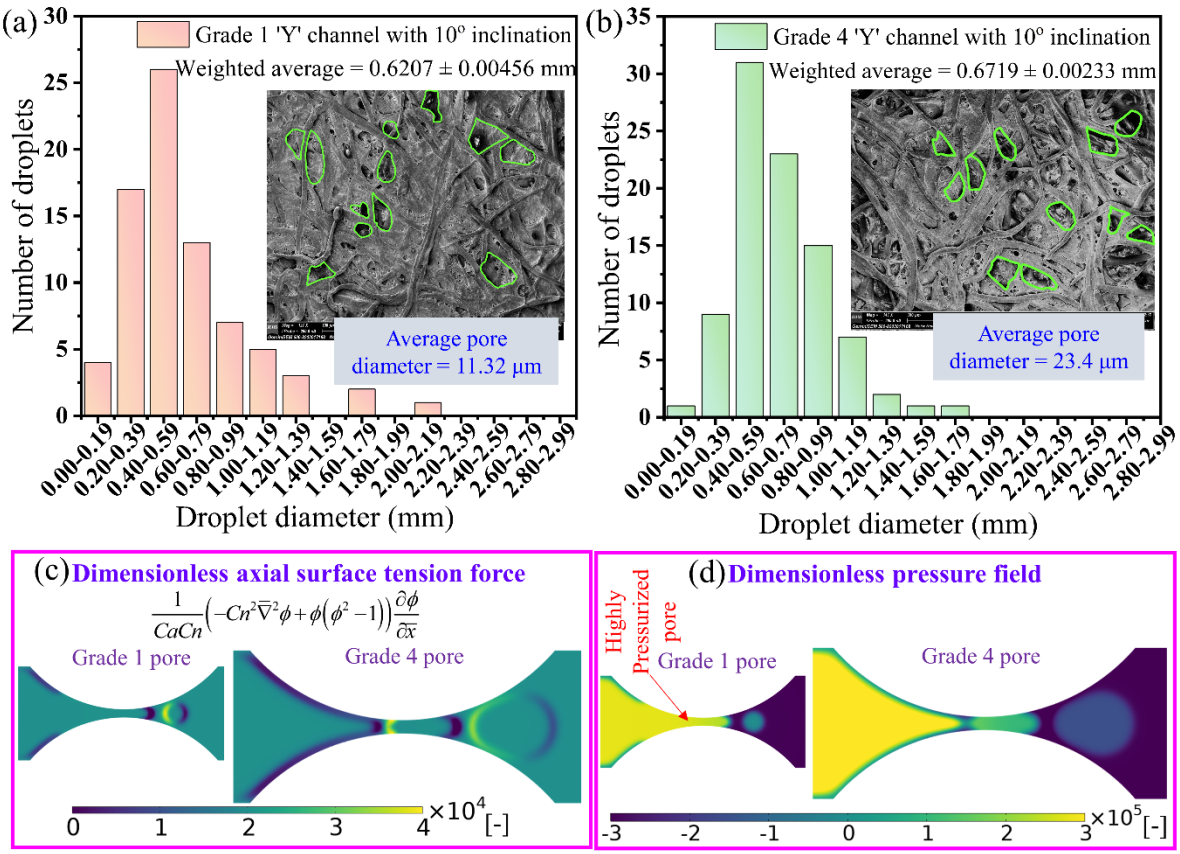

Figure 3.14. Plots depicting the distribution of the number of droplets collected and droplet size in the petri plate and inset SEM images for: (a) Grade 1 paper channel with 10° inclination and (b) Grade 4 paper channel with 10° inclination. (c) Dimensionless axial surface tension contours for Grade 1 and Grade 4 pores, (d) Dimensionless pressure field contours for Grade 1 and Grade 4 pores.

The isolation of micro-sized cells for biological research is performed using micro-sized droplet (Joensson and Andersson Svahn 2012; Lagus and Edd 2013; Rakszewska *et al.* 2014). Thus, the stability of micro-sized droplets is crucial. Hence, the size distribution and stability of droplets significantly influences the usefulness and desirability of the outcome of this endeavour. To ascertain that, we have compiled temporal change in the number and size of generated droplets for two different cases as follows. Figures 3.15(a) and (b) demonstrate the temporal fluctuation in average droplet size at three distinct time points (t = 50, 100, and 150 s) for two inclinations (θ = 0° and 10°) and two paper grades (Grade 1 and Grade 4), respectively. It is noted that for the three different time intervals, t = 50, 100, and 150 s, the mean diameter of the droplets remains nearly unchanged for both

cases of inclination and paper grades. The droplet size is crucial for targeted genomic research utilizing micro-sized droplets. Consequently, the micro-sized droplet produced in the current investigation using a cost-effective process may be beneficial for biological applications, including cell analysis (Mastiani *et al.* 2019; Matuła *et al.* 2020; Zhang *et al.* 2024).

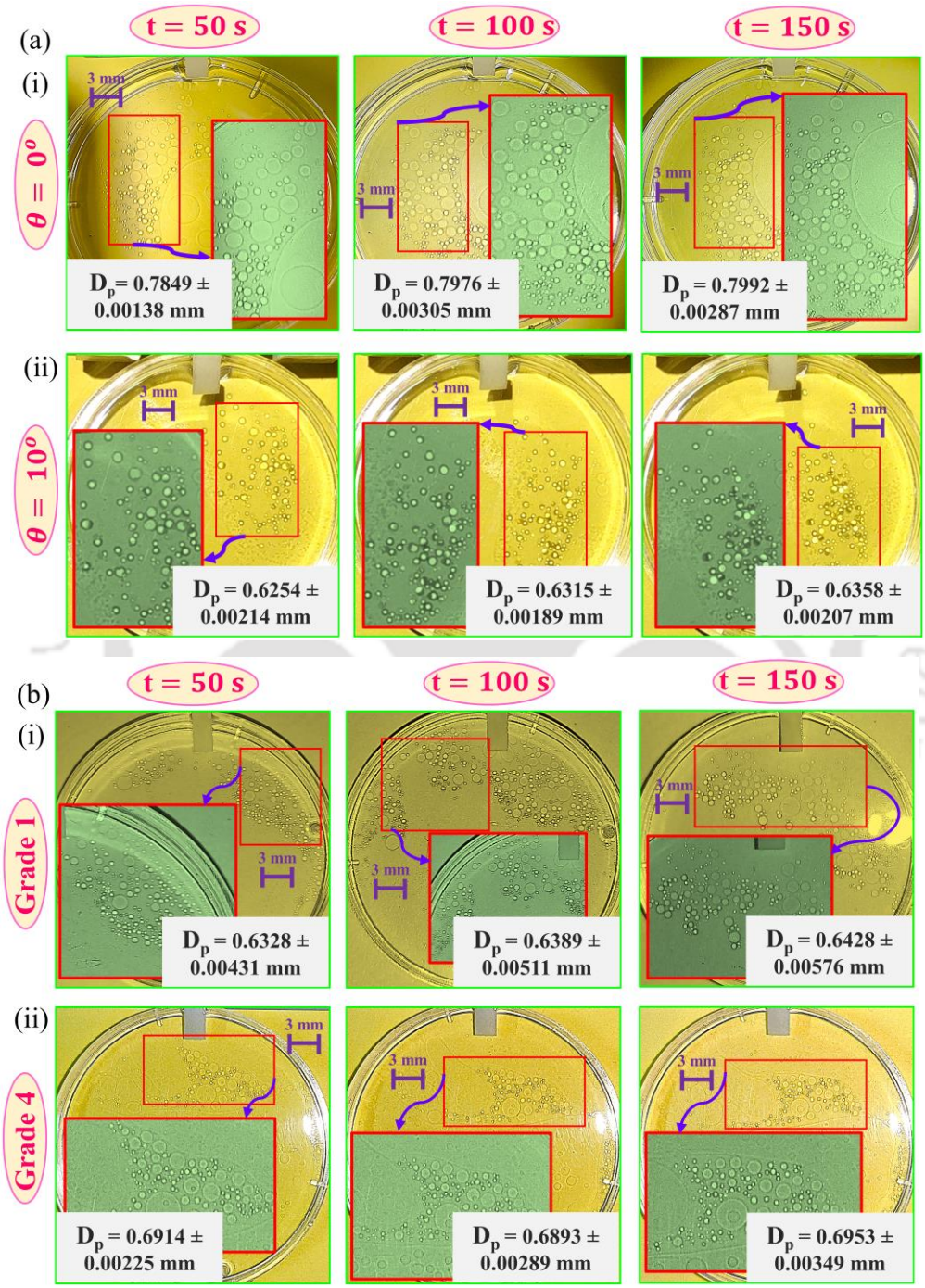

Figure 3.15. (a) Temporal visualization of generated droplets with change in inclination, (b) temporal variation of generated droplet with change in paper type.

3.4.8. Encapsulation of micro-sized species in generated droplets

The biological community is becoming more intrigued in studying micro-sized (~3-5 μm) (Nakai 2020) biological species, including bacteria, fungus, yeast, and algae, in micro-sized droplets (Postek and Garstecki 2022; Ramos *et al.* 2020; Shih *et al.* 2014). The micro sized droplets act as an confined environment and the porous substrate mimic their natural habitats where microbes are capable of surviving in both organic and inorganic porous media owing to their unique biophysical characteristics for active and passive nutrient transport (Jin and Sengupta 2024)·(Sengupta *et al.* 2022). Droplets serve as an exciting platform for high-throughput screening, sample preparation in multiparameter analysis of microbes and automation in medical diagnostics (Leung *et al.* 2012). Hence, we have taken an effort to analyse the encapsulation of micro sized (~5 μm) particle (Polystyrene micro particle, Sigma Aldrich). Mineral oil with 0.1 mg/ml polystyrene micro-particles were taken in an eppendorf tube and vortexed the mixture for 10 minutes using SPINIX™ Vortex Shaker. The mixture is subsequently sonicated to break down any aggregates and form a uniform suspension. The mineral oil containing suspended polystyrene micro particles has been introduced to the right arm of the Y- shaped paper channel (c.f. Fig. 3.6). The intrinsic capillary pressure draws the mineral oil with suspended polystyrene micro particles into the pores of the paper channel. Figure. 3.16 depicts the generated droplets encapsulating the polystyrene micro particles; the left of the image specifically showing a single oil droplet containing entrapped microparticles. The micro particles encapsulated oil droplets serve as an experimental analog for the lipid droplets that are essential for the biological species or microbes for the active and passive nutrient uptake.

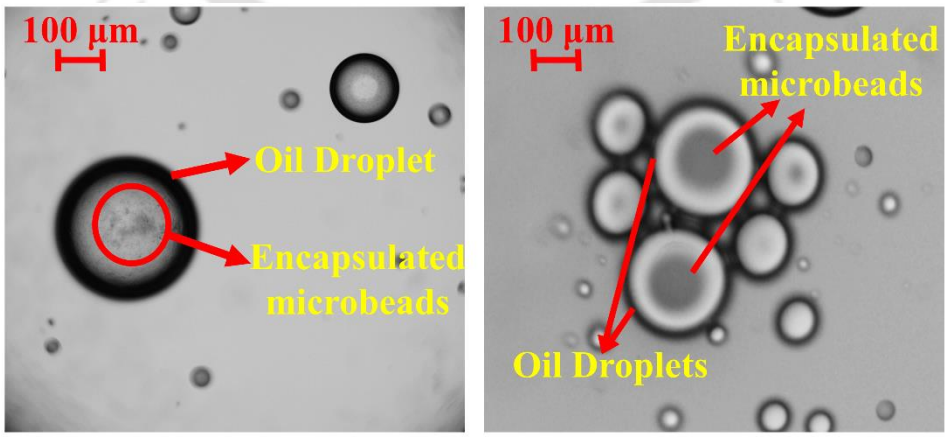

Figure 3.16. The microscopic image of a single droplet shows the encapsulated micro particle in the mineral oil droplets (left). The right-side microscopic image shows multiple oil droplets with micro particles in the center of the oil droplets.

3.4.9. Isolation and storage of droplets in 96 wells culture plate

We have used a 96 wells culture plate for the isolation and storage of droplets as shown in Fig. 3.17. The mineral oil has been dyed using a 0.1 mg/ml solution of Nile red as the oil is naturally colourless. Nile Red is a hydrophobic dye widely utilized for identifying oil droplets and quantifying intracellular lipid levels across various biological systems (Greenspan *et al.* 1985; Tan *et al.* 2005; Yan *et al.* 2013). This facilitated the imaging further to examine the droplets. The droplets were collected and separated in four wells of a 96-well culture plate and closely examined for 5 hours. The droplets retained their spherical shape and exhibited no variation in size during the observation period as shown in Fig. 3.17. This verifies that the droplets are stable and can be effectively separated for further use.

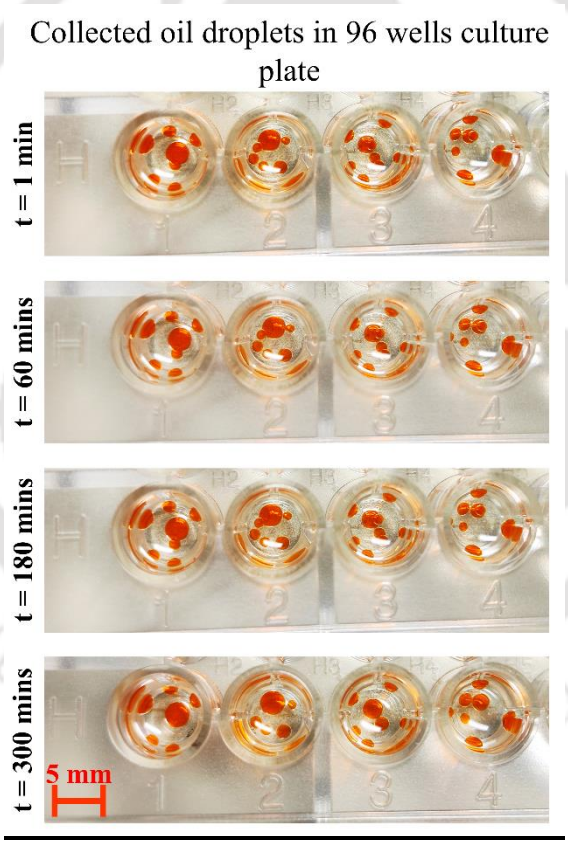

Figure 3.17. Images depicting oil droplets stained with Nile Red, successfully separated in a 96-well culture plate. The droplets retain their spherical form and exhibit prolonged stability for 5 hrs, verifying their suitability for further use.

3.5. CONCLUSION

The current innovative method generates microscale droplets utilizing a 'Y'-shaped porous paper strip, eliminating the need for external devices. We utilized Grade 1 and Grade 4 paper for the generation of micro-sized oil droplets due to the capillary forces

induced by water wicking. The microscopic images were used to analyze these oil droplets. The droplet size distribution was examined through changing the paper type and the inclination angle of the paper strip. Compared to using only water as the flowing medium, we found that the capillary pressure of the water–oil combination increases in the paper strips at higher liquid saturation levels. In addition, the capillary pressure in Grade 1 paper exceeds that in Grade 4 paper under these conditions. These micro-sized droplets are produced within the pores and transported toward the outlet through two primary mechanisms: merging and elongation of oil droplets facilitated by water wicking. The gravitational force significantly reduces droplet size with notable homogeneity. Subsequent observations indicate that an increased oil inlet width leads to a reduced droplet size of approximately 357.5 μm for a width of 5 mm. We identified three distinct regimes of temporal droplet production depending on the pattern of saturation-dependent capillary pressure. The size of droplet formation is significantly influenced by the type of paper, with the smaller pore size of Grade 1 paper enabling the formation of smaller droplets. We additionally developed a numerical framework to illustrate the local axial surface tension forces and pressure fields within the pores of Grade 1 and Grade 4. Moreover, we demonstrated the temporal stability of the droplet, which is pertinent for cellular research. Finally, we showed that the polystyrene micro particles, which resemble biological entities, are encapsulated in oil droplets. In summary, the findings of this study offer a cost-effective approach for producing micro-sized droplets suitable for biological and chemical analyses of micro/nano-sized targeted analytes. Nonetheless, the integration of analytes with the collected droplets is considered a significant challenge in the current design, warranting further investigation.

CHAPTER 4

EXPERIMENTAL AND SATURATION-BASED NUMERICAL INVESTIGATION INTO RHEOLOGY-DRIVEN WICKING DYNAMICS AND ANALYTE TRAPPING IN PAPER-BASED LATERAL FLOW ASSAYS

This chapter explores the rheology-modulated imbibition and analyte entrapment in paper-based porous media employing non-Newtonian fluids, namely NaCMC solutions and human blood. The research investigates the influence of shear-rate-dependent viscosity, saturation-dependent capillary pressure, and pore-scale fluid–substrate interactions on wicking dynamics and flow heterogeneity. A saturation-dependent numerical model is combined with an analytical framework based on effective viscosity to predict imbibition behavior. Additionally, the mechanisms of analyte transport and trapping are carefully examined through diffusion, interception, and inertial effects. Quantitative design criteria for effective lateral flow tests handling non-Newtonian biofluids are presented, along with the effects of fluid rheology and hematocrit level on entrapment probability and ideal test-line placement.

4.1. OBJECTIVE

In lateral flow assays (LFAs), the efficacy of test-line design is primarily dependent on regulated wicking behavior and analyte retention within the paper strip. Numerous diagnostic fluids utilized in LFAs have non-Newtonian characteristics, which can markedly affect capillary-driven transport and analyte retention. Blood exhibits shear-thinning properties influenced by hematocrit levels (Mehri *et al.* 2018), saliva displays non-Newtonian behavior due to dilute polymeric mucin chains, and polymeric solutions like sodium carboxymethyl cellulose (NaCMC) manifest non-Newtonian rheology resulting from long-chain molecular interactions. The rheological effects influence flow resistance, local shear rates, and pore-scale interactions, thus altering wicking dynamics and residence time inside the porous paper matrix. Therefore, comprehending rheology-modulated imbibition is crucial for enhancing analyte transport and retention in LFAs.[3]

[3] Content of this chapter is published in the journal of **Physics of Fluids (AIP), Volume 38, Issue 1, Page 012105, January 2026,** https://doi.org/10.1063/5.0305401

Conventionally, the wicking process in paper-based porous medium is characterized by the Lucas–Washburn equation or Darcy's law; however, both models are predominantly relevant at fully saturated circumstances. Given that capillary pressure is significantly influenced by liquid saturation, the Richards equation offers a more suitable framework for modeling partially saturated flow, with saturation-dependent capillary pressure often characterized by Brooks–Corey or van Genuchten correlations. Experimental studies have shown that analyte concentration considerably affects permeability and regulates analyte retention at particular axial positions, which is essential for optimal antigen-antibody interaction at the test line. Although these effects have been investigated for Newtonian fluids, their cumulative impact on non-Newtonian wicking and analyte entrapment in paper strips has yet to be examined. This study addresses the gap by examining rheology-modulated imbibition and analyte retention in paper-based fluidic channels utilizing NaCMC solutions and human blood through experimental, theoretical, and computational methodologies.

4.2.MATERIAL AND METHODS

4.2.1. Materials

For the wicking experiment, we consider Whatman^{TM} gel blot paper (GB003), cut into T-shape (cf. Fig. 4.1), as the paper substrate. The width of the paper strip is 0.8 mm. As shown in Fig. 4.1, an acrylic well has been attached to the glass slide with a slot to hold the T-shaped paper strip, placing its head inside the well. We consider aqueous solution of Carboxymethylcellulose sodium salt (NaCMC; Himedia) and human blood sample as the non-Newtonian fluid in the present study. We prepared NaCMC solutions by stirring the NaCMC powder in DI water using a magnetic stirrer (Tarsons Digital SPINOT) at 200-600 rpm subjected to the concentration of the NaCMC solution. We have prepared solutions (w/v) with 0.2 %, 0.25 %, 0.3 %, 0.35 %, 0.4 % and 0.45 % NaCMC salt concentrations (cf. top right side of Fig. 4.1). Here, 1% w/v indicate 1 g NaCMC salt in 100 ml of DI water. Blood samples were collected from voluntary participants and stored in vacutainer tubes (K_2EDTA) at room temperature until analysis. All procedures were carried out with a prior approval from the Ethics Committee of Government Medical College (GMC), Jammu (Approval No. IEC/GMCJ/2022/1144; dated November 3, 2022). Prior to every experimental run, the samples were vigorously mixed to achieve a homogeneous suspension. We have prepared blood solutions (38.23 % and 24.75 %) at different hematocrit levels by mixing 0.9 % saline water in pure whole blood (48.5 %). To prevent

the cell hemolysis, the osmotic strength of 0.9 % saline water is isotonic with whole blood solution (2002). We used Schott LED light to illuminate the experimental set-up and Nikon Z50 mirrorless camera for capturing videos. Moreover, all the experiments have been repeated three times and the average of the readings have been taken for further calculations.

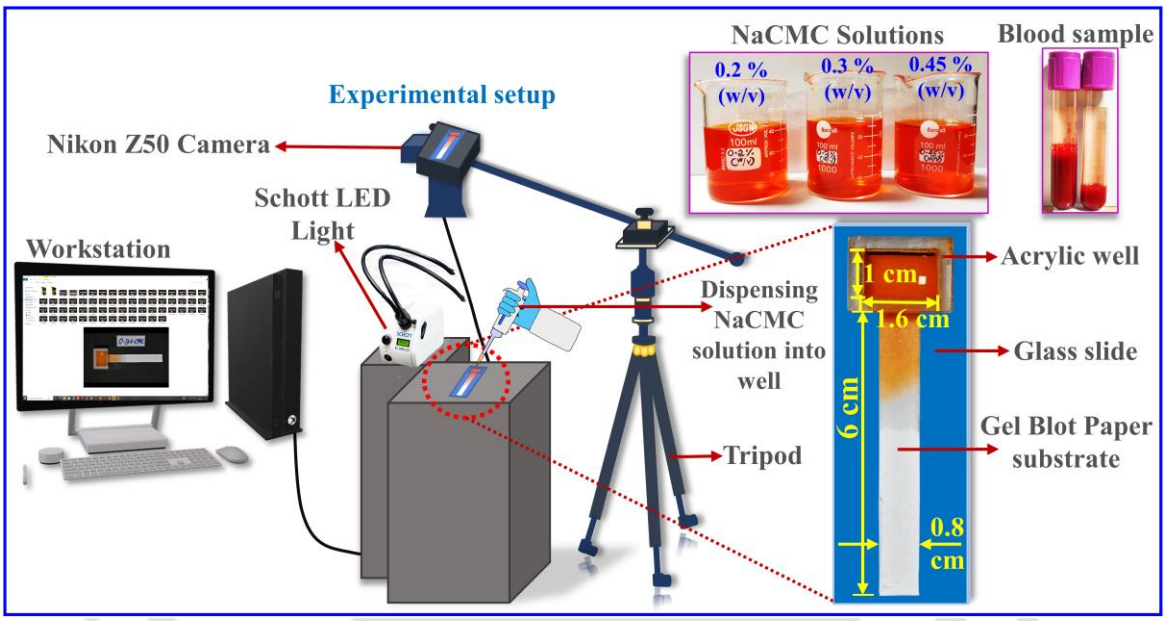

Figure 4.1. Schematic diagram of the experimental set-up depicting the wicking of non-Newtonian NaCMC solution and human blood in a gel blot paper strip placed on a glass slide with an acrylic well for filling the solution into it. Schott LED light is used to illuminated the test set-up and Nikon Z50 mirrorless camera mounted on a tripod is used to record videos of the wicking phenomenon. Three different concentrations of NaCMC solutions- 0.2 % (w/v), 0.3 % (w/v) and 0.45 % (w/v), mixed with 0.05 % (w/v) food dye and human blood samples of three different hematocrit levels are taken for the experiments. Note that food dye is used for easy visualization of the liquid wicking in the paper strip.

4.2.2. Viscosity measurement of non-Newtonian liquid

We considered NaCMC solutions with concentrations 0.2 % (w/v), 0.3 % (w/v) and 0.45 % (w/v); and human blood (hematocrit level: 48.5 %, 38.23 % and 24.75 %) for viscosity measurements using the Interfacial rheometer (Anton Paar, Model: MCR 301). We have measured the viscosity for the low shear rate range (10^{-3} and 10^{-1} s^{-1}), relevant to the underlying flow through paper-based fluidic pathways. The experimentally measured shear rate $(\dot{\gamma})$ versus viscosity (μ) data set has been fitted using the Carreau model and fitted as: $\mu = \mu_\infty + (\mu_o - \mu_\infty)(1 + (\lambda\dot{\gamma})^2)^{(n-1)/2}$. Here, μ_o, μ_∞, n and λ are the viscosity at zero and infinite share rate; flow behavior index and Carreau model time constant; and corresponding values of NaCMC solutions are presented in Table 4.1. and see Table 4.3. for blood.

4.2.3. Raman spectroscopy

The interaction between NaCMC solutions and the gel blot paper porous substrate has been examined using a laser-based Raman spectra analysis. For Raman analysis, we used the laser micro Raman system (HORIBA Jobin Vyon, Model LabRAM HR). The prepared NaCMC solutions with concentrations of 0.2% (w/v), 0.3% (w/v) and gel blot paper strips of dimensions 6 mm × 6 mm were taken for analysis. Initially, the dry gel blot paper was subjected to Raman spectroscopy. Subsequently, the gel blot paper was wetted with water, and subsequently with NaCMC solutions of 0.2% (w/v) and 0.3% (w/v) concentrations. Prior to spectroscopic measurements of the prepared samples using laser Raman equipment with 50× zooming lens, the gel blot paper substrate, wetted with NaCMC solution, is kept for 20 minutes to ensure it is in the same conditions as during the wicking experiments. The similar procedure has been included for the Raman spectral analysis of the blood.

TABLE 4.1. The fitting parameters of the Carreau model obtained from the experiment for low shear rate regime (10^{-3} to 10^{-1} s^{-1}) relevant for the paper-based flow.

	0.2 % (w/v)	0.3 % (w/v)	0.45 % (w/v)
μ_∞ in Pa-s	0.02319	0.241	0.6
μ_o in Pa-s	0.6841	0.973	2.621
n	0.3627	0.32	0.3
λ in s	68.91	65	64.8

4.3. MATHEMATICAL MODELING FOR EFFECTIVE VISCOSITY

The flow through the porous media is generally described by the Darcy-Brinkman–model (Ginzburg *et al.* 2015; Hu *et al.* 2016; Lyubimova *et al.* 2016; Strong *et al.* 2019). In this endeavor, we consider modified Darcy law for describing the imbibition phenomenon of non-Newtonian liquid through porous paper pathways, as elaborated later. It is noted that the modified Darcy law included assumptions such as a steady, laminar, single-phase, isotropic porous media with shear rate approximated by Darcy velocity. Furthermore, this model fails to account for inertia or pore-scale heterogeneity (Whitaker 1986). Also, the effective viscosity model treats the pore network model as equivalent capillaries and use bulk rheology as effective viscosity (μ_{eff}). This ignores local shear-rate variations, thixotropy, and multiphase effects (Sochi 2010b). For non-Newtonian fluid flow in porous media utilizing modified Darcy's law, an empirical constant, known as the effective viscosity ratio in this study, is required, as detailed in the upcoming paragraph.

To this end, we start with the description of Newtonian liquid imbibition in porous media, and corresponding momentum transport equation can be written as follows (Behera *et al.* 2023a; Gaikwad *et al.* 2017b):

$$\frac{\mu_N}{\phi}\frac{d^2U}{dy^2} - \frac{\mu_N}{K}U + -\left(\frac{dp}{dx}\right) = 0 \tag{4.1}$$

Where, the permeability of porous media, porosity, intrinsically averaged pressure, superficial velocity and liquid viscosity are represented by the symbols K, ϕ, p, U and μ_N, respectively. For complex fibrous porous media (paper) flow, K has been modelled using simpler representative unit cell (RUC) (Das *et al.* 2018; Maré and Woudberg 2023; Nabovati *et al.* 2009). Westhuizen and Plesssis (1996) implemented a mathematical model using a RUC of a bed of unidirectional fibres and obtained the transverse permeability as: $K = \frac{r_f^2\pi\phi\left(1-\sqrt{1-\phi}\right)^2}{24(1-\phi)^{1.5}}$. Based on the Darcy's law, Wada et al.(1985) first presented the modified Darcy law for non-Newtonian liquid flow in porous media. The experimental investigation by Comiti et al.(2000) suggests that the Darcy's law even valid for the non-Newtonian liquid up to the critical pore Reynolds number ~ 4.3. For the present case, the order of pore scale Reynolds number is obtained as ~ 10^{-7} - 10^{-6} for a liquid imbibition velocity in paper-strip ~10^{-5} m/s and viscosity ~ 10^{-1} - 1 Pa-s for NaCMC solution. In this context, it is noted that Brandao et al.(2021) provided the Darcy–Carreau–Yasuda rheological model for non-Newtonian fluid flow in porous media. They have defined effective apparent viscosity using the effective consistency index. Moreover, the viscosity of non-Newtonian liquid inside the complex pore is very difficult to estimate because of its strong dependency on shear rate, which in turn, depends on the flow field. Jang et al.(2025) demonstrated that the mobility factor of a non-Newtonian fluid in porous media, defined as the ratio of permeability to effective viscosity, analogous to the Newtonian liquid, as the ratio of permeability to constant viscosity. Motivated by this, we can write the modified Darcy's law for non-Newtonian liquid by introducing the effective viscosity as μ_{eff} in Eq. (4.1). Hence, the momentum transport equation for non-Newtonian fluid, consistent with the modified Darcy's law, can be written below:(Jang *et al.* 2025; WADA *et al.* 1985)

$$\frac{\mu_{eff}}{\phi}\frac{d^2U}{dy^2} - \frac{\mu_{eff}}{K}U + G = 0 \tag{4.2}$$

Here, $G = -dp/dx$. During wicking, the fluid encounters significant macroscopic viscous resistance relative to the equivalent porous free channel. This additional viscous resistance can be represented as effective viscosity (μ_{eff}) as the fluid passes through the porous

region. It is noted that Eq. (4.2) is important form of Darcy's law for non-Newtonian liquid, as the macroscopic axial velocity of wicking can be estimated from the experiments.

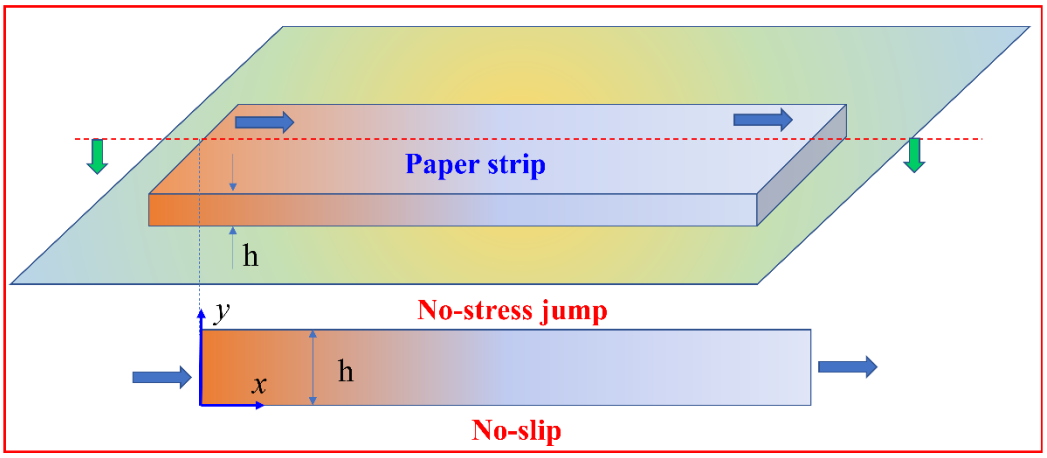

Figure 4.2. Schematic illustration of porous paper-strip and its projected cross-sectional domain taken for the analytical solution. Also, the boundary condition taken at the bottom and top part of the paper strip is mentioned.

We solve the ordinary differential equation (Eq. 4.2), and the general solution is given by the following expression:

$$U(y) = \frac{1}{\beta}\left[C_1 e^{\sqrt{\beta}y} + C_2 e^{-\sqrt{\beta}y} + \frac{G\phi}{\mu_{eff}}\right] \tag{4.3}$$

Where, $\beta = \phi/K$, and C_1, C_2 are arbitrary integration constants. Now, we employ the following boundary conditions to solve Eq. (4.3): at the bottom wall: $U(y)|_{y=0} = 0$, and at the top wall ($y = h$): no stress jump; $\mu_{eff}\frac{dU}{dy}\Big|_{y=h^+} = \mu_{eff}\frac{dU}{dy}\Big|_{y=h^-} \approx 0$. Here, h is the thickness of the paper strip (cf. to Fig. 4.2) and is taken as 0.8 mm. Hence, one-dimensional velocity profile can be obtained as:

$$U(y) = \frac{G\phi}{\mu_{eff}\beta}\left[A_1 e^{\sqrt{\beta}y} + A_2 e^{-\sqrt{\beta}y} - 1\right] \tag{4.4}$$

Where, $A_1 = \frac{e^{-\sqrt{\beta}h}}{e^{\sqrt{\beta}h}+e^{-\sqrt{\beta}h}}$, $A_2 = \frac{e^{\sqrt{\beta}h}}{e^{\sqrt{\beta}h}+e^{-\sqrt{\beta}h}}$ and h is the thickness of the porous strip. Accordingly, the average velocity of aqueous NaCMC solutions through the porous medium can be expressed as:

$$U_{avg} = \frac{\int_0^h U(y)dy}{\int_0^h dy} = \frac{G\phi}{\mu_{eff}\beta}\left[\frac{-(\sqrt{\beta}h)^2}{1+\sqrt{\beta}h+(\sqrt{\beta}h)^2}\right] \tag{4.5}$$

Now, using $G = -dp/dx$, we can get:

$$U_{avg} = \left(-\frac{dp}{dx}\right)\frac{\phi}{\mu_{eff}\beta}\left[\frac{(\sqrt{\beta}h)^2}{1+\sqrt{\beta}h+(\sqrt{\beta}h)^2}\right] \tag{4.6}$$

The pressure gradient, $-dp/dx$, can be expressed in finite representation as $\Delta p/\Delta x$. Here, Δp is the difference between the pressure at the liquid-air interface (i.e., capillary pressure, p_c) and entry pressure; and Δx is the axial distance of the imbibed liquid length from the strip entry. Also, one can write $\Delta p = p_f - p_i$; $p_f = p_c + p_{atm}$ and $p_i = p_{atm}$, hence, $\Delta p = p_c$. Therefore, from Eq. (4.6), we can write:

$$U_{avg} = \left(\frac{p_c}{x}\right)\frac{\phi}{\mu_{eff}\beta}\left[\frac{\left(\sqrt{\beta}h\right)^2}{1+\sqrt{\beta}h+\left(\sqrt{\beta}h\right)^2}\right] \tag{4.7}$$

In Eq. (4.7), the capillary pressure, p_c is estimated from the experiments and it is highly dependent on the liquid saturation-dependent (Abbasi and Andersen 2022; Mehta *et al.* 2025; Rath *et al.* 2018c; Verma and Toley 2024). The relationship between normalized liquid saturation and capillary pressure can be expressed as follows: using the Brooks and Corey correlation (Mehta *et al.* 2025):

$$p_c = p_{en}\overline{S_e}^{-\frac{1}{\lambda_b}} \tag{4.8}$$

Here, p_{en} and λ_b are the Brooks and Corey model parameters known as entry pressure required to move the liquid phase by displacing the air inside the pores and pore heterogeneity index, respectively. Further, the level of liquid saturation ($\overline{S_e}$) can be approximately related to the wicking length that wetted the paper strip (x). For the 0.06 m paper-strip length, the fractional level of liquid saturation can be approximated as $\overline{S_e} \sim x/0.06$. Hence, Eq. (4.8) and be approximately written as $p_c \sim p_{en}(x/0.06)^{-1/\lambda_b}$. Therefore, the corresponding expression for μ_{eff} can be written using Eq. (4.7) and given as:

$$\mu_{eff} \approx \left(\frac{p_{en}\left(\frac{x}{0.06}\right)^{-\frac{1}{\lambda_b}}}{x}\right)\frac{\phi}{U_{avg}\beta}\left[\frac{\left(\sqrt{\beta}h\right)^2}{1+\sqrt{\beta}h+\left(\sqrt{\beta}h\right)^2}\right] \tag{4.9}$$

In this endeavor, we considered Eq. (4.9) to estimate the effective viscosity of porous media, used for the analysis of non-Newtonian liquid imbibition, by estimating the wicking length (x) and interface velocity $\left(U_{avg}\right)$.

4.4. NUMERICAL MODELLING FOR SATURATION BASED POROUS MEDIA FLOW

In porous media, for the ith phase (wetting (w) and non-wetting (n)), the mass conservation equation is expressed as:

$$\frac{\partial\left(\phi\rho_{s_{e_i}}\right)}{\partial t} + \nabla\cdot\left(\rho_{s_{e_i}}\boldsymbol{u}_i\right) = 0 \tag{4.10}$$

Where the volumetric flow per unit width is: $\boldsymbol{u}_i = -\left(\frac{k_{rs_{ei}}}{\mu_{s_{ei}}}\right) k_{eq} \nabla p_{s_{ei}}$; moreover, for saturation level, s_{e_i}; k_{eq}, $k_{rs_{ei}}$, $\mu_{s_{ei}}$ and $p_{s_{ei}}$ are the equivalent permeability of the porous medium, permeability ratio, dynamic viscosity and pressure field, respectively. In the case of 100% saturation, the permeability ratio between the wetting and non-wetting phases is written as: $k_{rs_{e_w}} = \overline{S_e}^{\left(3+\frac{2}{\lambda_b}\right)}$ and $k_{rs_{e_n}} = \left(1-\overline{S_e}\right)^2 \left(1-\left(1-\overline{S_e}\right)^{\left(1+\frac{2}{\lambda_b}\right)}\right)$, respectively. Here, $\overline{S_e}$ is the normalized saturation level of the wetting phase. Furthermore, the following Brook and Corey correlation is an expression for the relationship between capillary pressure and normalized saturation ($\overline{S_e}$) (Hassler and Brunner 1945; van Genuchten 1980):

$$p_c = p_{en} \overline{S_e}^{-\frac{1}{\lambda_b}} \tag{4.11}$$

Where, the Brook and Corey model parameters are p_{en} and λ_b, termed as entry pressure when the fluid enters the porous medium displacing the air in the pores and the degree of heterogeneity, respectively.

The continuity equation can be written using the Darcy's law as described below (Hassler and Brunner 1945; van Genuchten 1980):

$$\frac{\partial(\phi\bar{\rho})}{\partial t} + \nabla \cdot (\rho \bar{\boldsymbol{u}}) = 0 \tag{4.12}$$

From Darcy's law, we have $\overline{\boldsymbol{u}} = \left(\frac{k_{eq}}{\bar{\mu}}\right) \nabla p$. Also, the averaged density is expressed as $\bar{\rho} = \sum_i s_{e_i} \rho_i$, and dynamic viscosity is written as $\bar{\mu} = \frac{\bar{\rho}}{\sum_i s_{e_i} \left(\frac{\rho_i}{\mu_i}\right)}$. The density of wetting (NaCMC solution) and non-wetting (air) fluid is taken as 1000 kg/m^3 and 1.2 kg/m^3 respectively. The viscosity of the non-wetting fluid is taken as 1.76 × 10^{-5} Pa-s. Moreover, the viscosity of the wetting fluid is taken as the effective viscosity of NaCMC solution in porous media using the curve fitted data of Fig. 4.5(a).

To numerically solve transport equations [Eqs. (4.10) and (4.11)] in a rectangular, two-dimensional paper-strip computational domain with length as 6 cm and width as 0.8 cm, we employ the following set of boundary conditions as given here. At the inlet: $\boldsymbol{n} \cdot \left(\rho_{s_{e_i}} \boldsymbol{u}_i\right) = 0$, $p_g = 0$; At the top and bottom edges: $\boldsymbol{n} \cdot \left(\rho_{s_{e_i}} \boldsymbol{u}_i\right) = 0$ and $\boldsymbol{n} \cdot (\rho \bar{\boldsymbol{u}}) = 0$; where, **n** is the normal from the wall surface. At the outlet: using Darcy's equation, ensuring capillary pressure equal to zero corresponding to fully saturated paper, we impose $p = -p_c \prod(\overline{S_e})$; here, $\prod(\overline{S_e})$ is smoothed step function. This step function $\prod(\overline{S_e})$ is equal to 1 when $\overline{S_e}$ varies between 0 to 0.9, and smoothly (i.e., without losing differentiability)

reaches $\prod(\overline{S_e})$= 0 with change in $\overline{S_e}$ from 0.9 to 1. Notably, this approximation is ought to serve as a boundary condition for Eq. (4.12). Therefore, weak constraints have been used to determine the precise flux at that border. Also, the Lagrangian multiplayer (LM_p, unit: $\mathrm{kg/(m\text{-}s)}$) for the shape functions of pressure in Eq. (4.10) is used at the outlet to calculate the accurate mass flux ($\mathrm{kg/(m^2\text{-}s)}$) therein. Hence, we have $-\boldsymbol{n}\cdot\left(\rho_{s_{e_i}}\boldsymbol{u}_i\right)=\frac{LM_p}{h}$, where, h is the thickness of the paper and taken as 0.8 mm. When weak constraints are used, it is observed that LM_p behaves as a new variable. Moreover, Verma and Toley (Verma and Toley 2024) emphasized that, in certain situations, implementing a "no-flux" inlet boundary condition may be physically incompatible. To resolve this, we have implemented an initial pressure condition derived from the mean capillary pressure at the experimentally determined saturation levels, which in accordance with the alternative methodology proposed by Verma and Toley (Verma and Toley 2024).

4.5. RESULTS AND DISCUSSION

We systematically discuss, in this section, the liquid saturation-dependent model parameters, the chemical analysis of paper in NaCMC liquid via Raman spectroscopy, effective viscosity in porous media, wicking length, wicking velocity, diffusive Peclet number, theoretical and actual trapping efficiency, trapping probability, and the estimation of critical axial design for the test line by modifying the rheological properties of the base liquid through variations in NaCMC solution concentration.

4.5.1. Saturation dependent capillary pressure of non-Newtonian liquid

In Fig. 4.3(a), we show the variation of capillary pressure obtained from the centrifugal experiment as a function of the NaCMC concentration. It has been observed that as NaCMC concentration increases, so does the magnitude of the capillary pressure. It is attributable to the increased bulk viscosity of NaCMC solution at higher concentrations, which causes strong centrifugal force to remove liquid from the pore to achieve desired liquid saturation level in the paper strip. Furthermore, the Brooks-Corey model expresses the capillary pressure of paper-based porous media in terms of the liquid entry pressure (p_{en}) and the degree of heterogeneity of the porous media (λ_b). According to the Brooks-Corey model, the capillary pressure is specified using the following relation as: $p_c = p_{en}(\overline{Se})^{\frac{-1}{\lambda_b}}$. Based on this model, we estimated the NaCMC concentration-dependent model

parameters (p_{en}, λ_b), as shown graphically in Figs. 4.3(b) and (c). The estimated data are presented in Table 4.2. The corresponding values of Brooks and Corey parameter for blood are presented in Table 4.3. We find that as NaCMC concentration increased, correspondingly increased the value of p_{en}.

TABLE 4.2. Estimation of Brooks and Corey model parameters at different NaCMC concentrations obtained from the saturation dependent capillary pressure curve.

C_{NaCMC} in % (w/v)	p_{en} (Pa)	λ_b
0.2	1.039×10^4	0.2606
0.25	2.444×10^4	0.2564
0.3	2.641×10^4	0.2469
0.35	3.028×10^4	0.2409
0.4	3.793×10^4	0.2341
0.45	4.962×10^4	0.2222

TABLE 4.3. Estimation of Brooks and Corey model parameters for blood at different hematocrit levels.

C_{NaCMC} in % (w/v)	p_{en} (Pa)	λ_b
48.5	1.60394×10^4	0.255768
38.23	1.039×10^4	0.2606
24.75	1.039×10^4	0.2606

The viscous liquid at higher NaCMC concentrations requires a higher entry pressure to displace air from the pore while entering the NaCMC solution. It is because of this reason, we find that with increasing the concentration of NaCMC, the liquid entry pressure (p_{en}) increases. In addition, the value of λ_b decreases as the NaCMC concentration increases in Fig. 4.3(b). It should be mentioned that λ_b is the pore size distribution index, which measures the degree of heterogeneity of porous media with wetted liquid. The decrease in pore size distribution index shows a larger degree of heterogeneity in porous media. The interaction of denser CMC-chains at higher concentrations is observed to give

rise to increased flow heterogeneity at the pore level. Consequently, when the concentration of NaCMC rises, the value of λ_b decreases.

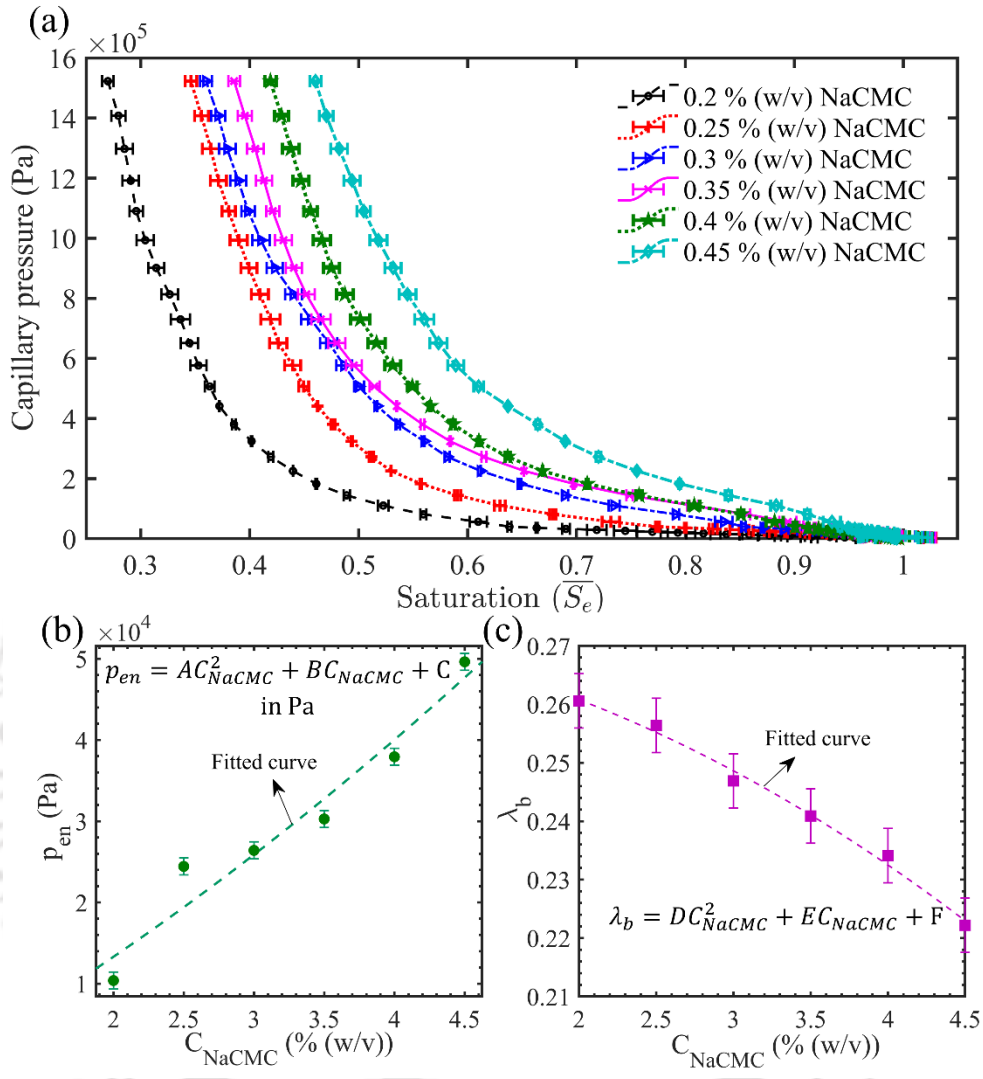

Figure 4.3. (a) Variation of liquid normalized saturation $(\overline{S_e})$ dependent capillary pressure obtained from centrifugal experiments by varying the NaCMC concentration (C_{NaCMC}). The variation of (b) entry pressure (p_{en}) and (c) degree of heterogeneity (λ_b) in the porous gel blot paper strip with respect to various concentrations of NaCMC $(C_{NaCMC})$is shown. The experimental fit expression for entry pressure (p_{en}) and degree of heterogeneity (λ_b) is obtained as: $p_{en} = AC_{NaCMC}^2 + BC_{NaCMC} + C$ in Pa with $R^2 = 0.97$and $\lambda_b = DC_{NaCMC}^2 + EC_{NaCMC} + F$ with $R^2 = 0.99$. Here, $A = 780$, $B = 8672$, $C = -7147$, $D = -0.001979$, $E = -0.002276$ and $F = 0.2733$. C_{NaCMC} is in % w/v (0.1 % w/v = 1 mg/mL).

4.5.2. Raman peak analysis

The cellulose chains are present in both NaCMC and gel blot paper. Cellulose has great affinity towards hydroxyl ions of water (Chami Khazraji and Robert 2013a), and able to form both the intramolecular and intermolecular hydrogen bond (Chami Khazraji and

Robert 2013b). It is previously reported that the stable hydrogen bonds in cellulose lead to the stable structure of it (Long *et al.* 2024; Wei *et al.* 2024). Hence, we have presented in Fig. 4.4 the Raman intensity curve of hydroxyl group band (3390 cm^{-1} to 3590 cm^{-1}) (Lota *et al.* 2016; Środek and Dulski 2025) for dry gel blot paper, wetted gel blot paper with DI water and at different values of NaCMC concentration. We can see that an increase in cellulose content with the increase in NaCMC concentration leads to the increment in the corresponding peak value. Therefore, we can infer that the formation of greater number of stronger hydrogen bond in cellulose is primarily because of the water at higher NaCMC concentration. The greater number of stable hydrogen bonding leads to excess flow resistance during wicking at the higher values of NaCMC concentration. This effect may lead to greater extent of effective viscosity argumentation at higher values of NaCMC concentration, as discussed in upcoming sub-section.

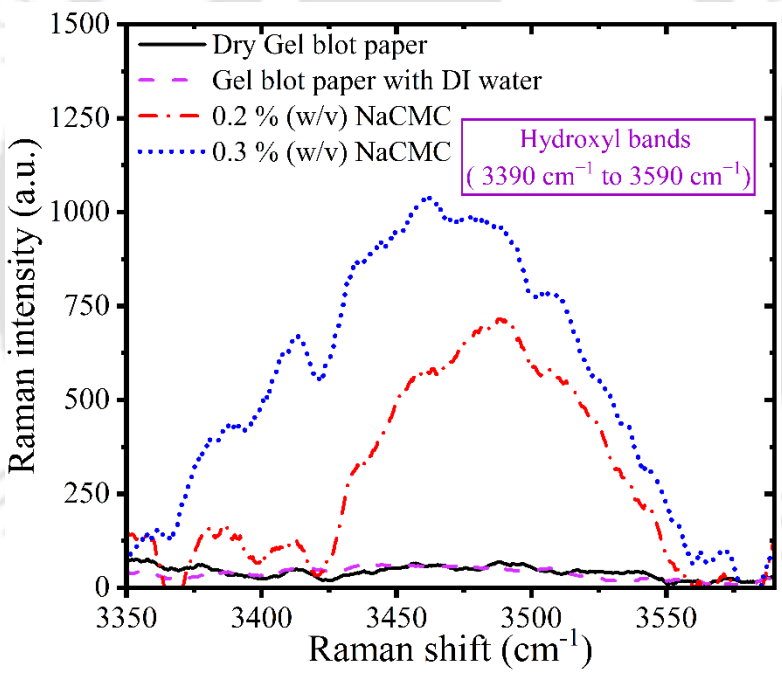

Figure 4.4. Raman shift intensity of hydroxyl band (3390 cm^{-1} to 3590 cm^{-1}) for dry gel blot paper, wetter gel blot paper with DI water and at different NaCMC concentrations.

4.5.3. Estimation of bulk effective viscosity of non-Newtonian liquid in paper-strip

We undertook an effort to analyze the temporal variation of effective viscosity (μ_{eff}) of the NaCMC solution in gel blot paper utilizing Eq. (4.9), as depicted in Fig. 4.5(a). We can see that the effective viscosity increases by the order of magnitude as the NaCMC concentration increases. This is due to the increased number of stable hydrogen bonds

resulting from a greater number of hydroxyl groups at higher NaCMC concentrations, as illustrated in Fig. 4.4. The significant increase in flow resistance caused by the higher-

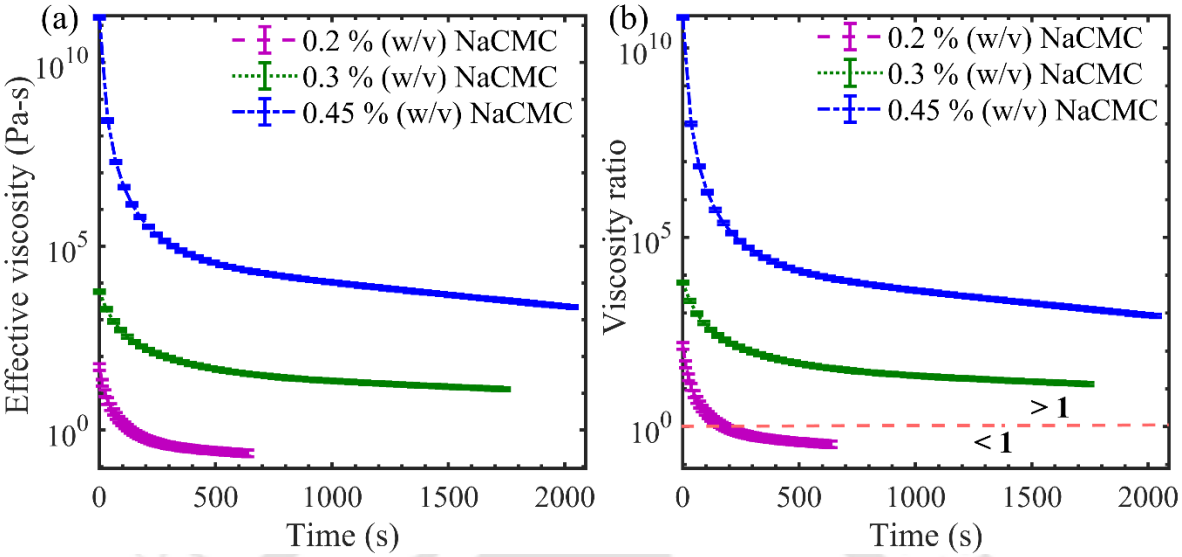

Figure 4.5. Temporal variation of (a) effective viscosity in Pa-s and (b) viscosity ratio for three different NaCMC aqueous solution concentrations- 0.2 % (w/v), 0.3 % (w/v) and 0.45 % (w/v).

-quantity of stable internal hydrogen bonds facilitates a proportional substantial rise in the effective viscosity of porous media as NaCMC concentration increases. Furthermore, we have assessed the effective viscosity ratio (μ_{eff}/μ) with respect to the viscosity of NaCMC solution measured by the rheometer through the temporal variation of (μ_{eff}/μ), demonstrated in Fig. 4.5(b). Note that the viscosity ratio is defined as the ratio of effective viscosity of the NaCMC solution to the rheometer viscosity. The rheometer viscosity (μ) is determined following to the Carreau model, utilizing the experimentally measured values provided in Table 4.1. The effective viscosity ratio is observed to be smaller than unity at lower concentrations of NaCMC solution, as illustrated in Fig. 4.5(b). This phenomenon can be ascribed to the reduced quantity of stable hydrogen bonds and the predominant shear-thinning characteristics of the NaCMC solution within the pores of the gel blot paper. This leads to a decrease in the effective viscosity of porous media relative to the rheometer viscosity of NaCMC solution at lower concentrations. This inference aligns with Breugem's results (Breugem 2007), which indicate that the pore configuration accounts for this phenomenon. This study predicted lower effective viscosity in porous media relative to the bulk solution when the porous structure is of the "channel" type. In the present study, the fibrous structure of the pore at lower NaCMC concentrations also provides a "channel" type pore configuration in addition to a lesser number of stable hydrogen bonds. Consequently,

the effective viscosity ratio is determined to be below unity at lower concentrations of NaCMC. Furthermore, the greater amount of stable hydrogen bonding results in a higher viscosity ratio (> 1) significantly exceeding unity at higher concentrations of NaCMC.

4.5.4. Wicking of non-Newtonian liquid

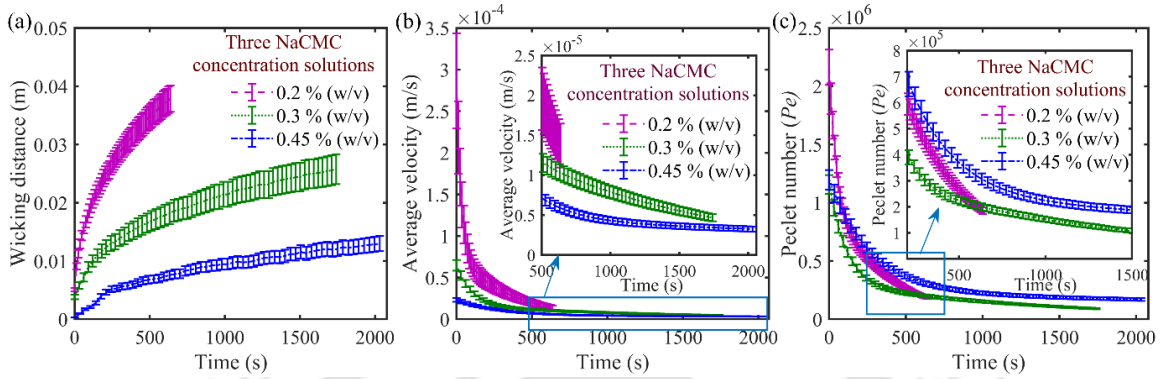

Figure 4.6. Temporal variation of (a) wicking distance in m, (b) average velocity (U_{avg}) in m/s and (c) food dye particle Peclet number (Pe) for three different NaCMC aqueous solution concentrations- 0.2 % (w/v), 0.3 % (w/v) and 0.45 % (w/v).

In Fig. 4.6(a), we show the temporal wicking length as a function of NaCMC concentration. The wicking length has been demonstrated to decrease with an increase in NaCMC concentration. The higher viscosity of the NaCMC solution at greater concentrations allows it to substantially resist the driving capillary force in the paper strip. As a result, we find a decrease in average wicking velocity (U_{avg}) with increasing CMC concentration, as shown in Fig. 4.6(b). Analyte transport in paper-strip is, therefore, significantly impacted by the variations in NaCMC viscosity that occur with changes in its concentration. The viscosity of the base fluid has a significant impact on the analyte's diffusion coefficient. Note that we have considered food dye particles as analytes in this analysis. As shown in Fig. 4.6(c), the variation in analyte diffusive Peclet number is strongly controlled by NaCMC concentration. The diffusive Peclet number for food-dye particle is expressed as $Pe = U_{avg}D_g/D$; where, $D\left(= K_BT/3\pi\mu d_p\right)$, $D_g(= 10.37\mu m)$, U_{avg} and $d_{pt}(= 0.848\mu m)$ are the diffusion coefficient, pore grain diameter, average velocity in paper strip and particle diameter, respectively. The dominance of the declining trend of the average flow velocity (cf. Fig. 4.6(b)) with an increase in NaCMC concentration from 0.2 to 0.3% (w/v) lowers the diffusive Peclet number. On the other hand, the dominance of the reduction in diffusion owing to the higher viscosity of the background solution at higher concentration of NaCMC leads to an increase in diffusive

Peclet number when concentration varies from 0.3 to 0.45% (w/v). We can therefore infer that the background fluid rheology has a significant role to play on the analyte transport.

4.5.5. Comparison of numerical findings with experimental results

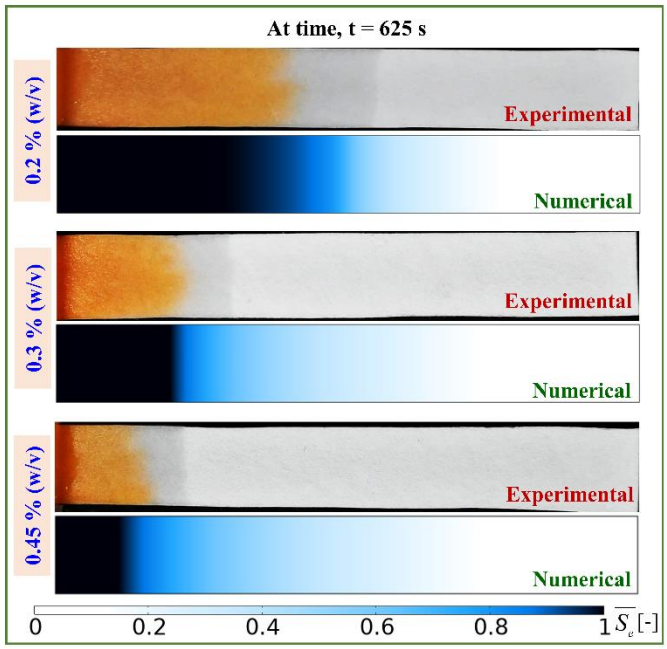

Figure 4.7. Comparison of liquid saturation level contours obtained from experiments and numerical simulations at time, t = 625 s for three different values of NaCMC aqueous solution concentrations- 0.2 % (w/v), 0.3 % (w/v) and 0.45 % (w/v).

In Fig. 4.7, we depict and compare the wicking of aqueous solution of NaCMC obtained from simulations and experiments at different concentrations at time t = 625 s. The paper-based porous media flow is modelled using the saturation-dependent phase transport model. We find a fairly accurate match of liquid saturation level between numerical and experimental results, as demonstrated in Fig. 4.7, primarily attribute to the use of effective viscosity of porous media in the numerical framework. Furthermore, at a particular temporal instant, with increasing the concentration of NaCMC in the liquid sample, the saturation level reduces as witnessed in Fig. 4.7. We attribute this observation to a greater flow resistance rendered by an increase in effective viscosity (see Fig. 4.5(a)).

4.5.6. Analyte trapping analysis

There are three primary mechanisms, as discussed in the referred literature (Nelson and Ginn 2005; Payen *et al.* 2012; Wang and Otani 2013; Wang *et al.* 2012b), are responsible for trapping the analyte particles inside the porous media. Firstly, the diffusion dominated trapping associated with the stochastic thermal motion of particles facilitates

their entrapment on the pore surface. Trapping efficiency by diffusion, also called as the Brownian trapping efficiency (η_B), can be calculated following the relation given below:(Nelson and Ginn 2005; Payen *et al.* 2012; Wang and Otani 2013; Wang *et al.* 2012b)

$$\eta_B = 4A^{\frac{1}{3}}Pe^{\frac{-2}{3}} \tag{4.13}$$

Here, $A = \frac{2(1-\Upsilon^5)}{2-3\Upsilon+3\Upsilon^5-2\Upsilon^6}$, $\Upsilon = (1-\phi)^{\frac{1}{3}}$. The diffusive Peclet number for particle transport is expressed as $Pe = \frac{U_{avg}d_p}{D}$.

Interception trapping mechanism is the second to describe the particle trapping which occurs primarily due to the size disparity between the particle and the porous fibre. At the upstream of the pore, the interception mechanism creates a capture zone. The expression for interception trapping efficiency is written as follows:(Nelson and Ginn 2005; Payen *et al.* 2012; Wang and Otani 2013; Wang *et al.* 2012b)

$$\eta_I = 1.5AN_R^2 \tag{4.14}$$

Where, the ratio of particle diameter to the pore size is represented as $N_R\left(= d_{pt}/d_p\right)$.

Subsequently, inertial trapping efficiency (η_{IN}), accounts for the trapping due to the inertial impact. Typically, for the higher Stokes number (St), the particles close to the pore wall deviate from the streamlines, maintaining their initial trajectory until they collide with the pore wall. The mathematical expression for inertial trapping efficiency (η_{IN}) can be written as follows:(Nelson and Ginn 2005; Payen *et al.* 2012; Wang and Otani 2013; Wang *et al.* 2012b)

$$\eta_{IN} = \frac{St^3}{St^3+0.77St^2+0.22} \tag{4.15}$$

where the Stokes number (St) is expressed as $St = \frac{(\rho_p d_{pt}^2 u_{avg})}{(18\mu d_p)}$.

With all of these well-reported trapping efficiency components considered, the overall theoretical trapping efficiency (η_o) can be expressed as follows:(Mehta *et al.* 2025)

$$\eta_o = \eta_B + \eta_I + \eta_{IN}. \tag{4.16}$$

Moreover, by estimating the normalized concentration of food dye $\left(\frac{C}{C_O}\right)$ (C_O = initial concentration), the actual trapping efficiency can be written as follows:(Mehta *et al.* 2025)

$$\eta = \frac{-ln\left(\frac{C}{C_O}\right)}{\left(1.5\left(\frac{1-\phi}{\phi}\right)\frac{x}{d_p}\right)} \tag{4.17}$$

Hence, the trapping probability (α) can be mathematically written as follows based on the theoretical and actual trapping efficiency:(Mehta *et al.* 2025)

$$\alpha = \frac{\eta}{\eta_o} \tag{4.18}$$

Pertaining to this analysis, as the order of Stokes number (~ 10^{-12} to 10^{-9}) is very low (<< 1), it is seen that the order of inertial efficiency (~ 10^{-33} to ~10^{-25}) is also quite small. Consequently, it has no significant effect on overall efficiency as witnessed in Fig. 4.8(a). It is determined that the interception efficiency is 0.0554. Furthermore, the diffusion-based trapping efficiency has been calculated to be in the order of ~10^{-3}. As can be seen from Fig. 4.8(a), the overall efficiency is mainly reliant on the diffusion efficiency because the interception efficiency is constant for the specified pore size and analyte particle size. Therefore, we have presented the variation of diffusion trapping efficiency in Fig. 4.8(b). As apparent from Eq. (4.13), the diffusion trapping efficiency is inversely related to the diffusive Peclet number. Thus, the variation in diffusion trapping efficiency is inversely related to the change in diffusive Peclet number (Fig. 4.6(c)) as time and NaCMC concentration changes. Therefore, as time and NaCMC concentration changes, the overall trapping efficiency follows the same pattern because of the dominating diffusion-based trapping efficiency for the present study.

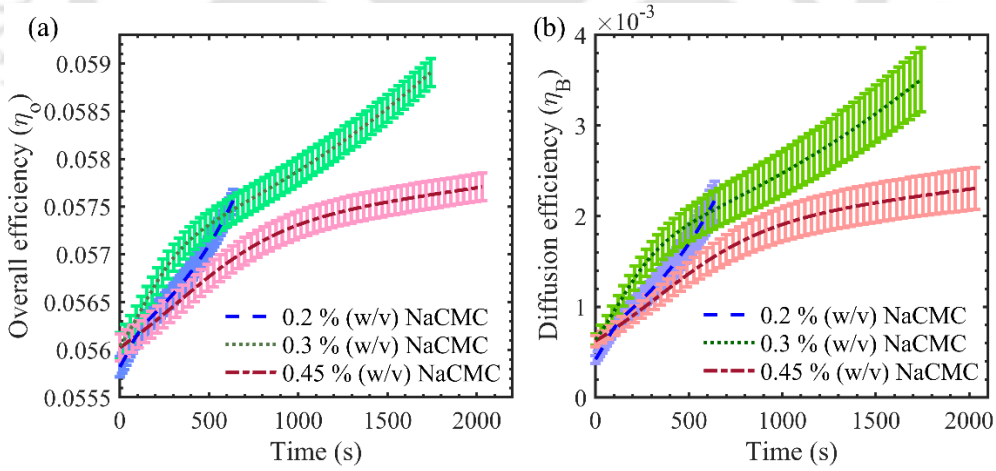

Figure 4.8. Temporal variation of (a) overall efficiency (η_o) and (b) diffusion efficiency (η_B) for three different NaCMC aqueous solution concentrations- 0.2 % (w/v), 0.3 % (w/v) and 0.45 % (w/v).

It is evident in Eqs. (4.17) and (4.18) that the trapping efficiency of analytes depends on to their normalized concentration. We have illustrated the normalized analyte concentration in a paper strip at t = 625 s in Fig. 4.9. We found that when axial length increases, the normalized concentration decreases and it mainly due to the analyte trapping in the downstream section of the paper pathway. Due to the reduced wicking length at larger

NaCMC concentrations (cf. Fig. 4.6(a)), the normalized concentration reaches zero at early axial section of the paper strip.

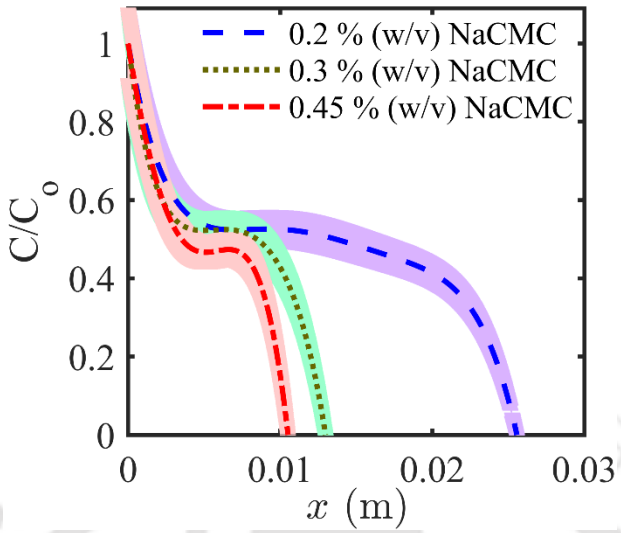

Figure 4.9. Variation of normalized concentration $\left(\frac{C}{C_o}\right)$ in axial direction for three different NaCMC aqueous solution concentrations- 0.2 % (w/v), 0.3 % (w/v) and 0.45 % (w/v).

We show the variation of actual trapping efficiency of food dye particle in Fig. 4.10(a), obtained for different concentrations of NaCMC. We find that the trapping probability of food dye particle is remaining nearly unchanged with change in NaCMC concentration at inlet side location ($x \rightarrow 0$). This observation is mainly because of the nearly equal normalized concentration profile for all NaCMC concentrations at smaller axial location ($x \rightarrow 0$), as witnessed from Fig. 4.9. Whereas, the greater difference in normalized analyte concentration with change in NaCMC concentration (see Fig. 4.9) at greater axial length leads to NaCMC-concentration dependent actual efficiency curve. As the actual efficiency is directly related to $-ln\left(\frac{C}{C_o}\right)$, a decrease in normalized concentration (< 1) leads to an increase in actual trapping efficiency with an increase in NaCMC concentration at larger axial length. Furthermore, as shown in Eq. (4.18), the trapping probability is directly related to the actual trapping efficiency. Therefore, the variation in trapping probability (refer to Fig. 4.10(b)) is identical to the change in actual trapping efficiency. Consequently, we obtain a very high food dye trapping probability at higher NaCMC concentrations at greater axial locations, as shown in Fig. 4.10(b).

4.5.7. Analysis of reaction zone axial length based on the critical Damköhler number

The axial position of the test line should be optimized depending on the effective reaction rate of analytes in order to develop lateral flow assays (LFAs) with high precision.

To delve deep into this part, we appeal to the Damköhler number (Da), which is a dimensionless number and defined as the ratio of the characteristic reaction rate to the convective transport rate. The mathematical expression for Damköhler number is $Da = C_M k_a/(U_{avg}/l_t)$, Where C_M, k_a , and l_t are the analyte's molar concentration, forward reaction constant, and characteristic length scale for reaction, with 2 mm as the thickness of the reaction zone at the test line (Mehta *et al.* 2025). Moreover, the reaction rate constant approaches the order of ~10^6 $M^{-1}s^{-1}$ with analyte molar concentration in the order of ~10^{-6} to10^{-5} M (Nalumachu *et al.* 2023; Oh *et al.* 2014; Qian and Bau 2003). Therefore, the rate of reaction rate order is obtained as ~1 to 10 s^{-1}, which is relevant to lateral flow assay. Based on this analysis, we depict the contours of Damköhler number in the plane of the previously described reaction rate to the wicking length in Fig. 4.11. The contours are plotted by altering the concentration of NaCMC in the aqueous solution. The critical Damköhler number (Da_c) is set to 50 (>> 1) to ensure an effective reaction at the test line. Figure 4.11 shows the locus of (Da_c) together with the variation in reaction rate and wicking length. The wicking length corresponding to the locus point of Da_c determines the appropriate location of the test line, offering an effective reaction.

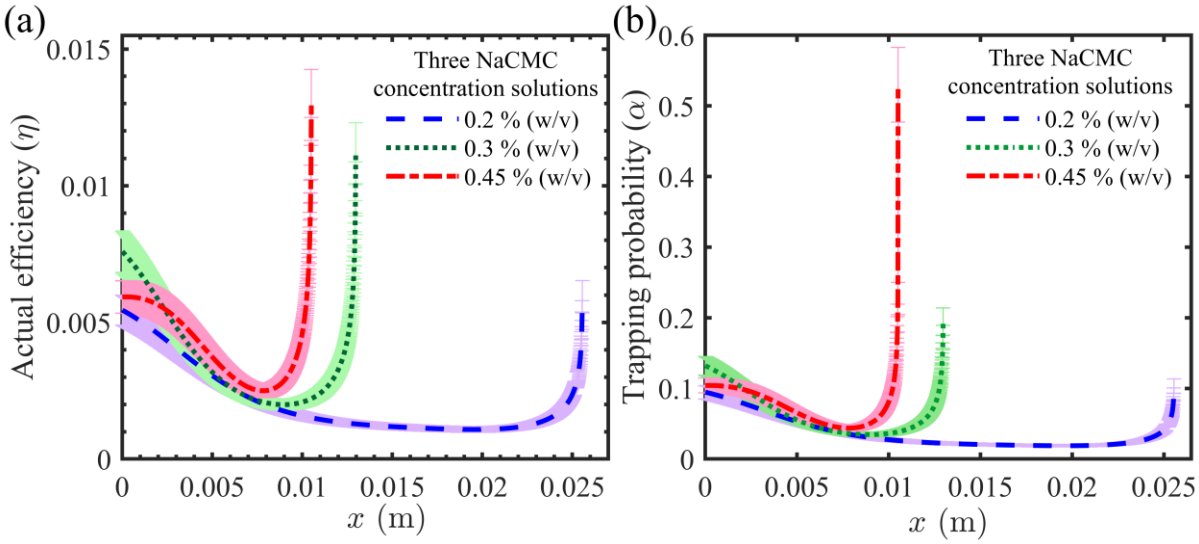

Figure 4.10. Variation of (a) actual efficiency (η) and (b) trapping probability (α) in axial direction for three different NaCMC aqueous solution concentrations- 0.2 % (w/v), 0.3 % (w/v) and 0.45 % (w/v).

We observe that increasing the concentration of NaCMC results in a reduction in the axial location of the appropriate test line. It corresponds to the decrease in averaged flow velocity [see Fig. 4.6(b)] at higher NaCMC concentrations, which leads to reduced convective flow strength in the paper strip. Consequently, the reduced convective strength

of the analytes in paper-strip leads to shorter axial locations with higher Da for a given reaction rate order. This discussion underlines that the design of an LFA test line is greatly affected by the rheology of working fluid.

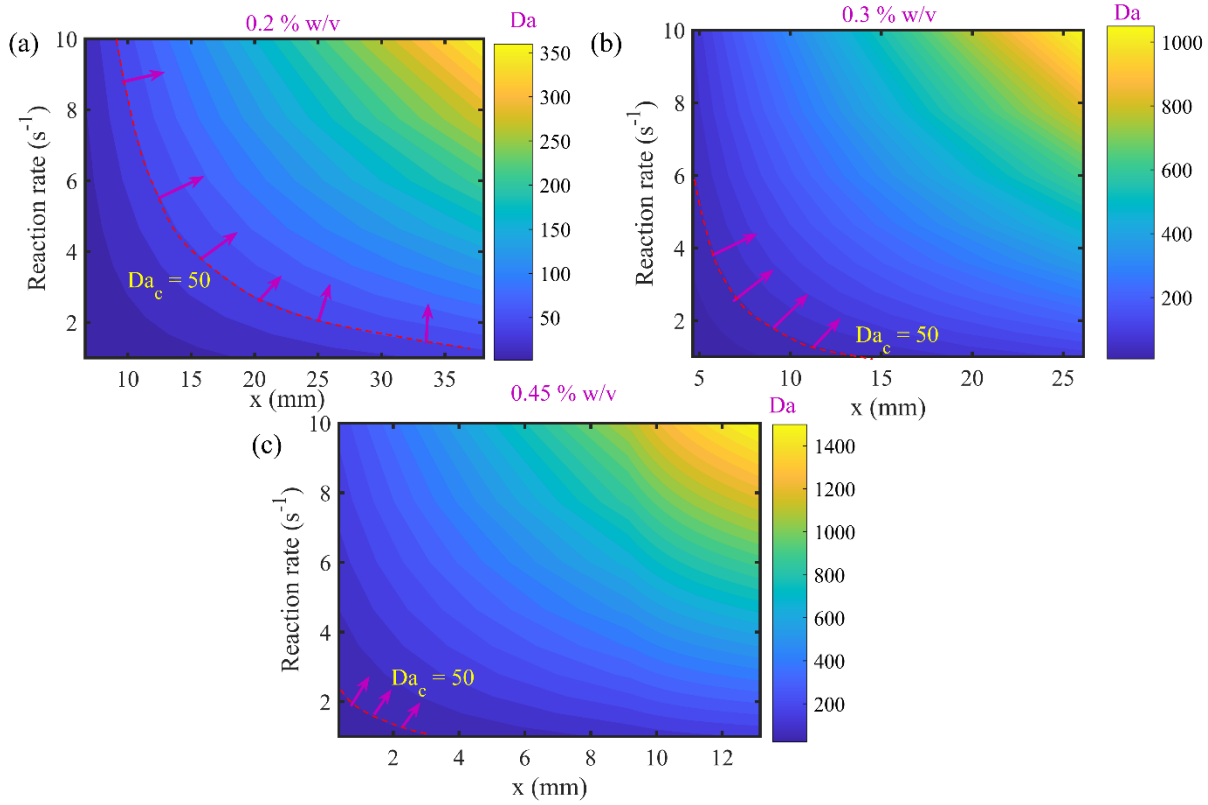

Figure 4.11. Contours of Damköhler number in the plane of reaction of relevant analytes used in LFA to the wicking length for (a) 0.2 % w/v, (b) 0.3 % w/v and (c) 0.45 % w/v for gel blotting paper.

4.5.8. Wicking of blood in paper strip

We have now used human blood as the working liquid in paper strip to examine the wicking phenomenon. As seen from Fig. 4.12(a), we have taken three types of blood solutions based on the haematocrit level. The hematocrit level of blood is estimated in Grade 1 filter paper using the established protocol by Ram et al.(2023) We can observe from Fig. 4.12(b) that the increase in hematocrit level leads to the reduction in wicking length. It is because of enhanced RBC content at the greater haematocrit level. Note that the higher haematocrit level leads to higher viscosity and restrict the wicking as well. Hence, as seen from Fig. 4.12(c), the average wicking length reduces with increase in haematocrit level. Moreover, the average wicking velocity of the blood solution is found to be strongly dependent on the haematocrit level, as seen from Fig. 4.12(d). The reduced viscosity at lower hematocrit level leads to higher average velocity for blood at the smaller

time instants. Whereas, for the greater time instants, the dominancy of viscous resistance leads to reduced average velocity for all types of blood solutions considered.

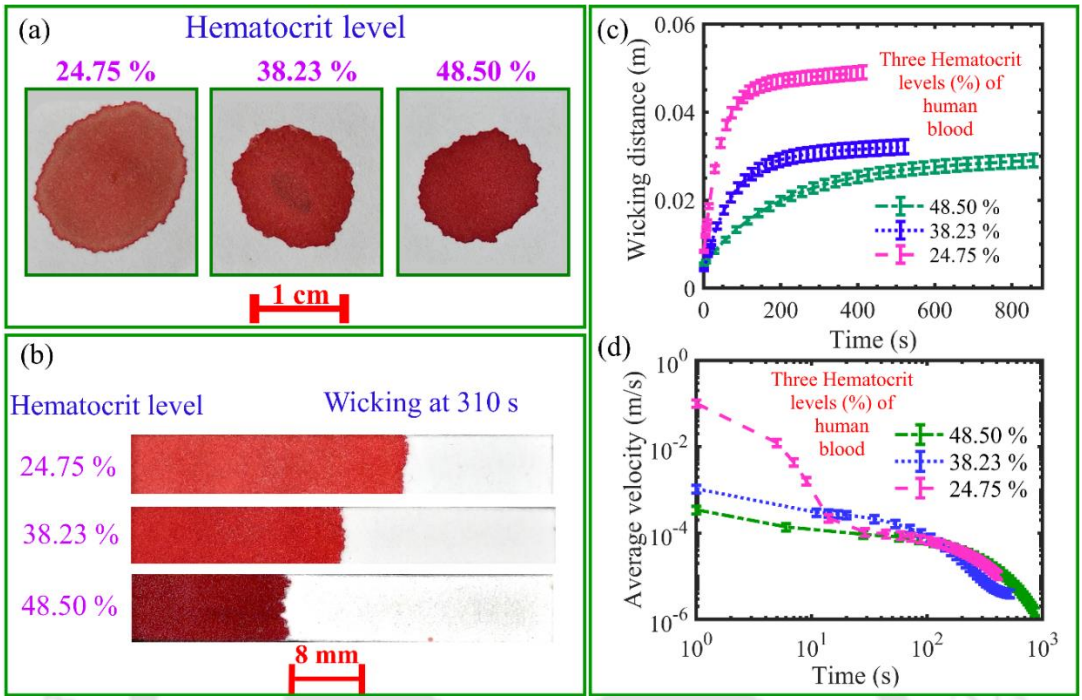

Figure 4.12. (a) Haematocrit level estimation in Grade 1 filter paper based on the protocol established by Ram et al.(Ram *et al.* 2023) (b) Wicking profile of blood at the different haematocrit level at 310 s after sample loading. Variation of (c) wicking distance and (d) average wicking velocity of the blood sample at different values of haematocrit level.

We have also estimated the effective viscosity of blood in gel blot paper by varying the hematocrit level as seen from the Fig 4.13(a). To estimate this effective viscosity, the value of p_{en} and λ_b for blood is presented in Table 4.3. We found that an increase in RBC content with rising hematocrit level results in greater effective viscosity, attributed primarily to the enhanced flow resistance caused by the interaction between the paper pores and the blood cells. Interestingly, the effective viscosity for blood sample is found to follow non-monotonic trend with increase in time interval during wicking phenomenon. We found that the effective viscosity shows a decreasing trend at lower time instants with increasing hematocrit level. This observation can be attributed to the dominancy of reduction in capillary pressure because of the increase in blood saturation level (see Eq. 4.8). Whereas, for the greater time instants, the decrease in saturation level is minuscule because of the lower wicking velocity (see Fig. 4.12 (d)). Hence, it can be inferred following Eq. (4.9) that, the effective viscosity of blood reduces with greater time instant because of the dominating effect of the decrease in average wicking velocity of blood (see Fig. 4.12(d)). Moreover, we have also presented the effective viscosity ratio (μ_{eff}/μ) for blood in Fig.

4.13(b) by varying the hematocrit level. The rheometer viscosity of blood (μ), is estimated experimentally and fitted with Carreau model. The Carreau model parameters, fitted for blood at lower shear rate (relevant for paper-based flow), are presented in Table. 4.4.

TABLE 4.4. The fitting parameters of the Carreau model obtained from the experiment for low shear rate regime (10^{-3} to 10^{-1} s^{-1}) relevant for the flow of blood in paper-based substrate.

	48.50 %	38.23 %	24.75 %
μ_∞ in Pa-s	0.1	0.015	0.01
μ_o in Pa-s	3.5	0.8	0.3
n	0.15	0.17	0.2
λ in s	34.52	30.09	30.15

We found that the viscosity ratio is found to be less than unity for the specific range of temporal instants for given hematocrit level of blood (see Fig. 4.13 (b)). This observation can be attributed to the shear-thinning nature of the blood, which allows reduction in effective viscosity in pores under shearing action compared to the rheometer viscosity of the blood. For lower time instants, the order of viscosity ratio is found to be much greater than unity. It can be explained by the initial trapping of RBCs in pores under high capillary pressure, which resists the blood imbibition. Also, at higher temporal instants, the increase in effective viscosity (see Fig 4.3(a)) leads to effective viscosity greater than unity. Hence, we can say that the effective viscosity of blood in paper pathways is highly dependent on the hematocrit level as well as its degree of saturation which alters the capillary pressure.

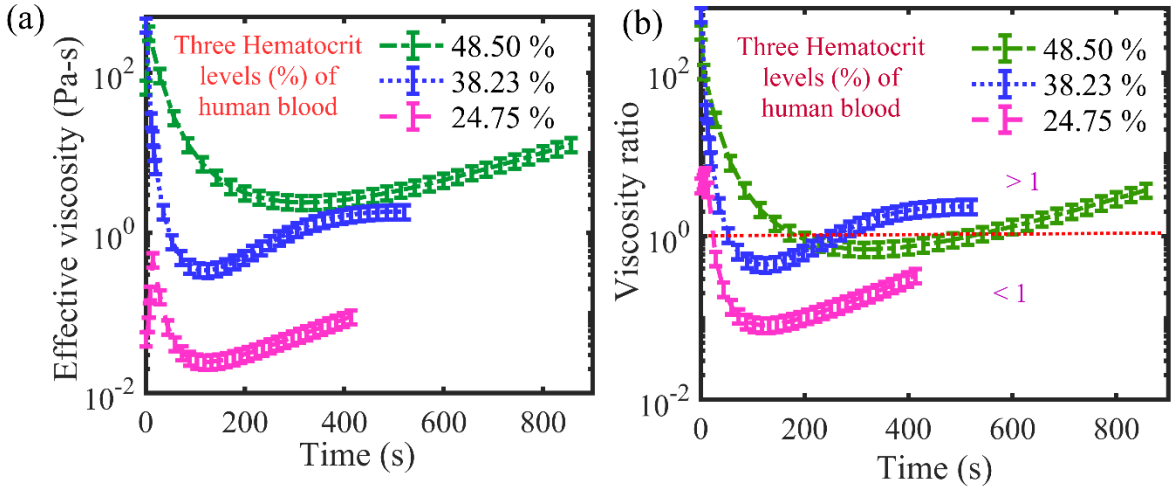

Figure 4.13. Variation of (a) effective viscosity and (b) viscosity ratio of the blood sample at different values of haematocrit level using gel blot paper.

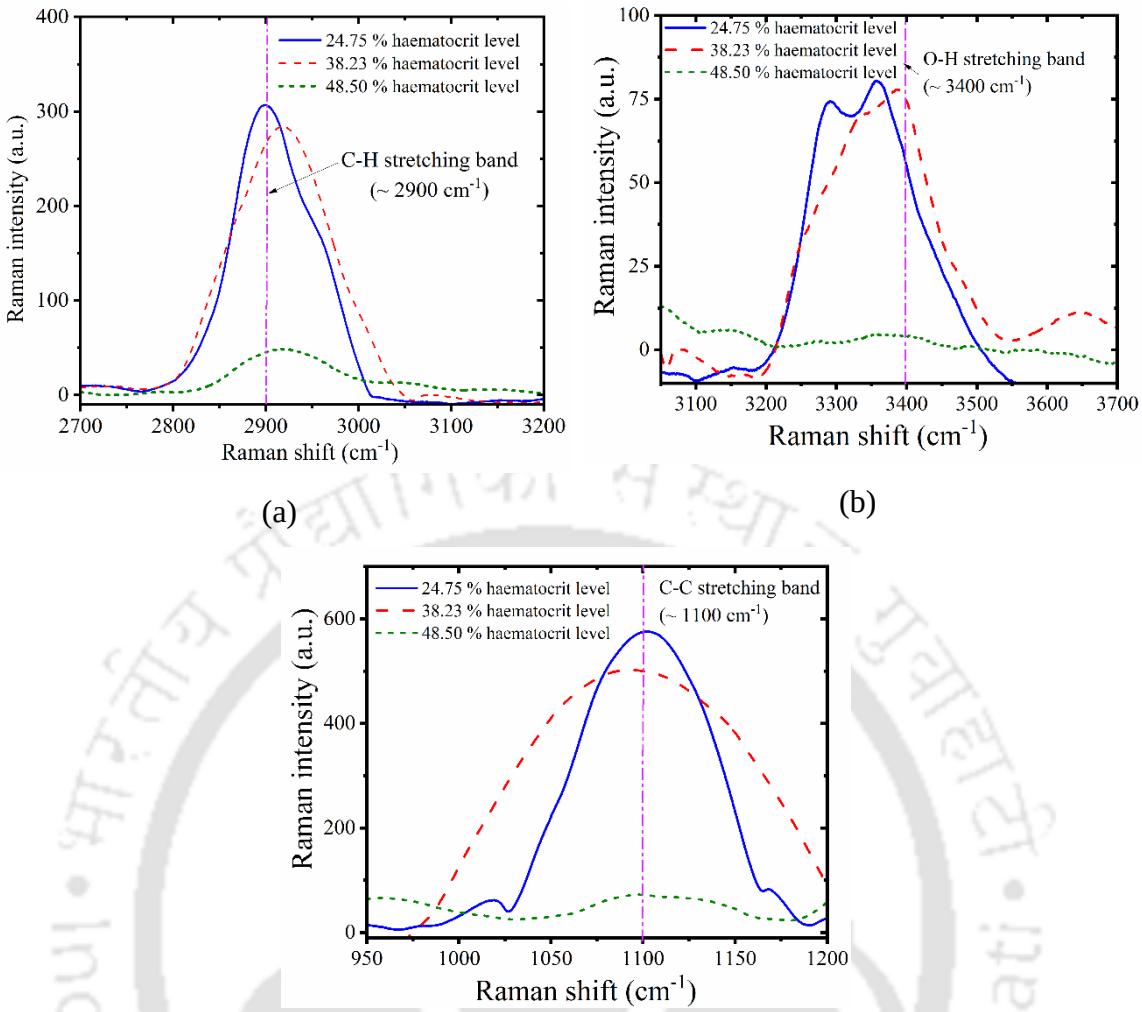

Figure 4.14. Variation of Raman intensity curve for (a) C-H stretching bond, (b) O-H stretching bond and (c) C-C stretching bond for blood sample at different values of haematocrit level using gel blotting paper.

To see that chemistry of blood inside the paper strip, the corresponding Raman intensity plot is depicted in Fig. 4.14. First, the Raman intensity related to C-H stretching bond (~ 2900 cm^{-1}) is presented in Fig. 4.14(a) for the different haematocrit levels, obtained using gel blotting paper. This peak can be related to the water in DNA solution (Uozumi and Takahashi 2023) and polymeric group of paper strip (Morita *et al.* 2007). Generally, red blood cells contain DNA (Liang *et al.* 2023), and the greater availability of water in blood at lower haematocrit levels allows for more interaction between water molecules, DNA, and cellulose, leading to a higher Raman intensity for the C–H stretching bond (~3400 cm^{-1}). Further, the Raman intensity of OH stretching bond (Makarem *et al.* 2019) is also evident for blood solution in paper strip as depicted in Fig. 4.14(b). This Raman peak is mainly attributed to the interaction of cellulose with the water molecule. The underlying interaction is responsible for producing the hydroxyl group and enhances the

peak intensity with the decrease in haematocrit level. Moreover, the significant intensity of C-C stretching bond (~1100 cm^{-1}) is also evident for the blood solution in paper strip, as witnessed in Fig. 4.14. This C-C stretching bond is typically indication of lipid and glucose in blood (Meier *et al.* 2006; Wang *et al.* 2010). At lower hematocrit levels, more water is available in the sample, and this affects the C-C bond stretching because of the higher number of hydrogen bonds in molecule, which enhances the Raman intensity of the C–C stretching bond.

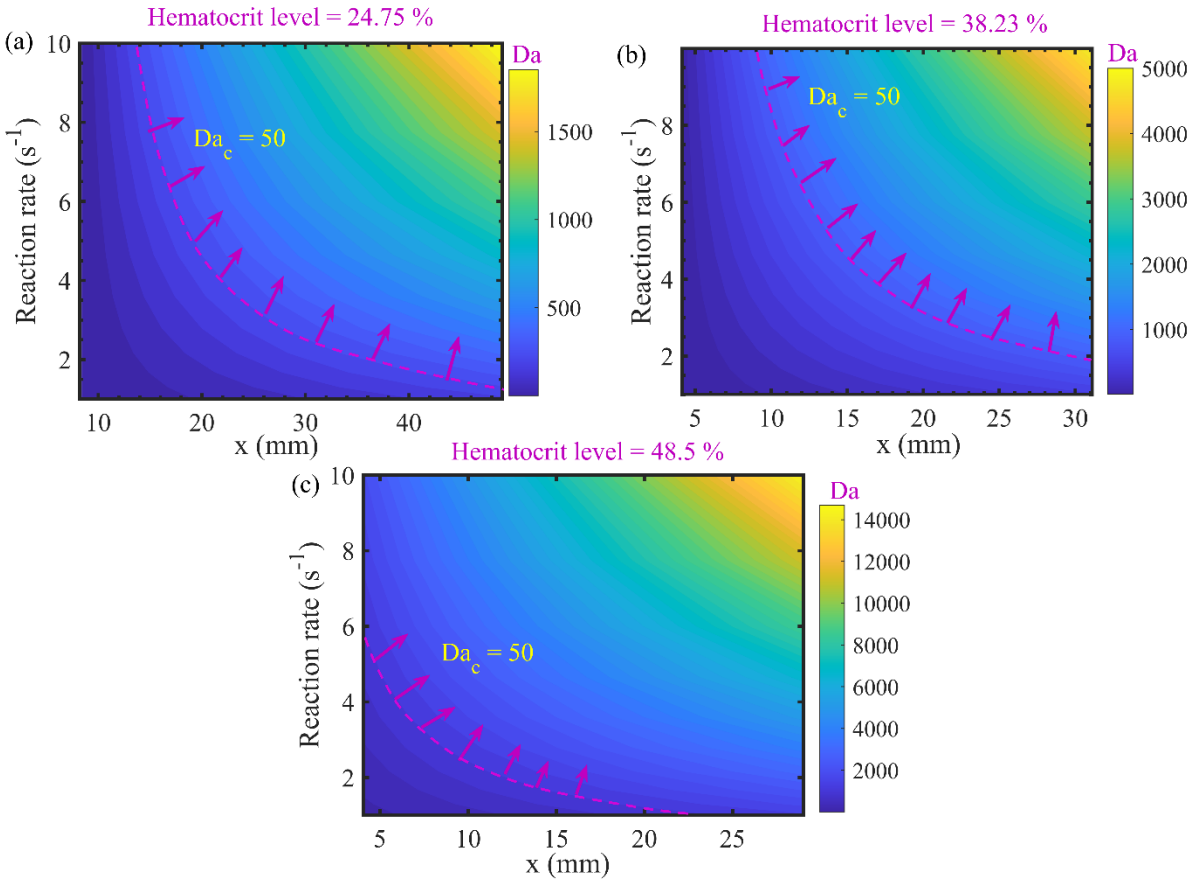

Figure 4.15. Contours of Damköhler number in the plane of reaction of relevant analytes in blood sample used in LFA to the wicking length for (a) 24.75 %, (b) 38.23 % and (c) 48.5 % of haematocrit level using gel blotting paper.

To establish the design criteria for using blood in LFA systems, Fig. 4.15 (a–c) presents the contours of the Damköhler number (Da) for different hematocrit levels, mapped over the plane of reaction rate of relevant blood analytes and the axial position along the paper strip. A critical Damköhler number (Da_C) of 50 (>>1) is considered to identify the optimized reaction zone, where the reaction rate significantly exceeds the flow rate. The results show that increasing the hematocrit level from 24.75% to 48.5% moves the reaction zone upstream where the Da reaches its critical value Da_C. This behavior is

primarily due to the decrease in average wicking velocity (see Fig. 4.12(d)), which increases the species residence time and thereby promotes more efficient reaction. These criteria are crucial for designing LFAs for diagnostic applications involving blood samples. To this end, we have fitted the locus of Da_C for all hematocrit level to estimate the critical axial length for test line design of LFA using power law fitted model as:

$$x_C = YH_C^a r^b \tag{4.19}$$

Here, x_C (in mm), H_C (in percentage) and r (in s^{-1}) are critical axial location, hematocrit level and reaction rate respectively. Using the log-log OLS regression (Ordinary least square regression), the values of coefficient (Y) and exponents (a, b) are obtained as $Y = 1.3187 \times 10^4$, $a = -1.6466$, $b = -0.6829$ within the 95 % confidence range. Hence, this expression provides the information for estimation of optimal reaction zone location at any hematocrit level of the blood.

4.6. CONCLUSIONS

In summary, the present study attempted to explore the coupled effects of fluid rheology and analyte trapping on the wicking phenomenon of NaCMC solution in a gel blot porous paper strip from the perspectives of experiments, theoretical analysis and simulations. We considered aqueous solution of NaCMC as the non-Newtonian liquid in this endeavor. Also, we have studied the wicking phenomenon of human blood in the gel blot paper strip and outlined the relevant design guidelines for efficient LFA, largely used in point of care diagnostics. In addition, we undertook an attempt to estimate the shear-rate dependent bulk effective viscosity of the non-Newtonian liquids (NaCMC and human blood) inside the complex porous media. We also developed a numerical modelling framework to simulate the saturation-based flow of non-Newtonian fluid in porous paper strips using Brooks and Corey parameters. In first part, we found that increasing the NaCMC concentration results in higher liquid entry pressure and a lower pore size distribution index. The lower pore size distribution index at higher NaCMC concentrations suggests increased flow heterogeneity in the paper strip. On comparing the experimental results to the simulated saturation-based flow field, estimated by using Brooks and Corey parameters, we found that the liquid saturation level was precisely predicted. Furthermore, the Raman analysis reveals that larger NaCMC concentrations result in a greater number of stable hydrogen bonds owing to the increased intensity of the hydroxyl group, which in turn, is able to trigger the effective viscosity in paper-strip. Consequently, the effective viscosity has been observed to exhibit increasing trend with the increasing concentration of

NaCMC. Interestingly, the effective viscosity ratio has been determined to be less than unity at lower NaCMC concentrations at longer time instants. This is because the underlying flow experienced less viscous owing to the predominant shear-thinning nature and less hydroxyl groups at lower NaCMC concentration. The viscosity ratio, on the other hand, increased by the order of magnitude when NaCMC concentration increased due to the higher flow resistance caused by greater number of hydrogen bonding. The average wicking velocity and wicking length, therefore, decreased with increasing the magnitude of NaCMC concentration in the aqueous solution. To understand the analyte trapping characteristics, we investigated the trapping efficiency and probability of a food dye particle in a paper strip in a non-Newtonian background. We found that the overall trapping efficiency is dominated by diffusion and interception processes, while inertial mechanism-induced particle trapping is insignificant. Because the background liquid viscosity varies with flow, the change in diffusion coefficient of dye particles does as well. This effect resulted in a non-monotonic variation in diffusive Peclet number as NaCMC concentration increased. Accordingly, both the diffusion and overall theoretical trapping efficiency were seen to exhibit a non-monotonic trend with increasing the magnitude of NaCMC concentration in the solution. Also, we observed that increased NaCMC concentrations at lower axial locations in the paper strip increase both trapping efficiency and probability. Consequently, it has been found that as the concentration of NaCMC increased, the critical axial location of the test line for the effective reaction in the LFA design decreased.

Finally, we have found that wicking length and average wicking velocity of blood reduce with increase in hematocrit level. In addition, the effective viscosity of blood in paper strip enhances with hematocrit level. Whereas, the temporal variation of effective viscosity is found to be non-monotonic. Due to the shear-thinning nature of the blood, the viscosity ratio is found to be less than unity in the specific range of time interval for all hematocrit levels considered in this study. The Raman analysis of blood in paper strip witnesses the existence of O-H, C-H and C-C stretching bonds, which is strongly dependent on the hematocrit level. Moreover, the optimum test line location for efficient species reaction in blood has been calculated from the critical Damköhler number (>>1). We have also developed the mathematical expression of critical axial location as a function of hematocrit level and reaction rate, essentially to provide the design guidelines for LFA. Overall, the inferences drawn from this study seem to provide adequate insight into the perspective of coupled influences of fluid rheology and analyte trapping on the underlying wicking phenomenon in paper pathways. We believe that the results of this endeavor are

deemed pertinent for the successful design of LFA, largely used as low-cost diagnostic tools for non-Newtonian liquid samples.

CHAPTER 5

DEVELOPMENT AND VALIDATION OF A LOW-COST PAPER-BASED MICROFLUIDIC PLATFORM FOR COLORIMETRIC METHANOL DETECTION IN ALCOHOLIC BEVERAGES

This chapter explores the fabrication and experimental validation of a paper-based lateral flow assay for the quick, economical detection and quantification of methanol in alcohol-based beverages. The research integrates capillary-driven transport with colorimetric chemical reactions by dry-storing chromotropic acid in the paper substrate. A computational framework is established to simulate imbibition dynamics, species movement, and reaction kinetics, facilitating the prediction of spatial and temporal colour changes. A quantifiable colorimetric index for methanol concentrations pertinent to toxicity limits is established using experimental results and normalized intensity of chromogenic complex on paper. A portable, self-driven diagnostic platform and useful design guidelines for field-deployable chemical sensing in resource-constrained environments are provided by the suggested method.

5.1. OBJECTIVE

Alcohol consumption presents significant public health issues, with methanol exposure constituting a particularly grave hazard due to its high toxicity (da Costa Sousa *et al.* 2024; Roy *et al.* 2021). Ingestion, inhalation, or dermal absorption of methanol can result in irreversible harm to the visual and neurological systems and may be death, with documented fatal dosages in people. Methanol poisoning transpires when methanol is processed by alcohol dehydrogenase in the liver. Due to its reduced cost relative to ethanol, methanol is occasionally used illegally to adulterate alcoholic beverages, resulting in multiple poisoning incidents documented in various countries, including India. Regulatory bodies have indicated that methanol levels in illicit spirits surpass acceptable thresholds, highlighting the critical necessity for swift detection.[4]

Traditional methods for methanol detection, including gas chromatography, spectroscopy, and sensor-based approaches, provide great sensitivity but necessitate costly equipment, skilled operators, and laboratory facilities, so restricting their use for on-site

[4] Content of this chapter is published in the journal of **Physics of Fluids (AIP), Volume 36, Issue 12, Page 123619, December 2024,** https://doi.org/10.1063/5.0245824

screening. Recently, paper-based microfluidic devices have evolved as economical, portable diagnostic platforms for chemical and biological investigation, utilizing capillary-driven flow without external power sources. Although successful in identifying different analytes, paper-based detection of methanol in alcoholic beverages remains unexamined.

Driven by this gap, the current project attempts to create a microfluidic methanol detection system employing Grade 1 paper. The adaptation of the chromotropic acid colorimetric assay to a paper-based format minimizes reagent usage, streamlines the testing process, and facilitates rapid, economical, and on-site screening, all while preserving sensitivity and specificity.

5.2.THEORETICAL MODELLING

5.2.1. Theory of chemical analysis

The reaction of methanol with potassium permanganate ($KMnO_4$) in the presence of sulfuric acid (H_2SO_4) has been performed in a 1.5 ml centrifuge tube, as schematically shown in Fig. 1. The underlying reaction results in the oxidation of methanol (CH_3OH) to formaldehyde (HCHO). In this reaction, $KMnO_4$ acts as a powerful oxidizing agent, and H_2SO_4 provides the necessary acidic environment for oxidation. Methanol is oxidized to formaldehyde, while the $KMnO_4$ is reduced. This reaction is significant in organic chemistry for demonstrating the oxidative capabilities of permanganate and for producing formaldehyde from methanol under controlled conditions.(Ranny 1965) A brownish-purple color is achieved by the reduced $KMnO_4$ into manganese dioxide (MnO_2).The summarized balanced equation for this reaction is written as follows:

$$3CH_3OH + 2KMnO_4 + H_2SO_4 \rightarrow 3HCHO + K_2SO_4 + 2MnO_2 + 4H_2O \quad (5.1)$$

In the next reaction, the excess $KMnO_4$ and the reduced MnO_2 from the previous reaction is reacted with sodium bisulfite ($NaHSO_3$) in the same centrifuge tube. The $KMnO_4$ and MnO_2 is reduced, and $NaHSO_3$ is oxidized. The reaction takes place in an acidic environment, often with H_2SO_4 that was added in previous reaction. $KMnO_4$, which is a strong oxidizing agent and MnO_2, is reduced to colorless Mn^{2+} (forming $MnSO_4$ in the presence of H_2SO_4), while $NaHSO_3$, acting as a reducing agent, is oxidized to $NaHSO_4$.(Saadat and Rafizadeh 2019) This step was done to prevent the interference of purple color of permanganate and brown color of manganese dioxide in the experiments. The balanced equation for this reaction is written as follows:

$$2KMnO_4 + 5\ NaHSO_3 + 3H_2SO_4 \rightarrow K_2SO_4 + 2MnSO_4 + 5NaHSO_4 + 3H_2O \quad (5.2)$$

$$2MnO_2 + 3NaHSO_3 + 3H_2SO_4 \rightarrow 2MnSO_4 + 3NaHSO_4 + 3H_2O \quad (5.3)$$

In the next reaction, previously formed formaldehyde is reacted with dry stored chromotropic acid (1,8-dihydroxynaphthalene-3,6-disulfonic acid) in the presence of concentrated H_2SO_4 results in the formation of an intense violet complex (Fagnani 2003). This reaction was performed on the paper microfluidic device as illustrated in the Fig. 5.1. The aforementioned reaction equation is written as follows:

$$2\,\text{HCHO} + \text{chromotropic acid} + H_2SO_4 \rightarrow \text{violet complex} \quad (5.4)$$

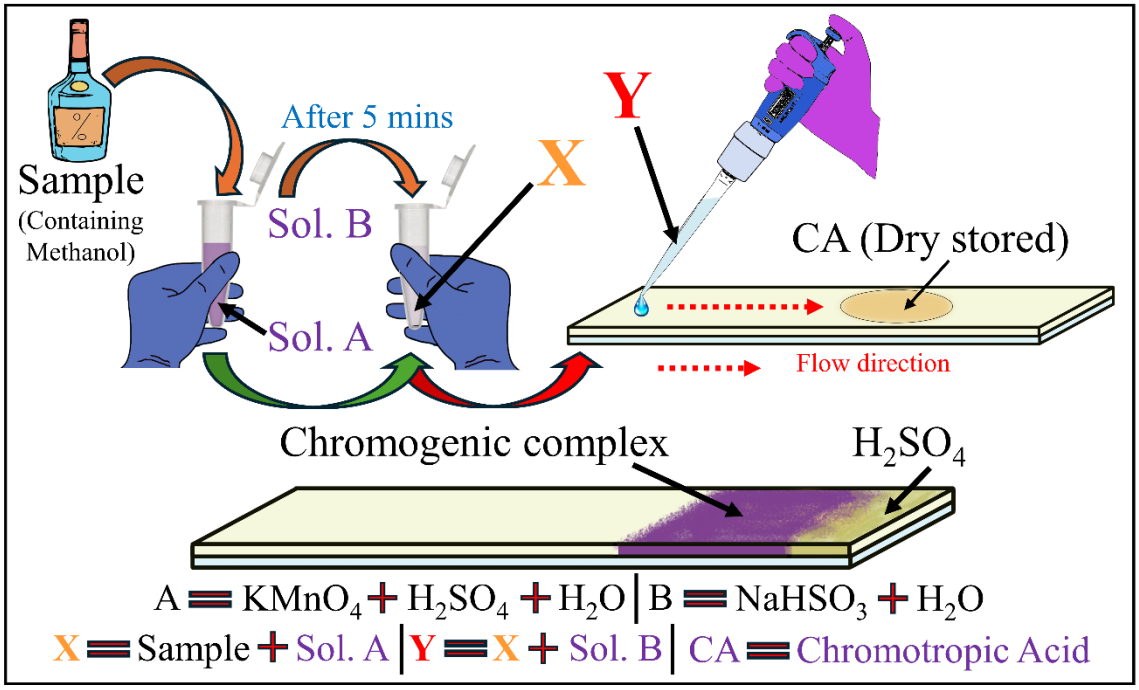

Figure 5.1. Schematic diagram of methanol detection on Grade 1 filter paper by wicking sample Y which interacts with previously dry stored chromotropic acid and H_2SO_4. The presence of methanol is detected by different intensity of color because of the presence of chromogenic complex.

5.2.2. Theory of mathematical modelling

5.2.2.1. Numerical modelling of flow in paper-based lateral flow assay

The mass conservation equation in porous media for the i^{th} phase, wetting (liquid, solution Y) and non-wetting phase (air), is given as (Rath *et al.* 2018d; Rath and Panda 2019; Toley *et al.* 2018):

$$\frac{\partial\left(\phi\rho_{\rho_{s_{ei}}}\right)}{\partial t} + \nabla\cdot\left(\rho_{s_{e_i}}\boldsymbol{u}_i\right) = 0 \quad (5.5)$$

Here, the volumetric flow per unit breadth can be written as: $\boldsymbol{u}_i = -\left(\frac{k_{rs_{e_i}}}{\mu_{s_{e_i}}}\right) k_{eq}\nabla p_{s_{e_i}}$; moreover, for saturation level, s_{e_i}; k_{eq}, $k_{rs_{e_i}}$, $\mu_{s_{e_i}}$and $p_{s_{e_i}}$are the equivalent permeability

of the porous medium, permeability ratio, dynamic viscosity and pressure field, respectively. The mathematical expression of normalized liquid saturation level is defined as $\overline{Se} = \frac{w - w_{dry}}{w_{sat} - w_{dry}}$. Here, w, w_{dry} and w_{sat} are weight of the sample when it is dry and when it is fully saturated, respectively.

The permeability ratio of the wetting (w) and non-wetting (n) phases in the event of 100% saturation is given as $k_{rs_{e_w}} = \overline{S}_e^{\left(3+\frac{2}{\lambda_p}\right)}$ and $k_{rs_{e_n}} = (1 - \bar{S}_e)^2 \left(1 - \left(1 - \overline{S_e}\right)^{\left(1+\frac{2}{b}\right)}\right)$, respectively. Additionally by applying the Brooks and Corey correlation, the correlation between normalized saturation and capillary pressure is expressed as follows:(Behera *et al.* 2023c)

$$p_c\left(\overline{S_e}\right) = p_{en}\overline{S_e}^{-\frac{1}{\lambda_b}} \tag{5.6}$$

Where, P_{en} (= 3325 Pa) and λ_b (= 1/4.45), respectively, stand for Brooks and Corey model parameters for water and Grade 1 paper (Behera *et al.* 2023c).

The continuity equation can be written in its combined form with Darcy's law as follows:

$$\frac{\partial(\phi\bar{\rho})}{\partial t} + \nabla \cdot (\bar{\rho}\bar{\boldsymbol{u}}) = 0 \tag{5.7}$$

Here, Darcy's law provides us with $\bar{\boldsymbol{u}} = \frac{k_{eq}}{\bar{\mu}}\nabla p$, averaged density is given as $\bar{\rho} = \sum_i s_{e_i}\rho_i$, and dynamic viscosity is written as $\bar{\mu} = \frac{\bar{\rho}}{\sum_i s_{e_i}\frac{\rho_i}{\mu_i}}$.

We consider two-dimensional rectangular computational domain for paper-strip having length and width of 5 cm and 4 mm, respectively, as illustrated in Fig. 5.2. We employ the following set of boundary conditions to numerically solve the transport equations [Eqs. (5.5) and (5.7)] as follows: At the inlet: $\boldsymbol{n} \cdot \left(\rho_{s_{e_i}}\boldsymbol{u}_i\right) = 0$, $p_g = 0$; For the top and bottom ends: $\boldsymbol{n} \cdot \left(\rho_{s_{e_i}}\boldsymbol{u}_i\right) = 0$ and $\boldsymbol{n} \cdot (\bar{\rho}\bar{\boldsymbol{u}}) = 0$; where, $\mathbf{n}$ represents the normal from the wall surface. At the outlet: For Darcy's equation, verifying capillary pressure equals zero, corresponding to entirely saturated paper, we have taken $p = -p_c\prod\left(\overline{S_e}\right)$; here, $\prod\left(\overline{S_e}\right)$ indicates the smoothed step function. The value of step function, $\prod\left(\overline{S_e}\right)$ is 1 when $\overline{S_e}$ varies from 0 to 0.9, and smoothly decreases at $\prod\left(\overline{S_e}\right)$ = 0 with increase in $\overline{S_e}$ from 0.9 to 1. It is worth noting that this estimation acts as a boundary condition for Eq. (5.5). We employ weak constraints to determine the exact flux at that border. Moreover, the

Lagrangian multiplayer (LM_p, unit: $\mathrm{kg/(m\text{-}s)}$), the shape functions of pressure are employed at the outflow to accurately determine the mass flux ($\mathrm{kg/(m^2\text{-}s)}$) therein for Eq. (5.4). Therefore, the normal mass flux at the outlet is described as $-\boldsymbol{n}\cdot\left(\rho_{s_{e_i}}\boldsymbol{u}_i\right)=\frac{LM_p}{h}$. We have assumed a wetting angle of zero degree due to the high hydrophilic nature of the Grade 1 filter paper.(Patari *et al.* 2023) Here, h is the thickness of the paper i.e., 0.185 mm. Moreover, LM_p acts as a new variable.

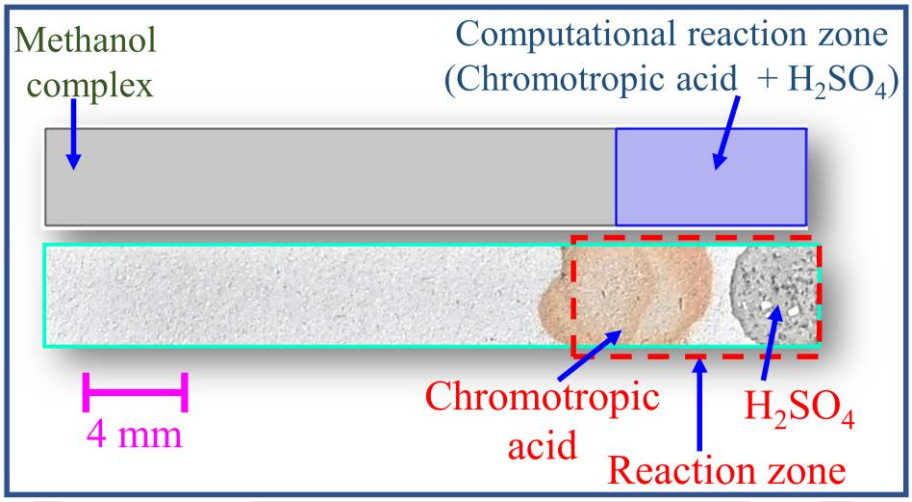

Figure 5.2. The top part illustrates computational domain with methanol complex at the inlet along with the computational reaction zone (right-side) with dry-stored chromotropic acid and H_2SO_4 solution. The bottom part depicts of experimental Grade 1 paper strip along with the dry-stored chromotropic acid and H_2SO_4 solution in the reaction zone.

5.2.2.2. Numerical modelling of reaction on paper strip

Below, we write the temporal convection-diffusion-reaction equation for species transport in paper strip.

$$\frac{\partial c_i}{\partial t}-\nabla\left[D_i\frac{\phi}{\phi^{-1/3}}\nabla c_i\right]+\boldsymbol{u}\cdot\nabla c_i=R_i \qquad (5.8)$$

Here, i = 1, 2, 3, indicating methanol complex, Chromotropic acid+H_2SO_4 complex (solution Y), and chromogen complex, respectively. The inlet concentration is taken as methanol concentration (v/v×247.187) in $\mathrm{mol/m^3}$, initial concentration of Chromotropic acid+H_2SO_4 complex Chromotropic acid+H_2SO_4 complex is presumed as same and equal to 247.187 $\mathrm{mol/m^3}$. The reaction rate, R_i, is evaluated in terms of normalized intensity of dark purple colour and only normalized intensity of product is estimated in the numerical simulation. We have considered that the dark purple intensity underscores the presence of methanol in the sample. Additionally, the diffusion coefficient for all species is taken to be 10^{-9} $\mathrm{m^2/s}$. It should be noted that this value corresponds to an appropriate order of

magnitude based on the molecular size in Angstroms, as determined by the Stokes-Einstein relation (Gisladottir *et al.* 2009; Miller and Walker 1997).

5.3. EXPERIMENTAL METHODOLOGY

5.3.1. Materials, reagents and equipment details

For the experiments, we have taken Potassium permanganate ($KMnO_4$), dilute and concentrated sulphuric acid (H_2SO_4), and sodium bisulphite ($NaHSO_3$) from Finar Limited®. Chromotropic acid has been procured from SRL®, methanol (CH_3OH) from Merck® and Grade 1 filter paper from Whatman™. Abdos® centrifuge tubes (2 ml, 5 ml, 15 ml), Abdos® falcon tubes (15 ml, 50 ml), Tarson® micro pipettes and Abdos® pipette tips have been used for the preparation of solutions. Distilled water is used as a solvent for all the solutions considered in this study. The Interfacial Rheometer (Anton Paar, Model: MCR 301) has been used to measure the viscosity of sample having varied methanol concentrations. The rheometer quantifies dynamic viscosity by evaluating a fluid's resistance to deformation when subjected to shear stress. The methanol sample is placed in a stationary cup, while a rotating cone is immersed in the cup-and-cone arrangement. The rotating cone exerts a controlled shear rate on the fluid. The device then quantifies the resultant torque, which correlates to the fluid's flow resistance. The rheometer calculates dynamic viscosity by assessing the torque and shear rate. We performed our viscosity measurement experiment thrice for each concentration of methanol in the sample by varying the shear rate in the rheometer and computed the average of the recorded measurements.

5.3.2. Preparation of reagents

In order to prepare 0.1 M $KMnO_4$ solution, 0.079 grams of $KMnO_4$ has been dissolved in 5 mL of water. A 0.5 M H_2SO_4 solution has been prepared by adding 0.139 mL of 18 M H_2SO_4 in 5 mL of water. A 0.5 M sodium bisulfite ($NaHSO_3$) solution has been prepared by dissolving 0.26 grams of $NaHSO_3$ in 5 mL of water. Ultimately, a quantity of 1.766 grams of chromotropic acid is completely dissolved in 5 mL of water, resulting in the formation of a solution with a concentration of 1 mole per litre.

5.3.3. Preparation of Whatman™ grade 1 paper strip and experimental conditions

A rectangular strip of Whatman™ Grade 1 filter paper with dimensions 40 mm length and 4 mm width has been made by cutting it using a craft knife. The strip was thereafter meticulously positioned and affixed to transparent cello tape, ensuring the absence of any creases or air pockets. The surplus tape was cut off in order to ensure a neat

boundary, which enhances the wicking process by adding additional reinforcement. The capillary wicking experiments were conducted at ambient conditions, with temperature of 27 ± 2°C and a relative humidity of 84 ± 2 %. These parameters were maintained to ensure that the underlying wicking phenomenon is independent of environmental conditions.

5.3.4. Dry storing

A concentrated spot of chromotropic acid has been created on a 40 mm by 4 mm rectangular strip of Whatman™ Grade 1 filter paper. A 1 M chromotropic acid solution has been prepared and dropwise 4 µL was placed to a specific spot on the strip using a pipette. Appealing to air drying operation after the first application, the process has been repeated with a second drop on the same spot. The strip is briefly placed under a dryer, resulting in a concentrated area of dry stored chromotropic acid. This similar dry-storing technique has been used for nanoparticles in the microfluidic paper (Kumari *et al.* 2024). Aside from this, no additional pre-treatment is performed on the paper strip.

5.3.5. Image processing and data analysis

Images of the paper-based device with coloured chromogenic complex were taken with a Nikon Z 50 camera, and the area was illuminated with a Schott LED light. To calculate the grey-scale intensity, we used 830 × 125 pixels of the paper strip. The gray scale intensity of the chromogenic and white regions of paper in 60-frame-per-second movie has been tracked using MATLAB® software. The processing of each second frame has been carried out using ImageJ® (free source). Furthermore, the obtained color intensity data has been normalized following the procedural steps as illustrated in Fig. 5.3.

The grayscale intensity of the white region (M) and the colored region (N) is measured, then the ratio is calculated $a = N/M$ for each time, $t = i$ ($0 \leq i \leq 20$ seconds). Further, the value 'a' is calculated by dividing each by its corresponding value at $t = 0$ seconds to get $b = (a_i/a_{t=0})$. The intermediate normalized intensity for any sample concentration has been calculated as $c = (a_i - a_{t_{i=20}})/(a_{t_{i=0}} - a_{t_{i=20}})$, which ranges from 1 to 0. The value 'c' is then subtracted from 1 to get d = 1−c. Further, the multiplying factor has been determined as, $e = (b_i - b_{i=20})/(b_{30\%_{i=0}} - b_{30\%_{i=20}})$, where $b_{30\%_{i=0}}$ and $b_{30\%_{i=20}}$ are the normalized ratios for standard 30 % (v/v) methanol sample at 0 s and 20 s after the contact of solution Y with dry stored chromotropic acid and H_2SO_4. Finally, the final normalized intensity is calculated as $f = e \times d$. This method provides a systematic approach for accurate prediction of normalized colorimetric methanol intensity.

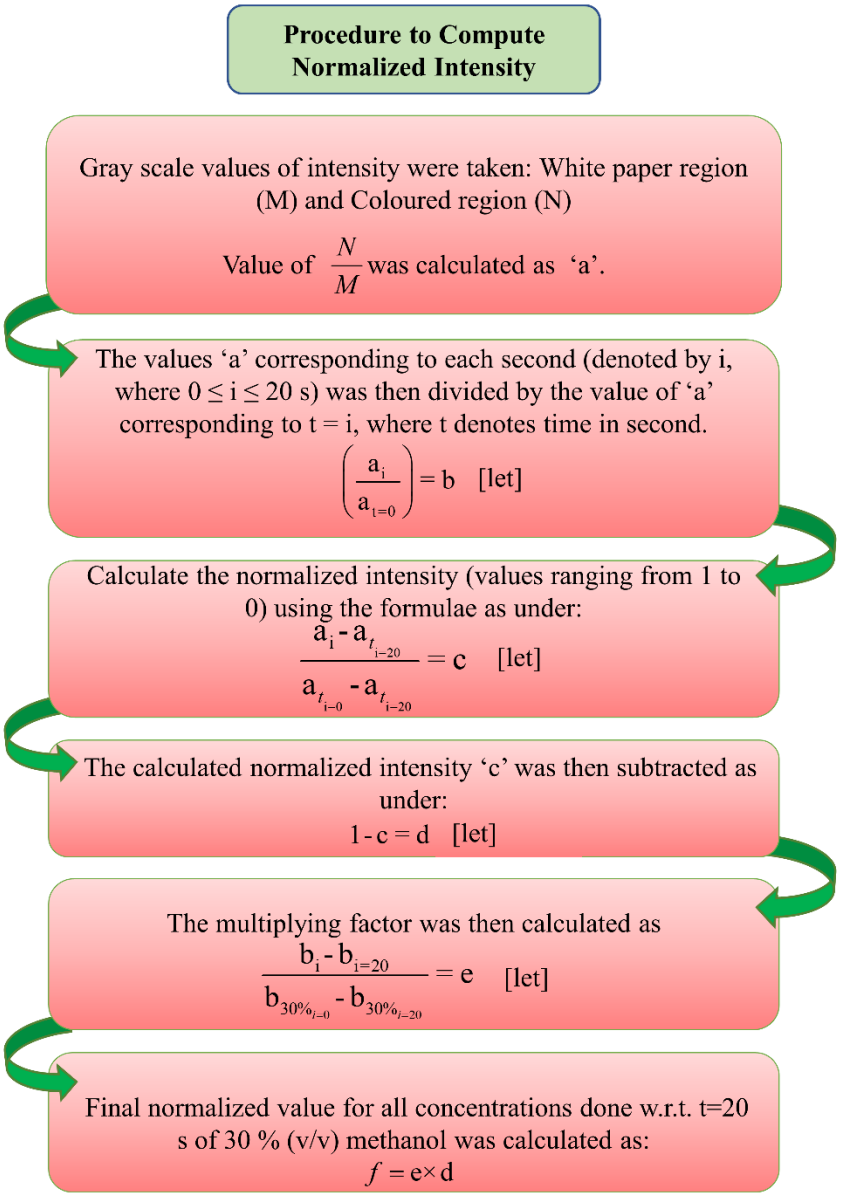

Figure 5.3. Flow chart outlining each step in calculating the normalized color intensity of the methanol sample with respect to 30 % (v/v) methanol color intensity at t = 20 s after contact on "Grade 1" paper. Varying the type of paper used may influence the resultant color intensity due to the pore size and paper type of the porous material.

5.4. RESULTS AND DISCUSSION

This study involves the development of a mathematical model, subsequently validated through our experimental results, for analyzing the imbibition dynamics through a paper-based lateral flow assay, designed for rapid detection of methanol in alcoholic beverages in a cost-effective manner. The normalized intensity of the chromogenic complex is determined by reacting it with dry stored chromotropic acid and H_2SO_4. This reaction is carried out by wicking the Y solution (as shown in Fig. 5.1) with methanol. In

addition, we have developed a numerical framework to calculate the wicking dynamics of solution Y on Grade 1 paper. Furthermore, we determined the reaction dynamics by calculating the normalized reaction rate of the chromogenic complex. We conducted experiments by varying the additional methanol percentage between 5 % (v/v) and 30 % (v/v) in the targeted sample. This allowed us to develop a colorimetric index, which we then used to test and verify the accuracy of branded alcohol and local alcohol samples with variable levels of methanol.

5.4.1. Wicking of solution Y

Due to the strong correlation between liquid wicking and viscosity, our initial analysis focuses on determining the dynamic viscosity of wicking solution Y. Figure 5.4 illustrates the relationship between the change in methanol concentration and the variation of dynamic viscosity in solution Y. It has been observed that the viscosity of the solution Y increases as the concentration of methanol increases. The higher activation energy of methanol compared to water enables more external energy to be used to commence the flow by breaking intermolecular attachment (Macedo and Litovitz 1965; Shah *et al.* 2016). Therefore, an increase in methanol concentration leads to an increase in dynamic viscosity due to the increase in activation energy of the molecules. The fitted expression is obtained as follows in relation to the methanol percentage (v/v), denoted by V:

$$\mu = 1.453\times10^{-7}\times V^2 + 9.193\times10^{-6}\times V + 0.0011 \text{ Pa-s} \quad (5.9)$$

We have observed that the viscosity of concentrated H_2SO_4 is significantly higher (about 38 times more (Rhodes and Barbour 1923)) than that of solution Y. As a result, the wicking of H_2SO_4 through capillary action is not considered in the numerical simulations and is assumed to remain constant throughout the reaction area.

We demonstrate, in Fig. 5.5, the wicking of Y solution for 5 % (v/v) and 30 % (v/v) methanol content by depicting the liquid saturation level $\left(\overline{S_w}\right)$ of solution Y. As witnessed in Fig. 5.4, we find that wicking of lower concentration solution is faster as compared to 30 % (v/v) solution because of lower viscosity of 5 % (v/v) methanol solution.

Using the numerical results, we take an effort to calculate the wicking velocity. This allows us to provide with the information on the convective strength of species transport. Due to the inverse relationship between convective strength of species transport and species residence time, higher convective strength is not suitable for an efficient reaction in the designated region(s). Hence, the reaction line/region should be positioned in the location

where the species residence duration would be greater. As a result, we have identified a suitable place for dry storage of chromotropic acid with high species residence time.

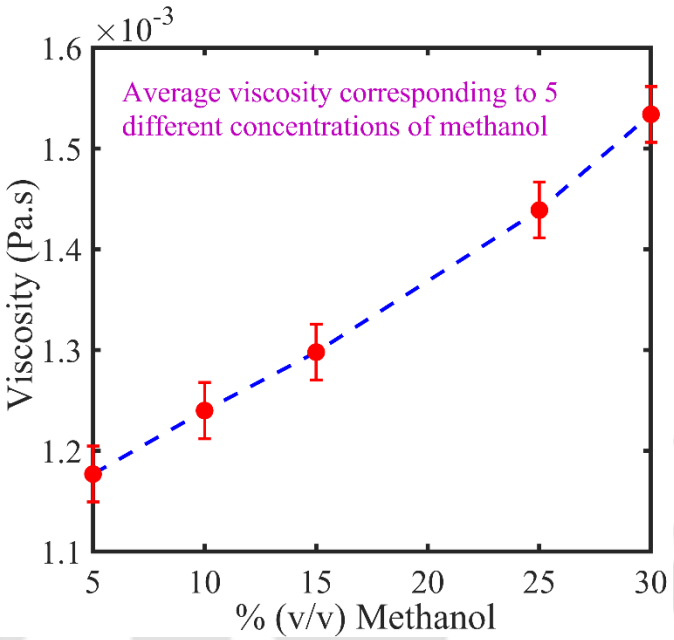

Figure 5.4. Variation of dynamic viscosity of solution Y with change in methanol concentration.

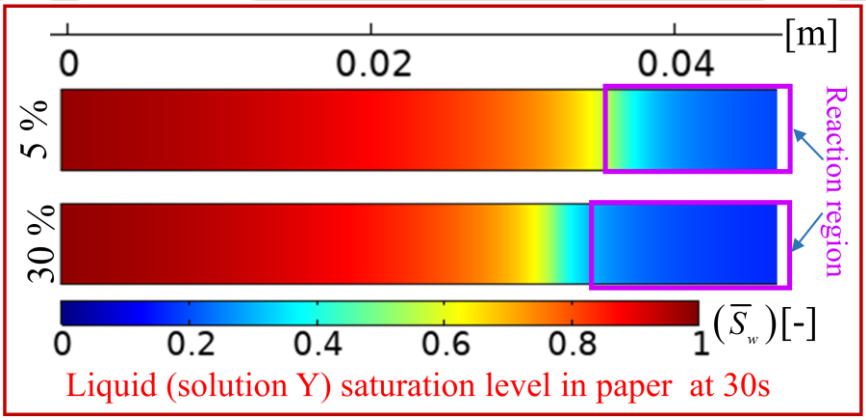

Figure 5.5. The depiction of normalized liquid saturation level of solution Y at 30 s for 5 % (v/v) and 30 % (v/v) implementing the two-phase (liquid of solution Y and air). The normalized saturation level of liquid (solution Y) is defined as the ratio of volume fraction of liquid (solution Y) present in porous medium to the total pore volume of that porous medium.

-This phenomenon can be represented by the diffusive Peclet number ($Pe = \frac{u_{avg} d_p}{D}$; here u_{avg}, d_p and D are average velocity, pore diameter and diffusion coefficient of species). Pertaining to the species transport phenomena, the diffusive Peclet number plays an important role as it underlines the relative contribution of convective strength to diffusion mechanism on the underlying transport inside the structured environment of the paper strip.

The species (chromotropic acid) remains dry stored in the reaction zone and it should get adequate time to complete the reaction effectively. When the diffusive Peclet number is less than one, diffusion-dominant transport takes over, extending the interaction period between the species and the methanol sample. So, we need to choose lower Peclet number, preferably less than unity. Higher Peclet number signifies that the species will be transported along with the flow at a relatively faster rate, which in turn, may result in insufficient reaction. Accounting for this, we have considered low Peclet number (less than unity) in the present analysis.

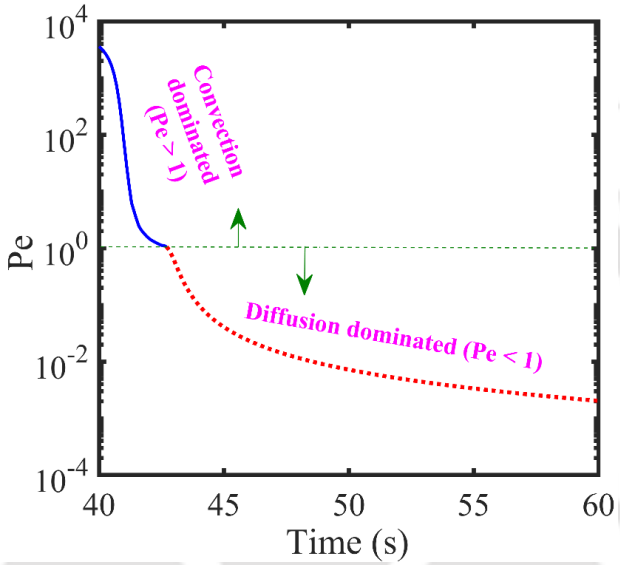

Figure 5.6. Variation of temporal diffusive Peclet number of 5 % (v/v) methanol solution during wicking of solution Y on paper strip.

Accordingly, the temporal variation of diffusive Peclet number of species with the diffusion coefficient order 10^{-9} m^2s^{-1}, is presented in Fig. 5.6. Between 40 and 45 seconds, the species transport mechanism transitions from convection to diffusion, shown by a change in the Peclet number from larger than one to less than one. Within the specified time intervals, the position is situated at a distance ranging from 3 to 4 cm from the sample/species loading point. Thus, we can conclude that the residence time is adequately enough in that specific area to ensure efficient completion of the underlying reaction. Accordingly, we considered that specific area for the storage of chromotropic acid in a dry state, as well as for the loading of a highly viscous and concentrated (98%) solution of H_2SO_4.

5.4.2. Determination of rate of reaction

We depict, in Fig. 5.7, the normalized intensity of chromogenic complex with change in time for different methanol percentages (v/v). Note that we calculate the

normalized intensity of chromogenic complex using the procedure outlined in Fig. 5.3. Normalization is performed based on the grayscale intensity acquired from a 30% (v/v) solution at t = 20 seconds after the solution Y comes into contact with chromotropic acid and sulphuric acid. To determine the normalized intensity of the chromogenic complex through numerical simulations, we have calculated the reaction rate in terms of normalized intensity per unit time. Consequently, we plot all the experimental curves obtained for solutions with concentrations of 5 % (v/v), 15% (v/v), and 30% (v/v) in Fig. 5.7. After calculating the slope of the fitted curves, shown in Fig. 5.7, we derive the following expressions for the reaction rate:

R_i = ((2×0.0007×t) +0.0237) normalized intensity of chromogen/s for 5 % (v/v) (5.10)

R_i =((2×0.0003×t) +0.0369) normalized intensity of chromogen /s for 15 % (v/v) (5.11)

R_i = (-(2×0.0016×t) +0.857) normalized intensity of chromogen/s for 30 %(v/v) (5.12)

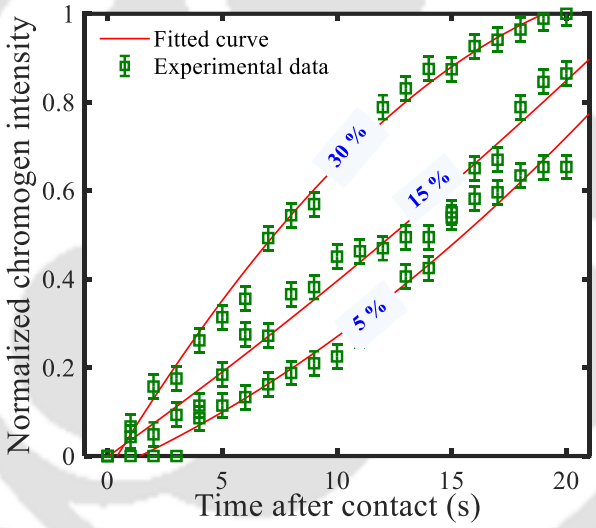

Figure 5.7. Normalized concentration of chromogen at different methanol percentage in % (v/v).

5.4.3. Numerical prediction of reaction on Grade 1 paper

We numerically calculate and present colorimetric change obtained from the experiment for 30 % (v/v) methanol content at the end of 20 s after the solution Y comes into contact with chromotropic acid and sulphuric acid on a paper strip. It is worth to mention in this context here that paper-based lateral flow assays, which can be fabricated in various simpler shapes, enable inexpensive detection technique providing with a rapid and sensitive visual colorimetric response (de Oliveira *et al.* 2017; Dungchai *et al.* 2011; Gong and Sinton 2017; Pradela-Filho *et al.* 2023; Xia *et al.* 2016). The paper-based lateral flow assay developed in this endeavour facilitates a quick visible reaction with intensified colour

within 20 s after contact. This eliminates the requirement for any additional instrument to detect the concentration of methanol in the samples. The reaction region on the considered paper strip has sufficient species residence time owing to the low Peclet number, attributed primarily to low convective strength of species transport (See Fig. 5.6). The simplicity and efficiency of the system contribute to its overall efficacy. The normalized concentration of the chromogenic complex has been determined through numerical simulations presented in Fig. 5.8, based on the previously stated estimated reaction rate described in Fig. 5.7. The simulated results produce an enhanced colour corresponding to the normalized intensity of the chromogenic complex at the reaction zone, which aligns with the experimental prediction as well. Hence, the current numerical model has the ability to accurately replicate the chemical kinetics involved with the detection of methanol in alcoholic beverages on a paper strip.

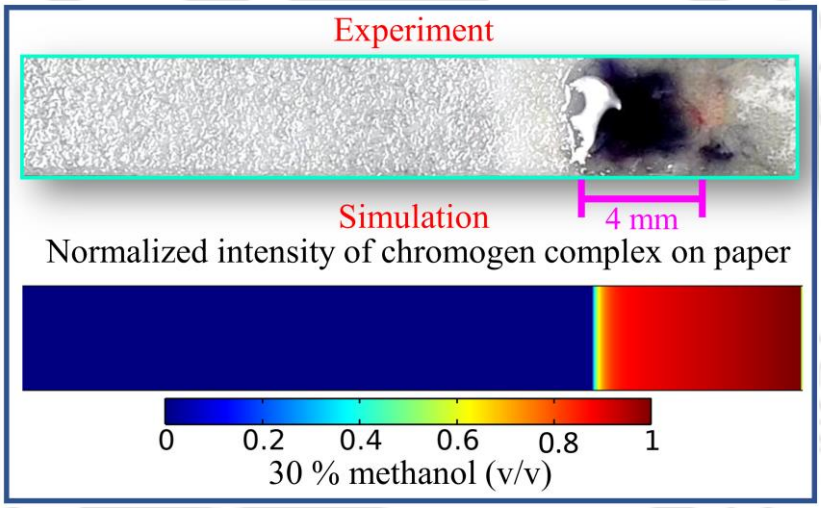

Figure 5.8. Comparison of experimental and simulation result at the end of 20 seconds after contact of solution Y with dry stored chromotropic acid and H_2SO_4.

For more information readers are referred to Figs. 5.9-5.11, which compare the color intensity of the chromogenic complex acquired from the experiments to the normalized intensity derived from the simulations at different time steps for 5 % (v/v), 15 % (v/v), and 30 % (v/v) methanol content. The temporal experimental and numerical contours at various methanol concentrations (v/v), as depicted in Figs. 5.9-5.11, exhibit a strong resemblance to one another. Therefore, the current numerical model has the credibility of predicting the changes over time in the normalized intensity of the chromogenic complex as a result of changes in methanol concentration. From the experiment, it has been observed that the intensity reaches a saturation point 20 seconds after the solution Y, chromotropic acid, and

H_2SO_4 comes into contact. Thus, we have specifically chosen a time interval of 20 s after contact to calculate the colorimetric indexing in relation to the methanol content.

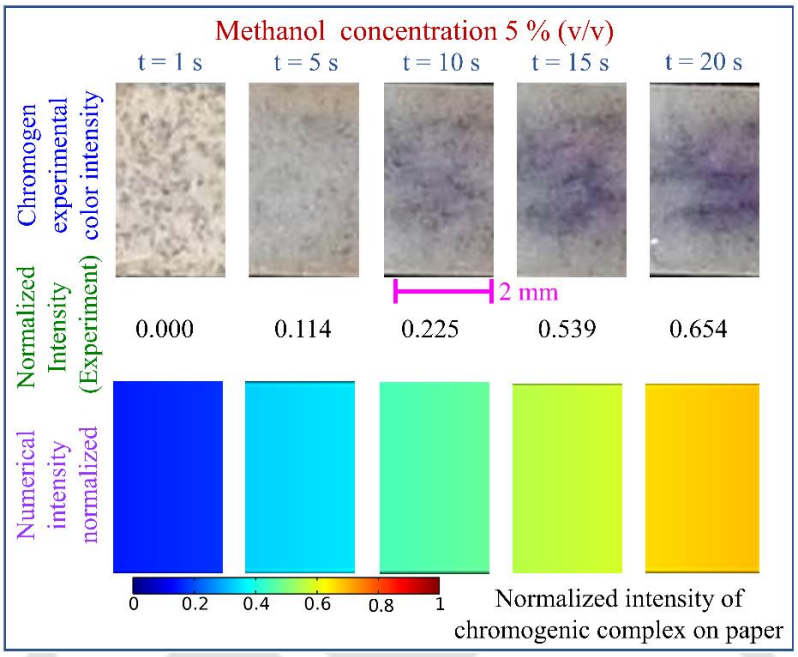

Figure 5.9. Comparison of normalized intensity of chromogenic complex on paper for 5 % (v/v) methanol solution. The starting time is denoted as the moment of initial contact between solution Y, H_2SO_4 and chromotropic acid, serving as the reference of time for all measurements.

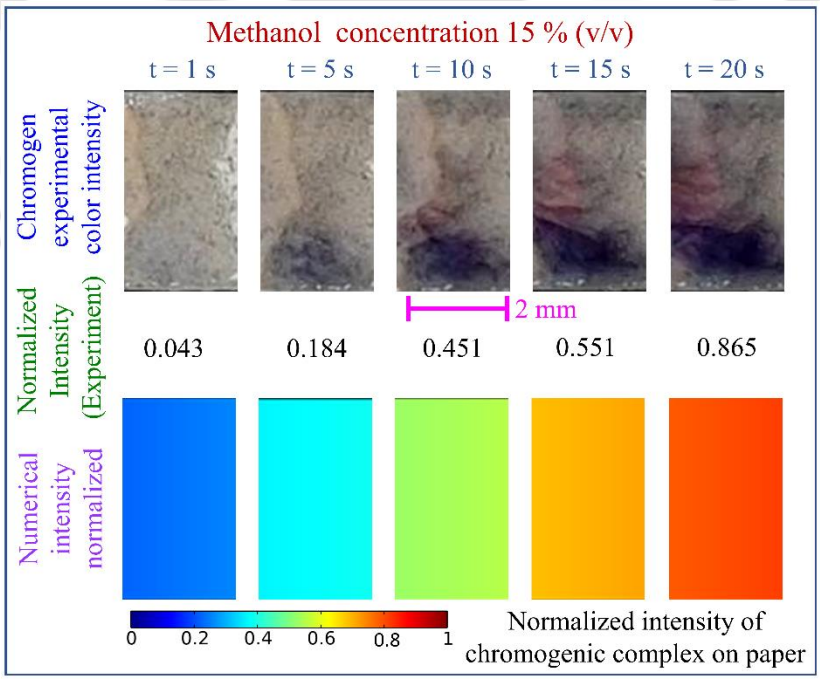

Figure 5.10. Comparison of normalized intensity of chromogenic complex on paper for 15 % (v/v) methanol solution. The starting time is denoted as the moment of initial contact between solution Y, H_2SO_4 and chromotropic acid, serving as the reference time for all measurements.

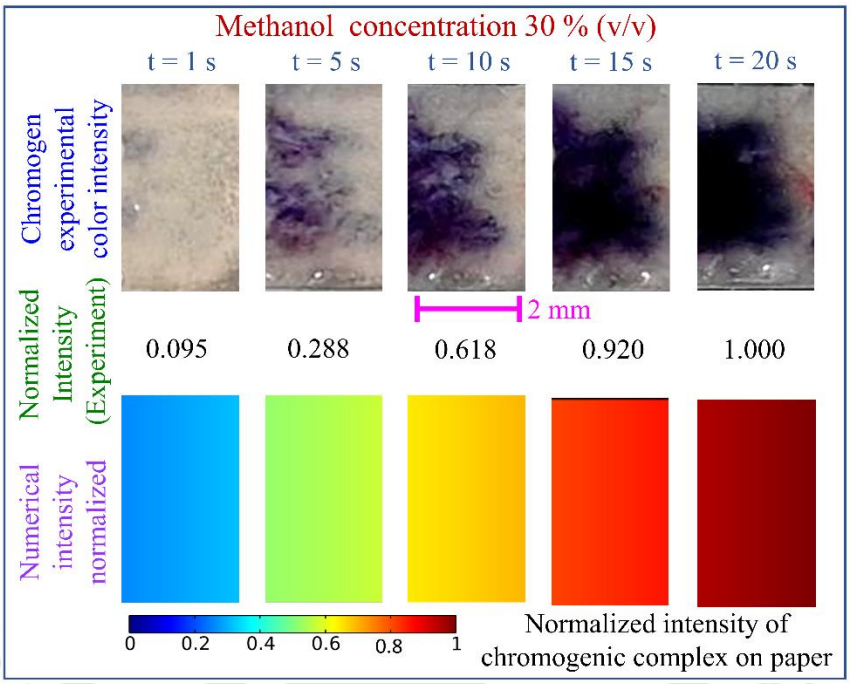

Figure 5.11. Comparison of normalized intensity of chromogenic complex on paper for 30 % (v/v) methanol solution. The starting time is denoted as the moment of initial contact between solution Y, H_2SO_4 and chromotropic acid, serving as the reference time for all measurements.

5.4.4. Development of colorimetric scale for methanol detection on paper strip

We have made an attempt to develop a colorimetric index using the normalized intensity of a chromogenic complex, as shown in Fig. 5.12(a). The color indexing has been categorized into labels 0 to XII, based on the concentration of methanol. The corresponding ranges can be found in Table 5.1 as well. In addition, we show the intensity of the chromogenic complex in relation to the concentration of methanol in Fig. 5.12(b) essentially to provide a clear grasp of the relationship between methanol concentration and color indexing. Using this color indexing method, we verify the concentration of methanol in both locally produced alcohol and branded vodka, as elaborated in the subsequent section.

Following the development of colorimetric indexing (see Fig. 5.12) for methanol detection, we examine the colorimetric response for local alcohol and branded vodka (lemon flavoured) for methanol detection. In order to verify the validity of the developed colorimetric scale, we considered pure samples of each component and added 5 % (v/v), 10 % (v/v), and 20 % (v/v) additional methanol for these tests. The colorimetric response for local alcohol is presented in Fig. 5.13(A). It can be observed that the pure form produces a mild colorimetric change (see Fig. 5.13A(i)), which has less intensity than the developed colorimetric scale (see Fig. 5.12). Therefore, this sample can be considered safe as the

colour intensity is far below the critical limit. As observed in Figs. 5.13A (i to iv), addition of further methanol percentage (by volume) permits colour indexing to lie in the range of O-I, III-IV, and VII-VIII for 5 % (v/v), 10 % (v/v), and 20 % (v/v), respectively. The obtained indexing indicates that the pure form of local alcohol has a very low methanol level, approximately less than ~2% (v/v). Paine (2001) states that the critical limit for methanol concentration is 8 % (v/v), considering safety issues as well as metabolic clearance of methanol for healthy human body. The methanol level in local alcohol appears to be less than ~2% (based on the colour indexing) when comparing Figs. 5.13 A (i to iv). Thereby, it is within the safety threshold defined by Paine (2001).

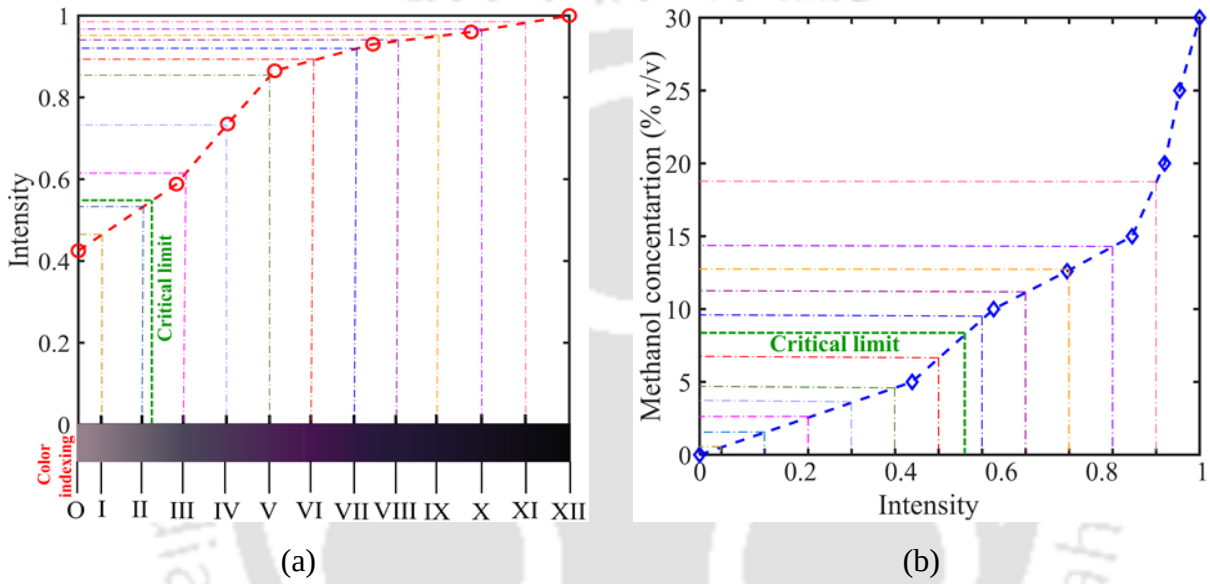

(a) (b)

Figure 5.12. (a) Normalized intensity of chromogenic complex from experimental data with colour indexing, (b) methanol concentration with change in intensity of chromogenic complex from experimental data.

TABLE 5.1. Indexing range corresponding to the methanol percentage in the sample.

Serial. number	Range of color indexing	Methanol percentage (v/v)
1	O to I	5 to 6.09 %
2	I to II	6.09 to 8.27 %
3	II to III	8.27 to 10.45 %
4	III to IV	10.45 to 12.63 %
5	IV to V	12.63 to 14.81%
6	V to VI	14.81to 17.00 %
7	VI to VII	17.00 to 19.17 %
8	VII to VIII	19.17 to 21.88 %

9	VIII to IX	21.88 to 24.06 %
10	IX to X	24.06 to 26.24 %
11	X to XI	26.24 to 28.42 %
12	XI to XII	28.42-30 %

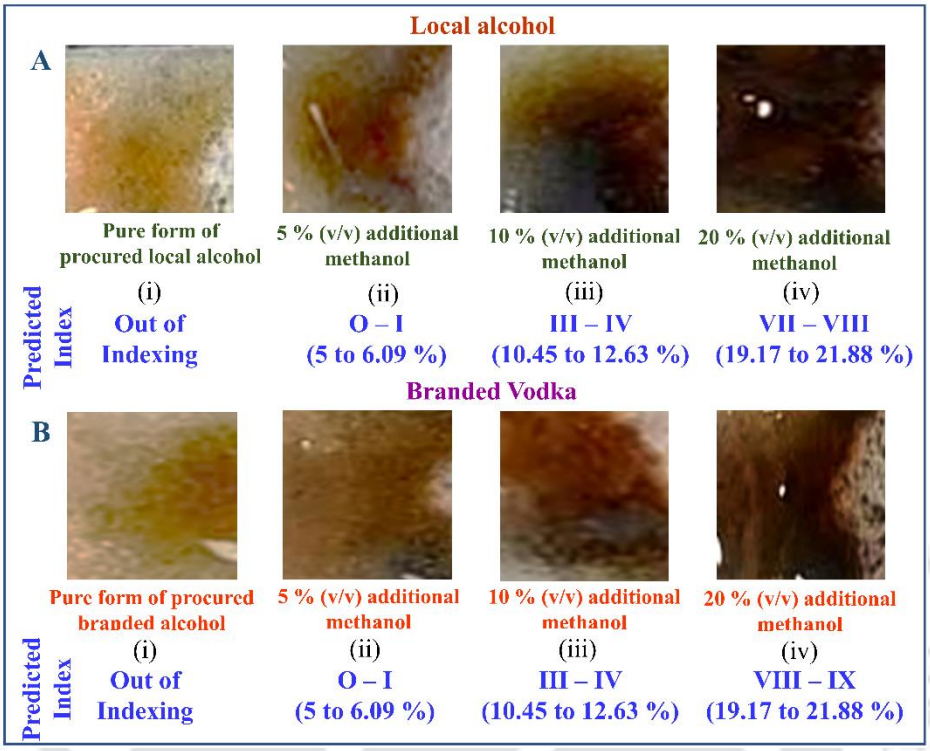

Figure 5.13. A (i, ii, iii and iv): Images illustrate the colorimetric testing of a locally made alcoholic beverage sample in pure form, 5 % (v/v), 10 % (v/v), and 20 % (v/v) additional methanol. Similarly, images in B (i, ii, iii and iv) denotes the testing of samples of a pure branded vodka, 5 % (v/v), 10 % (v/v), and 20 % (v/v) additional methanol.

Further, we have presented the colorimetric change of branded vodka in pure conditions (Fig. 5.13. B(i)) as well as additional methanol mixing of 5 % (v/v), 10 % (v/v), and 20 % (v/v) (Figs. 5.13. B(ii to iv)). As shown in Fig. 5.13B(i), pure branded vodka exhibits a pale colour whose intensity is less than the lower limit of the developed colorimetric index (refer to Fig. 5.12). As per literature and "Food Safety and Standards Authority of India" (FSSAI) (Safety and Act 2021), the accepted maximum limit for flavoured vodka has been set to be 0.2 % (v/v) (Wiśniewska *et al.* 2015). Accordingly, adding the extra methanol content in branded vodka allows not much extra deviation in colour indexing over the colour indexing of additional methanol percentage (v/v) (see Figs. 5.13B (iii to iv)). Therefore, the methanol concentration in pure form of branded vodka seems to be very less (approximately less than ~ 1 or 2 % (v/v) according to colour indexing

developed in Fig. 5.12) by observing the index level in extra added methanol. Thus, this comparison validates the accuracy of our colorimetric scale for detecting critical limit of methanol on a paper test strip.

In Table 5.2, we have emphasized the advantages of the present colorimetric paper-based microfluidic methanol detector compared to the traditional approaches such as gas chromatography (GC), metal-oxide gas sensor, dielectric sensor with TiO_2 nanotube, nitrogen-doped carbon-dots with fluorescence visualisation, and others (Bindra and Hazra 2020; Charapitsa *et al.* 2021; Latha *et al.* 2020; Soares *et al.* 2019; van den Broek *et al.* 2021, 2024; Zamani *et al.* 2019). The present technique is deemed cost-effective, user-friendly, and does not require sophisticated equipment for detecting methanol in alcoholic beverages. Moreover, the sample loading in the paper-based device is self-sufficiently propelled by virtue of capillary action. Thus, the current method as proposed in this endeavour is well-suited for detecting methanol beverage in remote regions where access to advanced instrumentation is limited.

TABLE 5.2. Details of previous conventional methods for methanol detection and advantage of the present paper-based device.

Sl. number	Reference	Technique details	Remark
1	Zamani *et al.* (2019)	Gas chromatography (GC) and a modified CA kit	The approach is not portable or easy to use. Limitations exist in the comparison made between the results of GC and the kit.
2	Van den Broek *et al*. (2019)(Soares *et al.* 2019)	Micromachined metal-oxide gas sensor housed inside a Teflon chamber using pump.	This sensor is costly due to the complex microchip design and is not self-driven because of the pump.
3	Bindra and Hazra (2020)	Dielectric sensor with TiO_2 nanotube. Signal-processing circuit detects the methanol contamination levels.	The whole arrangement is costly because of the nanotube manufacturing and due to the electrical circuit.
4	Van den Broek *et al*. (2021)	A handheld breath detector using a chemoresistive Pd-doped SnO_2 microsensor	The fully integrated electronic circuit makes the detector costly.
5	Charapitsa *et al.* (2021)	Gas chromatography (GC)	The use of bulky and costly GC equipment makes the approach complex.
6	Latha *et al.* (2020)	Nitrogen-doped oxidized carbon dots (NOCDs) are used as on-off nanoprobes (fluorescent) for detection of	The fluorescent based detection requires sophisticated instruments which makes it costly and lab-based.

		methanol traces in water and alcoholic beverages.	
7	van den Broek et al. (2024)	A handheld methanol detector Spark M-20 (Alivion AG, Switzerland) with a chemoresistive gas sensor to quantify methanol.	The handheld device is highly costly for use in low income countries.
8	Present study	Microfluidic paper-based self-driven device with dry stored chromotropic acid with colorimetric indexing.	• Self-driven: sample is loaded by capillary flow • Low-cost due to the use of grade 1 paper • No sophisticated device need because of the colorimetric indexing. • Relatively small in size and easy to handle. • Skilled personnel is not required for the use of the device

5.4.5. Selectivity of methanol detection in ethanol rich sample

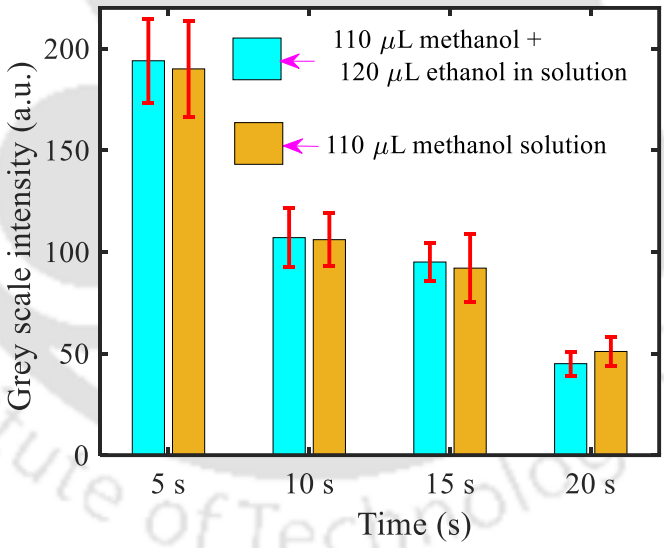

Figure 5.14. Comparison of grey scale intensity on paper strip at different times for solution (with methanol) having with and without ethanol content.

We have taken an effort to verify the methanol detection selectiveness on paper strip with solution having ethanol content as well. This situation is practical as the alcoholic beverages contain both ethanol and methanol (Bindra and Hazra 2020; Charapitsa *et al.* 2021; Latha *et al.* 2020; Soares *et al.* 2019; van den Broek *et al.* 2021, 2024; Zamani *et al.* 2019). Fig. 5.14 illustrates the grayscale intensity of the detected colour on the paper strip

having cases with and without ethanol content in the solution with methanol. It is observed that the grayscale intensity is nearly same for both the cases. It implies that the chromogenic complex is selective to detect methanol only in paper strip. The similar phenomenon has been observed by Ranny.(Ranny 1965) Hence, we can say that the developed paper-based LFA, targeted for colorimetric detection of methanol in alcoholic beverages, is selective to detect the methanol in alcoholic beverages which contains large amount of ethanol.

5.5. CONCLUSION

A low-cost paper-based detection method has been demonstrated for assessing methanol content in alcoholic beverages. The Whatman™ Grade 1 paper was selected as the test substrate due to its delayed resistance to the corrosive properties of H_2SO_4. Colorimetric analysis was conducted on samples spiked with methanol at 6 different concentrations (5 % (v/v), 10 % (v/v), 15 % (v/v), 20 % (v/v), 25 % (v/v), and 30 % (v/v)). The reagents were dry-stored on the test paper strip, with the storage location determined using numerical simulation. The diffusive Peclet number was found to be around unity in the vicinity of the reaction zone, which was favourable during the experiment because of the sufficiently larger residence time available. According to the literature, the lethal critical limit for methanol in alcoholic beverages, is approximately 8 % (v/v). The present test strip is capable of accurately measuring methanol concentrations ranging from 5 % (v/v) to a toxic threshold of 30 % (v/v). A colour indexing chart was developed for general use, allowing individuals to correlate the colour on the test strip with methanol concentration. The colours generated at various methanol concentrations on the test strip were analyzed using ImageJ® software, and the grayscale intensities were calculated. The intensities were subsequently standardized in relation to the sample containing a methanol concentration of 30 % (v/v). Transient numerical simulations were conducted for methanol concentrations of 5 % (v/v), 15 % (v/v), and 30 % (v/v) to provide further insights. In addition, the methanol concentration of both a branded and a locally made alcoholic beverage were examined, validating the accuracy of the established colorimetric index.

CHAPTER 6

CONCLUSIONS AND SCOPE OF FUTURE WORK

This chapter discusses the significant results derived from the research objectives explored in this dissertation, along with prospective directions for future research.

6.1 SUMMARY AND OUTLOOK

This dissertation conducts a thorough examination of capillary-driven transport mechanisms in paper-based porous media, focusing on solute concentration, immiscible interfacial effects, non-Newtonian rheology, and reaction-transport coupling in lateral flow assay (LFA) platforms. This study enhances the fundamental comprehension of wicking, permeability modulation, pore-scale multiphase dynamics, and analyte transport in cellulose-based substrates pertinent to economical diagnostic and sensing applications through a systematic integration of experiments, analytical modeling, and numerical simulations.

A summary of the research problems this dissertation addresses is as follows:

- Experimental, analytical, and numerical investigation of concentration-dependent solute imbibition and permeability variation in paper-based porous media.
- Experimental and pore-scale numerical investigation of immiscible interfacial transport and droplet generation in paper microfluidic structures.
- Investigation of rheology-modulated imbibition and analyte transport/trapping in paper substrates using non-Newtonian fluids.
- Development and validation of a paper-based lateral flow assay for colorimetric detection and quantification of methanol in alcoholic beverages.

In **Chapter 2**, experiments, analytical modelling, and numerical simulations were used to examine the concentration-dependent capillary imbibition of aqueous dye solutions in gel blot paper. A Brinkman-extended Darcy model was formulated to analytically characterize wicking dynamics. Experiments with four dye concentrations (0.2%, 0.5%, 1%, and 2% (w/v)) exhibited concentration-dependent wicking behavior, which was used to calculate fitting parameters and effective permeability. The findings indicate that increased dye concentrations diminish wicking length during the initial time intervals but gradually augment it in the subsequent phase, characterized by notable front-angle shifts

and asymmetric front progression at intermediate times. The analytical analysis facilitated the identification of the concentration-dependent permeability constant. Two separate regimes of permeability fluctuation with solute concentration were discovered, resulting from the competing interactions of particle-induced flow resistance and pore blockage-induced capillary pressure augmentation. Capillary pressure and permeability parameters, dependent on saturation, were experimentally obtained and fitted using the Brooks-Corey model which is integrated into Richards' equation for numerical simulations. The experimental and numerical results exhibited excellent agreement, suggesting the potential to develop paper-based microfluidics devices with species concentration-dependent flow with greater efficacy.

Chapter 3 introduces a cost-efficient technique for producing microscale droplets via a Y-shaped porous paper strip, therefore removing the necessity for external actuation. Experimental data indicated droplet splitting via pore-scale mechanisms, including elongation, snap-off, and merging, regulated by local saturation-dependent capillary pressure fluctuations. Grade 1 and Grade 4 papers have been used, wherein water wicking generates capillary forces which break down the oil phase into micro-sized droplets, which were studied using microscopy. The distribution of droplet sizes has been evaluated by varying the type of paper and the angle of the strip. In comparison to water alone, the water-oil system demonstrated increased capillary pressure at higher saturation levels, with Grade 1 paper consistently exhibiting larger pressure than Grade 4 owing to its finer pore structure. Droplet movement happened via merging and elongation mechanisms, while gravity decreased droplet size and enhanced homogeneity. Increasing the oil inlet reduced droplet size to approximately 357.5 μm at a width of 5 mm. Numerical phase-field simulations captured the droplet dynamics and were found to be consistent with Roof snap-off criteria. The numerical model accurately represented axial surface tension forces and pressure fields, while studies validated droplet stability and the effective encapsulation of polystyrene microparticles. This method offers a cost-effective means of generating micro-droplets for biological and chemical uses.

Chapter 4 investigates the combined effects of non-Newtonian fluid rheology and analyte entrapment on capillary-driven transport on gel blot paper through experimental, theoretical, and numerical methodologies. Aqueous NaCMC solutions and human blood have been taken as typical non-Newtonian fluids for the lateral flow test applications.

Richards' equation was employed with Brooks-Corey parameters in saturation-based flow modeling, and the predicted saturation fields closely aligned to the experimental data. Increasing the NaCMC concentration augmented the liquid entry pressure and decreased the pore size distribution index, signifying enhanced flow heterogeneity and suppressed wicking velocity. Raman spectroscopic analysis indicated that increasing the NaCMC concentrations enhance hydrogen bonding, resulting in enhanced bulk effective viscosity inside the paper matrix. Interestingly, the effective viscosity ratio has been determined to be less than unity at lower NaCMC concentrations at longer time instants. This is because the underlying flow experienced less viscous owing to the predominant shear-thinning nature and less hydroxyl groups at lower NaCMC concentration. Investigation on analyte entrapment revealed that diffusion and interception processes predominantly govern overall trapping efficiency, while inertial effects are insignificant. The diffusive Peclet number and overall trapping efficiency demonstrated a non-monotonic relationship with NaCMC concentrations, resulting in a reduction of the ideal test-line position as concentration increased. In blood, an increase in hematocrit diminished wicking velocity and augmented effective viscosity, whereas the ideal reaction site was identified using a criterion based on the critical Damköhler number.

In **Chapter 5**, a low-cost paper-based technique was developed for the colorimetric detection of methanol in alcohol-based beverages. Whatman™ Grade 1 paper was chosen as the substrate because of its delayed resistance to the corrosive properties of sulfuric acid. Colorimetric testing was conducted on samples with methanol concentrations of 5%, 10%, 15%, 20%, 25%, and 30% (v/v). Chemical reagents were dry stored on the paper strip, and an optimal placement area has been determined by numerical simulations. The diffusive Peclet number in the reaction zone was approximately one, signifying adequate residence time for efficient reaction. The test strip exhibited precise detection of methanol concentrations from 5% (v/v) to a dangerous threshold of 30% (v/v), including the documented lethal limit of about 8% (v/v). A colorimetric indexing chart was created to associate visual colour intensity with methanol concentration. Grayscale intensities were assessed utilizing ImageJ® and standardized against the 30% (v/v) methanol sample. Transient numerical simulations were performed at specific methanol concentrations to corroborate experimental findings. The established colorimetric index was subsequently validated by an evaluation of both branded and locally manufactured alcoholic beverages, affirming the accuracy of the demonstrated paper-based detection method.

Overall, this dissertation establishes an integrated understanding of how solute concentration, multiphase effects, fluid rheology, and reaction-transport coupling govern capillary-driven flow in paper-based porous media. The findings provide physically grounded design guidelines for optimizing paper microfluidic devices, particularly lateral flow assays, through controlled manipulation of permeability, saturation, viscosity, and residence time. By bridging pore-scale physics with device-level performance, this work contributes toward the rational design of next-generation paper-based diagnostic and sensing platforms.

6.2 SCOPE OF FUTURE WORK

While the present dissertation offers substantial insights into capillary-driven transport and reaction phenomena in paper-based porous media, several directions remain open for future investigation.

The natural next step of this research is to examine capillary-driven transport and diffusion of other biological fluids, including saliva, blood serum, and urine, within paper substrates, and to analyze their implications for biomarker detection. Investigating the impact of fluid-specific physicochemical parameters on diffusion, residence duration, and reaction efficiency could enhance the design and efficacy of paper-based diagnostic systems.

A further potential development of this research is to investigate droplet generation utilizing modified paper substrates to facilitate more controlled and reproducible droplet generation. By altering paper substrate properties like as pore structure, surface chemistry, or geometric design, enhanced droplet homogeneity and increased droplet generation rates may be attainable only through passive capillary mechanisms, eliminating the necessity for external actuation. Such research could further enhance paper-based systems for regulated multiphase microfluidic applications.

Another promising direction involves extending the present analyses to multistep reaction networks and multiplexed assays, where multiple reagents and reaction zones interact within the same paper device. Coupled modeling of sequential transport and reaction processes could aid in the rational design of complex paper-based diagnostic platforms.

Additionally, integrating the developed modeling frameworks with real-time image-based or smartphone-based readout systems could improve quantitative interpretation and field deployability of paper-based assays.

Together, these future directions can build upon the foundation established in this dissertation and advance the development of robust, predictive, and application-ready paper-based microfluidic systems.

REFERENCES

Abbasi, J., and Andersen, P. Ø. (2022). Theoretical comparison of two setups for capillary pressure measurement by centrifuge. *Heliyon*, **8**(9), e10656.

Ahmed, H., Khan, E. A., and Stokke, B. T. (2023). Microfluidic dual picoinjection based encapsulation of hemoglobin in alginate microcapsules reinforced by a poly(<scp>l</scp> -lysine)- *g* -poly(ethylene glycol). *Soft Matter*, **19**(1), 69–79.

Ai, Y., Xie, R., Xiong, J., and Liang, Q. (2020). Microfluidics for Biosynthesizing: from Droplets and Vesicles to Artificial Cells. *Small*, **16**(9), 1–24.

Aminpour, M., Galindo-Torres, S. A., Scheuermann, A., and Li, L. (2018). Pore-Scale Behavior of Darcy Flow in Static and Dynamic Porous Media. *Physical Review Applied*, **9**(6), 1–15.

Amiri Roodan, V., Gómez-Pastora, J., Karampelas, I. H., … Swihart, M. T. (2020). Formation and manipulation of ferrofluid droplets with magnetic fields in a microdevice: a numerical parametric study. *Soft Matter*, **16**(41), 9506–9518.

Armstrong, R. T., Berg, S., Dinariev, O., … Safonov, S. (2016). Modeling of Pore-Scale Two-Phase Phenomena Using Density Functional Hydrodynamics. *Transport in Porous Media*, **112**(3), 577–607.

Arun, R. K., Priyadarshini, N., Chaudhury, K., Chanda, N., Biswas, G., and Chakraborty, S. (2016). Paper-PDMS hybrid microchannel: A platform for rapid fluid-transport and mixing. *Journal of Micromechanics and Microengineering*, **26**(10).

Asadi, H., Pourjafar-Chelikdani, M., Khabazi, N. P., and Sadeghy, K. (2022). Quasi-steady imbibition of physiological liquids in paper-based microfluidic kits: Effect of shear-thinning. *Physics of Fluids*, **34**(12), 123111.

Avraam, D. G., and Payatakes, A. C. (1995). Flow regimes and relative permeabilities during steady-state two-phase flow in porous media. *Journal of Fluid Mechanics*, **293**(2), 207–236.

Ayappa, K. G., Davis, H. T., Davis, E. A., and Gordon, J. (1989). Capillary pressure: Centrifuge method revisited. *AIChE Journal*, **35**(3), 365–372.

Azizov, I., Dudek, M., and Øye, G. (2022). Studying droplet retention in porous media by novel microfluidic methods. *Chemical Engineering Science*, **248**, 117152.

Bachmann, J., Deurer, M., and Arye, G. (2007). Modeling Water Movement in Heterogeneous Water-Repellent Soil: 1. Development of a Contact Angle–Dependent Water-Retention Model. *Vadose Zone Journal*, **6**(3), 436–445.

Bai, F., He, X., Yang, X., Zhou, R., and Wang, C. (2017). Three dimensional phase-field investigation of droplet formation in microfluidic flow focusing devices with experimental validation. *International Journal of Multiphase Flow*, **93**, 130–141.

Bai, X., Yang, Q., Fang, Y., … Chen, F. (2020). Anisotropic, adhesion-switchable, and thermal-responsive superhydrophobicity on the femtosecond laser-structured shape-memory polymer for droplet manipulation. *Chemical Engineering Journal*, **400**, 125930.

Banerjee, U., Jain, S. K., and Sen, A. K. (2021). Particle encapsulation in aqueous ferrofluid drops and sorting of particle-encapsulating drops from empty drops using a magnetic field. *Soft Matter*, **17**(24), 6020–6028.

Bashirzadeh, Y., and Liu, A. P. (2019). Encapsulation of the cytoskeleton: towards mimicking the mechanics of a cell. *Soft Matter*, **15**(42), 8425–8436.

Behera, P. P. , Mehta, S. K., Arun, R. K. , and Mondal, P. K.. (2023a). Solute imbibition in paper strip: Pore-scale insights into the concentration-dependent permeability. *Physics of Fluids*, **35**(12), 122007.

Behera, P. P., Mehta, S. K., Agarwal, K., Bera, S., Arun, R. K., and Mondal, P. K.. (2024). Paper-based lateral flow assays: Prediction of methanol content in alcoholic beverages. *Physics of Fluids*, **36**(12), 123619.

Behera, P. P., Kumar, N., Kumari, M., Kumar, S., Mondal, P. K., and Arun, R. K. (2023b). Integrated microfluidic devices for point-of-care detection of bio-analytes and disease. *Sens. Diagn.*, **2**(6), 1437–1459.

Behera, P. P., Mehta, S. K., Arun, R. K., and Mondal, P. K. (2023c). Solute imbibition in paper strip: Pore-scale insights into the concentration-dependent permeability. *Physics of Fluids*, **35**(12).

Bewley, J. D., Bradford, K. J., Hilhorst, H. W. M., and Nonogaki, H. (2013). *Seeds: Physiology of Development, Germination and Dormancy*. *Seed Science Research*, Vol. 23, New York, NY: Springer New York.

Bindra, P., and Hazra, A. (2020). Dielectric Sensor System Using TiO2Nanotubes for Real-Time Detection of Methanol Contamination in Alcoholic Beverages. *IEEE Transactions on Instrumentation and Measurement*, **69**(9), 6621–6629.

Bishop, J. D., Hsieh, H. V., Gasperino, D. J., and Weigl, B. H. (2019). Sensitivity enhancement in lateral flow assays: A systems perspective. *Lab on a Chip*, **19**(15), 2486–2499.

Boccardo, G., Marchisio, D. L., and Sethi, R. (2014). Microscale simulation of particle

deposition in porous media. *Journal of Colloid and Interface Science*, **417**, 227–237.

Brandão, P. V, Ouarzazi, M. N., Hirata, S. C., and Barletta, A. (2021). Darcy–Carreau–Yasuda rheological model and onset of inelastic non-Newtonian mixed convection in porous media. *Physics of Fluids*, **33**(4), 44111.

Brentrup, G., Moawad, H. M. M., and Jain, H. (2008). Reduction of cracking in nano-macroporous bioactive glass. *Physics and Chemistry of Glasses: European Journal of Glass Science and Technology Part B*, **49**(6), 293–296.

Breugem, W.-P. (2007). The effective viscosity of a channel-type porous medium. *Physics of Fluids*, **19**(10).

Byrnes, S., Thiessen, G., and Fu, E. (2013). Progress in The Development of Paper-Based Diagnostics for Low-Resource Point-Of-Care Settings. *Bioanalysis*, **5**(22), 2821–2836.

Cahn, J. W., and Hilliard, J. E. (1958). Free Energy of a Nonuniform System. I. Interfacial Free Energy. *The Journal of Chemical Physics*, **28**(2), 258–267.

Cahn, J. W., and Hilliard, J. E. (1959). Free Energy of a Nonuniform System. III. Nucleation in a Two-Component Incompressible Fluid. *The Journal of Chemical Physics*, **31**(3), 688–699.

Cai, Y., Sun, R., Ren, Y., and Gou, Y. (2025). Development of droplet-based microfluidics in generation, manipulation and biomedical application. *Microchemical Journal*, **211**, 113101.

Cate, D. M., Adkins, J. A., Mettakoonpitak, J., and Henry, C. S. (2015). Recent Developments in Paper-Based Micro fl uidic Devices.

Chami Khazraji, A., and Robert, S. (2013a). Interaction Effects between Cellulose and Water in Nanocrystalline and Amorphous Regions: A Novel Approach Using Molecular Modeling. *Journal of Nanomaterials*, **2013**(1), 409676.

Chami Khazraji, A., and Robert, S. (2013b). Self-Assembly and Intermolecular Forces When Cellulose and Water Interact Using Molecular Modeling. *Journal of Nanomaterials*, **2013**(1), 745979.

Chang, H. Y., Tsao, H. K., and Sheng, Y. J. (2023). Abnormal wicking dynamics of total wetting ethanol in graphene nanochannels. *Physics of Fluids*, **35**(5).

Chang, S., and Kim, W. (2020). Dynamics of water imbibition through paper with swelling. *Journal of Fluid Mechanics*, **892**.

Charapitsa, S., Sytova, S., Kavalenka, A., … Kolesnov, A. (2021). The Method for Direct Gas Chromatographic Determination of Acetaldehyde, Methanol, and Other Volatiles

Using Ethanol as a Reference Substance: Application for a Wide Range of Alcoholic Beverages. *Food Analytical Methods*, **14**(10), 2088–2100.

Chowdhury, M. S., Zheng, W., Singh, A. K., … Haag, R. (2021). Linear triglycerol-based fluorosurfactants show high potential for droplet-microfluidics-based biochemical assays. *Soft Matter*, **17**(31), 7260–7267.

Comiti, J., Sabiri, N. E., and Montillet, A. (2000). Experimental characterization of flow regimes in various porous media — III: limit of Darcy's or creeping flow regime for Newtonian and purely viscous non-Newtonian fluids. *Chemical Engineering Science*, **55**(15), 3057–3061.

Cun, D., Zhang, C., Bera, H., and Yang, M. (2021). Particle engineering principles and technologies for pharmaceutical biologics. *Advanced Drug Delivery Reviews*, **174**, 140–167.

da Costa Sousa, M. G., Vignolo, S. M., Franca, C. M., … Bertassoni, L. E. (2024). Engineering models of head and neck and oral cancers on-a-chip. *Biomicrofluidics*, **18**(2), 21502.

Das, S., Patel, H. V., Milacic, E., Deen, N. G., and Kuipers, J. A. M. (2018). Droplet spreading and capillary imbibition in a porous medium: A coupled IB-VOF method based numerical study. *Physics of Fluids*, **30**(1).

De Jonghe, J., Kaminski, T. S., Morse, D. B., … Hollfelder, F. (2023). spinDrop: a droplet microfluidic platform to maximise single-cell sequencing information content. *Nature Communications*, **14**(1), 4788.

de Oliveira, R. A. G., Camargo, F., Pesquero, N. C., and Faria, R. C. (2017). A simple method to produce 2D and 3D microfluidic paper-based analytical devices for clinical analysis. *Analytica Chimica Acta*, **957**, 40–46.

Dharmaraja, S., Lafleur, L., Byrnes, S., … Lutz, B. (2013). Programming paper networks for point of care diagnostics. In *Proc.SPIE*, Vol. 8615, p. 86150X.

Dimitrov, D. I., Milchev, A., and Binder, K. (2007). Capillary Rise in Nanopores: Molecular Dynamics Evidence for the Lucas-Washburn Equation. *Phys. Rev. Lett.*, **99**(5), 54501.

Ding, M., Zhang, T., Zhang, H., Tao, N., Wang, X., and Zhong, J. (2020). Gelatin-stabilized traditional emulsions: Emulsion forms, droplets, and storage stability. *Food Science and Human Wellness*, **9**(4), 320–327.

Douglas Ruth; Sidney Wong. (1991). Calculation Of Capillary-pressure Curves From Data Obtained By The Centrifuge Method.

Dungchai, W., Chailapakul, O., and Henry, C. S. (2011). A low-cost, simple, and rapid fabrication method for paper-based microfluidics using wax screen-printing. *Analyst*, **136**(1), 77–82.

Eberhard, U., Seybold, H. J., Floriancic, M., … Holzner, M. (2019). Determination of the effective viscosity of non-Newtonian fluids flowing through porous media. *Frontiers in Physics*, **7**(MAY), 1–9.

Elizalde, E., Urteaga, R., and Berli, C. L. A. (2015). Rational design of capillary-driven flows for paper-based microfluidics. *Lab Chip*, **15**(10), 2173–2180.

Elizalde, E., Urteaga, R., and Berli, C. L. A. (2016). Precise capillary flow for paper-based viscometry. *Microfluidics and Nanofluidics*, **20**(10), 135.

Elrahmani, A., Al-Raoush, R. I., and Seers, T. D. (2023). Clogging and permeability reduction dynamics in porous media: A numerical simulation study. *Powder Technology*, **427**(January), 118736.

Erol, S., Fowler, S. J., Harcouët-Menou, V., and Laenen, B. (2017). An Analytical Model of Porosity–Permeability for Porous and Fractured Media. *Transport in Porous Media*, **120**(2), 327–358.

Fagnani, E. (2003). Chromotropic acid–formaldehyde reaction in strongly acidic media. The role of dissolved oxygen and replacement of concentrated sulphuric acid. *Talanta*, **60**(1), 171–176.

Fan, D., Chapman, E., Khan, A., … Striolo, A. (2022). Anomalous transport of colloids in heterogeneous porous media: A multi-scale statistical theory. *Journal of Colloid and Interface Science*, **617**, 94–105.

Farthing, M. W., and Ogden, F. L. (2017). Numerical Solution of Richards' Equation: A Review of Advances and Challenges. *Soil Science Society of America Journal*, **81**(6), 1257–1269.

Feng, Q., Cha, L., Dai, C., Zhao, G., and Wang, S. (2020). Effect of particle size and concentration on the migration behavior in porous media by coupling computational fluid dynamics and discrete element method. *Powder Technology*, **360**, 704–714.

Flow, T. H. E., Through, L., and Capillary, L. T. (1905). The flow, **50**(30).

FSSAI. (2021). Food Safety and Standards (Alcoholic Beverages) Regulations, 2018. The Gazette of India, Version-1, 1–16.

Fu, E., and Downs, C. (2017). Progress in the development and integration of fluid flow control tools in paper microfluidics. *Lab on a Chip*, **17**(4), 614–628.

Fu, E., Liang, T., Spicar-Mihalic, P., Houghtaling, J., Ramachandran, S., and Yager, P.

(2012). Two-Dimensional Paper Network Format That Enables Simple Multistep Assays for Use in Low-Resource Settings in the Context of Malaria Antigen Detection. *Analytical Chemistry*, **84**(10), 4574–4579.

Fu, E., Lutz, B., Kauffman, P., and Yager, P. (2010). Controlled reagent transport in disposable 2D paper networks. *Lab on a Chip*, **10**(7), 918–920.

Gaikwad, H. S., Mondal, P. K., and Wongwises, S. (2017a). Non-linear drag induced entropy generation analysis in a microporous channel: The effect of conjugate heat transfer. *International Journal of Heat and Mass Transfer*, **108**, 2217–2228.

Gaikwad, H. S., Mondal, P. K., and Wongwises, S. (2017b). Non-linear drag induced entropy generation analysis in a microporous channel: The effect of conjugate heat transfer. *International Journal of Heat and Mass Transfer*, **108**, 2217–2228.

Garstecki, P., Fuerstman, M. J., Stone, H. A., and Whitesides, G. M. (2006). Formation of droplets and bubbles in a microfluidic T-junction—scaling and mechanism of break-up. *Lab on a Chip*, **6**(3), 437.

Gasperino, D., Baughman, T., Hsieh, H. V., Bell, D., and Weigl, B. H. (2018a). Improving Lateral Flow Assay Performance Using Computational Modeling. *Annual Review of Analytical Chemistry*, **11**, 219–244.

Gasperino, D., Baughman, T., Hsieh, H. V, Bell, D., and Weigl, B. H. (2018b). Improving Lateral Flow Assay Performance Using Computational Modeling. *Annual Review of Analytical Chemistry*, **11**(Volume 11, 2018), 219–244.

Genuchten, V. A. N. (1980). A Closed-form Equation for Predicting the Hydraulic Conductivity of Unsaturated Soils 1. *Soil Science Society of America Journal*, **44**, 892–898.

Gillespie, T. (1959). The capillary rise of a liquid in a vertical strip of filter paper. *Journal of Colloid Science*, **14**(2), 123–130.

Ginzburg, I., Silva, G., and Talon, L. (2015). Analysis and improvement of Brinkman lattice Boltzmann schemes: Bulk, boundary, interface. Similarity and distinctness with finite elements in heterogeneous porous media. *Phys. Rev. E*, **91**(2), 23307.

Gisladottir, S., Loftsson, T., and Stefansson, E. (2009). Diffusion characteristics of vitreous humour and saline solution follow the Stokes Einstein equation. *Graefe's Archive for Clinical and Experimental Ophthalmology*, **247**(12), 1677–1684.

Gong, M. M., and Sinton, D. (2017). Turning the Page: Advancing Paper-Based Microfluidics for Broad Diagnostic Application. *Chemical Reviews*, **117**(12), 8447–8480.

Gorthi, S. R., Meher, S. K., Biswas, G., and Mondal, P. K. (2020). Capillary imbibition of non-Newtonian fluids in a microfluidic channel: analysis and experiments. *Proceedings of the Royal Society A: Mathematical, Physical and Engineering Sciences*, **476**(2242), 13663–13667.

Goudappel, G. J. W., van Duynhoven, J. P. M., and Mooren, M. M. W. (2001). Measurement of Oil Droplet Size Distributions in Food Oil/Water Emulsions by Time Domain Pulsed Field Gradient NMR. *Journal of Colloid and Interface Science*, **239**(2), 535–542.

Greenspan, P., Mayer, E. P., and Fowler, S. D. (1985). Nile red: A selective fluorescent stain for intracellular lipid droplets. *Journal of Cell Biology*, **100**(3), 965–973.

H., B. R., and T., C. A. (1966). Properties of Porous Media Affecting Fluid Flow. *Journal of the Irrigation and Drainage Division*, **92**(2), 61–88.

Hao, L., and Cheng, P. (2010). Pore-scale simulations on relative permeabilities of porous media by lattice Boltzmann method. *International Journal of Heat and Mass Transfer*, **53**(9–10), 1908–1913.

Hassler, G. L., and Brunner, E. (1945). Measurement of Capillary Pressures in Small Core Samples. *Transactions of the AIME*, **160**(01), 114–123.

He, G. Y., Tsao, H. K., and Sheng, Y. J. (2022). Wicking dynamics into two-rail open channel with periodical branches. *Physics of Fluids*, **34**(10).

Heiranian, M., and Aluru, N. R. (2022). Modified Lucas-Washburn theory for fluid filling in nanotubes. *Phys. Rev. E*, **105**(5), 55105.

Helton, K. L., and Yager, P. (2007). Interfacial instabilities affect microfluidic extraction of small molecules from non-Newtonian fluids. *Lab Chip*, **7**(11), 1581–1588.

Hommel, J., Coltman, E., and Class, H. (2018). Porosity–Permeability Relations for Evolving Pore Space: A Review with a Focus on (Bio-)geochemically Altered Porous Media. *Transport in Porous Media*, **124**(2), 589–629.

Hsu, C. T., and Cheng, P. (1990). Thermal dispersion in a porous medium. *International Journal of Heat and Mass Transfer*, **33**(8), 1587–1597.

Hu, J., Wang, S., Wang, L., … Xu, F. (2014). Advances in paper-based point-of-care diagnostics. *Biosensors and Bioelectronics*, **54**, 585–597.

Hu, Y., Li, D., Shu, S., and Niu, X. (2016). Finite-volume method with lattice Boltzmann flux scheme for incompressible porous media flow at the representative-elementary-volume scale. *Phys. Rev. E*, **93**(2), 23308.

Jamshidi, F., Kunz, W., Altschuh, P., … Nestler, B. (2022). Geometric flow control in

lateral flow assays: Macroscopic single-phase modeling. *Physics of Fluids*, **34**(6).

Jang, H. K., Oh, Y., and Hwang, W. R. (2025). A Unified Method for the Mobility Prediction of an Inelastic Non-Newtonian Fluid Through Complex Porous Media. *Transport in Porous Media*, **152**(1), 1–22.

Jena, S. K., Srivastava, T., Bahga, S. S., and Kondaraju, S. (2023). Effect of channel width on droplet generation inside T-junction microchannel. *Physics of Fluids*, **35**(2), 22107.

Jin, C., and Sengupta, A. (2024). Microbes in porous environments: from active interactions to emergent feedback. *Biophysical Reviews*, **16**(2), 173–188.

Joensson, H. N., and Andersson Svahn, H. (2012). Droplet Microfluidics—A Tool for Single-Cell Analysis. *Angewandte Chemie International Edition*, **51**(49), 12176–12192.

Kaneelil, P. R., de Souza, J. P., Turk, G., Pahlavan, A. A., and Stone, H. A. (2024). Electrically mediated self-assembly and manipulation of drops at an interface. *Soft Matter*, **20**(27), 5417–5424.

Kim, J., Moon, M. W., and Kim, H. Y. (2020). Capillary rise in superhydrophilic rough channels. *Physics of Fluids*, **32**(3).

Kim, S., and Cho, Y. I. (2003). The effect of dye concentration on the viscosity of water in a scanning capillary-tube viscometer. *Journal of Non-Newtonian Fluid Mechanics*, **111**(1), 63–68.

Kim, S. J., Choi, J. W., Moon, M.-W., … Kim, H.-Y. (2015). Wicking and flooding of liquids on vertical porous sheets. *Physics of Fluids*, **27**(3).

Kumar, S., Bhushan, P., and Bhattacharya, S. (2016). Development of a paper-based analytical device for colorimetric detection of uric acid using gold nanoparticles-graphene oxide (AuNPs-GO) conjugates. *Analytical Methods*, **8**(38), 6965–6973.

Kumar, S., Bhushan, P., and Bhattacharya, S. (2019). Fluid Transport Mechanisms in Paper-Based Microfluidic Devices BT - Paper Microfluidics: Theory and Applications. In S. Bhattacharya, S. Kumar, and A. K. Agarwal, eds., , Singapore: Springer Singapore, pp. 7–28.

Kumari, M., Kumar, N., Kumar, S., Gandhi, S., Zussman, E., and Arun, R. K. (2024). A paper-based point-of-care device for the detection of cysteine using gold nanoparticles from whole blood. *Analytical Methods*, **16**(19), 3007–3019.

Kuznetsov, A. V. (1998). Analytical Study of Fluid Flow and Heat Transfer during Forced Convection in a Composite Channel Partly Filled with a Brinkman – Forchheimer Porous Medium, **0**, 173–192.

Lagus, T. P., and Edd, J. F. (2013). A review of the theory, methods and recent applications of high-throughput single-cell droplet microfluidics. *Journal of Physics D: Applied Physics*, **46**(11), 114005.

Latha, M., Aruna-Devi, R., Bogireddy, N. K. R., … Agarwal, V. (2020). N-doped oxidized carbon dots for methanol sensing in alcoholic beverages. *RSC Advances*, **10**(38), 22522–22532.

Lathia, R., Nampoothiri, K. N., Sagar, N., Bansal, S., Modak, C. D., and Sen, P. (2023). Advances in Microscale Droplet Generation and Manipulation. *Langmuir*, **39**(7), 2461–2482.

Lee, M., Kim, S., Kim, H. Y., and Mahadevan, L. (2016). Bending and buckling of wet paper. *Physics of Fluids*, **28**(4).

Leung, K., Zahn, H., Leaver, T., … Hansen, C. L. (2012). A programmable droplet-based microfluidic device applied to multiparameter analysis of single microbes and microbial communities. *Proceedings of the National Academy of Sciences of the United States of America*, **109**(20), 7665–7670.

Li, B., Yu, L., Qi, J., Fu, L., Zhang, P., and Chen, L. (2017). Controlling Capillary-Driven Fluid Transport in Paper-Based Microfluidic Devices Using a Movable Valve. *Analytical Chemistry*, **89**(11), 5707–5712.

Li, K. (2010). Analytical derivation of Brooks–Corey type capillary pressure models using fractal geometry and evaluation of rock heterogeneity. *Journal of Petroleum Science and Engineering*, **73**(1–2), 20–26.

Li, M., Liu, H., Zhuang, S., and Goda, K. (2021). Droplet flow cytometry for single-cell analysis. *RSC Advances*, **11**(34), 20944–20960.

Li, S., Liu, M., Hanaor, D., and Gan, Y. (2018). Dynamics of Viscous Entrapped Saturated Zones in Partially Wetted Porous Media. *Transport in Porous Media*, **125**(2), 193–210.

Liang, N., Jiao, Z., Zhang, C., … Chen, Q. (2023). Mature Red Blood Cells Contain Long DNA Fragments and Could Acquire DNA from Lung Cancer Tissue, **2206361**, 1–12.

Lioumbas, J. S., Zamanis, A., and Karapantsios, T. D. (2013). Towards a wicking rapid test for rejection assessment of reused fried oils: Results and analysis for extra virgin olive oil. *Journal of Food Engineering*, **119**(2), 260–270.

Liu, H., Valocchi, A. J., Zhang, Y., and Kang, Q. (2013). Phase-field-based lattice Boltzmann finite-difference model for simulating thermocapillary flows. *Phys. Rev. E*, **87**(1), 13010.

Liu, Z., Hu, J., Zhao, Y., Qu, Z., and Xu, F. (2015). Experimental and numerical studies on liquid wicking into filter papers for paper-based diagnostics. *Applied Thermal Engineering*, **88**(June 2018), 280–287.

Long, Y., Li, Y., Cao, R., … Nie, Y. (2024). Molecular insight into the dissolution-degradation process of cellulose bunch in ionic liquids. *Journal of Molecular Liquids*, **414**, 126191.

Lopez, C. G., Rogers, S. E., Colby, R. H., Graham, P., and Cabral, J. T. (2015). Structure of sodium carboxymethyl cellulose aqueous solutions: A SANS and rheology study. *Journal of Polymer Science Part B: Polymer Physics*, **53**(7), 492–501.

Lota, G., Krawczyk, P., Lota, K., … Buchwald, T. (2016). The application of activated carbon modified by ozone treatment for energy storage. *Journal of Solid State Electrochemistry*, **20**(10), 2857–2864.

Louf, J. F., Zheng, Y., Kumar, A., … Jensen, K. H. (2018). Imbibition in plant seeds. *Physical Review E*, **98**(4), 1–5.

Lu, C., Zhao, W., Liu, Y., and Dong, X. (2018). Pore-Scale Transport Mechanisms and Macroscopic Displacement Effects of In-Situ Oil-in-Water Emulsions in Porous Media. *Journal of Solar Energy Engineering, Transactions of the ASME*, **140**(10), 1–8.

Lutz, B., Liang, T., Fu, E., Ramachandran, S., Kauffman, P., and Yager, P. (2013). Dissolvable fluidic time delays for programming multi-step assays in instrument-free paper diagnostics. *Lab on a Chip*, **13**(14), 2840–2847.

Lyubimova, T. P., Lyubimov, D. V, Baydina, D. T., Kolchanova, E. A., and Tsiberkin, K. B. (2016). Instability of plane-parallel flow of incompressible liquid over a saturated porous medium. *Physical Review E*, **94**(1), 13104.

Macedo, P. B., and Litovitz, T. A. (1965). On the relative roles of free volume and activation energy in the viscosity of liquids. *The Journal of Chemical Physics*, **42**(1), 245–256.

Mahmoudi, T., de la Guardia, M., Shirdel, B., Mokhtarzadeh, A., and Baradaran, B. (2019). Recent advancements in structural improvements of lateral flow assays towards point-of-care testing. *TrAC - Trends in Analytical Chemistry*, **116**, 13–30.

Makarem, M., Lee, C. M., Kafle, K., … Kim, S. H. (2019). *Probing cellulose structures with vibrational spectroscopy*. *Cellulose*, Vol. 26, Springer Netherlands.

Malik, L., Nandy, S., Satpathi, N. S., Ghosh, D., Laurell, T., and Sen, A. K. (2024). Ultrasound reforms droplets. *Lab Chip*, **24**(19), 4649–4658.

Maré, E., and Woudberg, S. (2023). A Comparative Study of Geometric Models for Predicting Permeability Coefficients and Specific Surface Areas of Fibrous Porous Media. *Transport in Porous Media*, **148**(2), 383–416.

Martinez, A. W., Phillips, S. T., Butte, M. J., and Whitesides, G. M. (2007). Patterned Paper as a Platform for Inexpensive, Low-Volume, Portable Bioassays. *Angewandte Chemie*, **119**(8), 1340–1342.

Masoodi, R., and Pillai, K. M. (2010a). Darcy's law-based model for wicking in paper-like swelling porous media. *AIChE Journal*, **56**(9), 2257–2267.

Masoodi, R., and Pillai, K. M. (2010b). Darcy's law-based model for wicking in paper-like swelling porous media. *AIChE Journal*, **59**(4), NA-NA.

Mastiani, M., Firoozi, N., Petrozzi, N., Seo, S., and Kim, M. (2019). Polymer-Salt Aqueous Two-Phase System (ATPS) Micro-Droplets for Cell Encapsulation. *Scientific Reports*, **9**(1), 15561.

Matuła, K., Rivello, F., and Huck, W. T. S. (2020). Single-Cell Analysis Using Droplet Microfluidics. *Advanced Biosystems*, **4**(1), 1900188.

McClure, J. E., Berg, S., and Armstrong, R. T. (2020). Capillary fluctuations and energy dynamics for flow in porous media. *Physics of Fluids*, **33**(8). doi:10.1063/5.0057428

Mehrabian, H., Gao, P., and Feng, J. J. (2011). Wicking flow through microchannels. *Physics of Fluids*, **23**(12).

Mehri, R., Mavriplis, C., and Fenech, M. (2018). Red blood cell aggregates and their effect on non-Newtonian blood viscosity at low hematocrit in a two-fluid low shear rate microfluidic system. *PLoS ONE*, **13**(7).

Mehta, S. K., Kumar, S., Shen, A. Q., and Mondal, P. K. (2025). Paper-based microfluidics: Analyte-driven imbibition under the lens. *Biomicrofluidics*, **19**(3), 34104.

Meier, R. J., Csisza, A., and Klumpp, E. (2006). On the Interpretation of the 1100 cm - 1 Raman Band in Phospholipids and Other Alkyl-Containing Molecular Entities, 5842–5844.

Meissner, M., Dong, J., Eggers, J., Seddon, A. M., and Royall, C. P. (2017). Oil-in-water microfluidics on the colloidal scale: new routes to self-assembly and glassy packings. *Soft Matter*, **13**(4), 788–794.

Mendez, S., Fenton, E. M., Gallegos, G. R., … López, G. P. (2010). Imbibition in Porous Membranes of Complex Shape: Quasi-stationary Flow in Thin Rectangular Segments. *Langmuir*, **26**(2), 1380–1385.

Michelin, S. (2023). Self-Propulsion of Chemically Active Droplets. *Annual Review of*

Fluid Mechanics, **55**(1), 77–101.

Miller, C. C., and Walker, J. (1997). The Stokes-Einstein law for diffusion in solution. *Proceedings of the Royal Society of London. Series A, Containing Papers of a Mathematical and Physical Character*, **106**(740), 724–749.

Moelans, N., Blanpain, B., and Wollants, P. (2008). An introduction to phase-field modeling of microstructure evolution. *Calphad*, **32**(2), 268–294.

Mondal, P. K., DasGupta, D., Bandopadhyay, A., Ghosh, U., and Chakraborty, S. (2015a). Contact line dynamics of electroosmotic flows of incompressible binary fluid system with density and viscosity contrasts. *Physics of Fluids*, **27**(3), 32109.

Mondal, P. K., DasGupta, D., and Chakraborty, S. (2015b). Rheology-modulated contact line dynamics of an immiscible binary system under electrical double layer phenomena. *Soft Matter*, **11**(33), 6692–6702.

Morita, S., Tanaka, M., and Ozaki, Y. (2007). Time-Resolved In Situ ATR-IR Observations of the Process of Sorption of Water into a Poly (2-methoxyethyl acrylate) Film, (12), 3750–3761.

Multiphysics, C. (1998). Introduction to comsol multiphysics®. *COMSOL Multiphysics, Burlington, MA, Accessed Feb*, **9**(2018), 32.

Nabovati, A., Llewellin, E. W., and Sousa, A. C. M. (2009). A general model for the permeability of fibrous porous media based on fluid flow simulations using the lattice Boltzmann method. *Composites Part A: Applied Science and Manufacturing*, **40**(6–7), 860–869.

Nakai, R. (2020). Size Matters: Ultra-small and Filterable Microorganisms in the Environment. *Microbes and Environments*, **35**(2).

Nalumachu, R., Anandita, A., and Rath, D. (2023). Computational modelling of a competitive immunoassay in lateral flow diagnostic devices. *Sens. Diagn.*, **2**(3), 687–698.

Narayanamurthy, V., Jeroish, Z. E., Bhuvaneshwari, K. S., … Yusoff, M. M. (2020). Advances in passively driven microfluidics and lab-on-chip devices: A comprehensive literature review and patent analysis. *RSC Advances*, **10**(20), 11652–11680.

Nelson, K. E., and Ginn, T. R. (2005). Colloid Filtration Theory and the Happel Sphere-in-Cell Model Revisited with Direct Numerical Simulation of Colloids. *Langmuir*, **21**(6), 2173–2184.

Ngom, B., Guo, Y., Wang, X., and Bi, D. (2010). Development and application of lateral

flow test strip technology for detection of infectious agents and chemical contaminants: a review. *Analytical and Bioanalytical Chemistry*, **397**(3), 1113–1135.

Noh, H., and Phillips, S. T. (2010). Fluidic Timers for Time-Dependent, Point-of-Care Assays on Paper. *Analytical Chemistry*, **82**(19), 8071–8078.

Norouzi Darabad, M., Singha, S., Vanapalli, S. A., Vaughn, M. W., and Blawzdziewicz, J. (2024). Capillary imbibition of confined monodisperse emulsions in microfluidic channels. *Soft Matter*, **20**(22), 4337–4357.

Oh, Y. K., Joung, H.-A., Han, H. S., Suk, H.-J., and Kim, M.-G. (2014). A three-line lateral flow assay strip for the measurement of C-reactive protein covering a broad physiological concentration range in human sera. *Biosensors and Bioelectronics*, **61**, 285–289.

Paine, A. J. (2001). Defining a tolerable concentration of methanol in alcoholic drinks. *Human and Experimental Toxicology*, **20**(11), 563–568.

Palit, S., Khajehpour Tadavani, S., and Yethiraj, A. (2018). Realization of a stable, monodisperse water-in-oil droplet system with micro-scale and nano-scale confinement for tandem microscopy and diffusion NMR studies. *Soft Matter*, **14**(3), 448–459.

Patari, S., Chowdhury, I. U., Kumar, J., and Mahapatra, P. S. (2023). Dynamics of liquid flow through fabric porous media: Experimental, analytical, and numerical investigation. *Physics of Fluids*, **35**(10).

Patari, S., and Mahapatra, P. S. (2020a). Liquid Wicking in a Paper Strip: An Experimental and Numerical Study. *ACS Omega*, **5**(36), 22931–22939.

Patari, S., and Mahapatra, P. S. (2020b). Liquid Wicking in a Paper Strip: An Experimental and Numerical Study. *ACS Omega*, **5**(36), 22931–22939.

Patel, P., Tonog, P., and Lakhkar, A. D. (2002). Normal Saline. Reactions Weekly, **909**, 13.

Paul, A., Pal, A. K., Wang, A.-B., and Biswas, G. (2024). Splashing impact of a falling liquid drop. *Physics of Fluids*, **36**(9), 92129.

Payen, Julien, Vroman, Philippe, Lewandowski, Maryline, Perwuelz, Anne, Callé-Chazelet, Sandrine, and Thomas, Dominique. (2012). Influence of fiber diameter, fiber combinations and solid volume fraction on air filtration properties in nonwovens. *Textile Research Journal*, **82**(19), 1948–1959.

Pazdniakou, A., and Adler, P. M. (2013). Dynamic permeability of porous media by the lattice Boltzmann method. *Advances in Water Resources*, **62**, 292–302.

Pearson, J. R. A., and Tardy, P. M. J. (2002). Models for flow of non-Newtonian and complex fluids through porous media. *Journal of Non-Newtonian Fluid Mechanics*, **102**(2), 447–473.

Peng, R., and Li, D. (2016). Electroosmotic flow in single PDMS nanochannels. *Nanoscale*, **8**(24), 12237–12246.

Perez-Cruz, A., Stiharu, I., and Dominguez-Gonzalez, A. (2017a). Two-dimensional model of imbibition into paper-based networks using Richards' equation. *Microfluidics and Nanofluidics*, **21**(5), 98.

Perez-Cruz, A., Stiharu, I., and Dominguez-Gonzalez, A. (2017b). Two-dimensional model of imbibition into paper-based networks using Richards' equation. *Microfluidics and Nanofluidics*, **21**(5), 98.

Piacentini, E., Drioli, E., and Giorno, L. (2014). Membrane emulsification technology: Twenty-five years of inventions and research through patent survey. *Journal of Membrane Science*, **468**, 410–422.

Pismen, L. M., and Pomeau, Y. (2000). Disjoining potential and spreading of thin liquid layers in the diffuse-interface model coupled to hydrodynamics. *Phys. Rev. E*, **62**(2), 2480–2492.

Pivonka, P., and Smith, D. (2005). Investigation of nanoscale electrohydrodynamic transport phenomena in charged porous materials. *International Journal for Numerical Methods in Engineering*, **63**(14), 1975–1990.

Postek, W., and Garstecki, P. (2022). Droplet Microfluidics for High-Throughput Analysis of Antibiotic Susceptibility in Bacterial Cells and Populations. *Accounts of Chemical Research*, **55**(5), 605–615.

Pradela-Filho, L. A., Veloso, W. B., Arantes, I. V. S., … Paixão, T. R. L. C. (2023). Paper-based analytical devices for point-of-need applications. *Microchimica Acta*, **190**(5).

Qian, S., and Bau, H. H. (2003). A mathematical model of lateral flow bioreactions applied to sandwich assays. *Analytical Biochemistry*, **322**(1), 89–98.

Ragavendar, M. S., and Anmol, C. M. (2012). A mathematical model to predict the optimal test line location and sample volume for lateral flow immunoassays. *Proceedings of the Annual International Conference of the IEEE Engineering in Medicine and Biology Society, EMBS*, 2408–2411.

Rakszewska, A., Tel, J., Chokkalingam, V., and Huck, W. T. S. (2014). One drop at a time: toward droplet microfluidics as a versatile tool for single-cell analysis. *NPG Asia Materials*, **6**(10), e133–e133.

Ram, R. (ऋषि राम), Kumar, D. (धर्मेन्द्र कुमार), Paik, P. (प्रदीप पैक), and Sarkar, A. (अर्नब सरकार). (2023). A simple and low-cost paper-based device for simultaneous determination of hematocrit and hemoglobin levels in point-of-care settings. *Physics of Fluids*, **35**(12), 122006.

Ramos, G., Cordero, M. L., and Soto, R. (2020). Bacteria driving droplets. *Soft Matter*, **16**(5), 1359–1365.

Ranny, M. (1965). The determination of methanol by oxidation to formaldehyde and polarographic reduction. *The Analyst*, **90**(1076), 664–673.

Rath, D., and Panda, S. (2019). Modeling the transport and capture of analytes in a two-phase heterogeneous microfluidic immunosensor. *Chemical Engineering Research and Design*, **141**, 272–278.

Rath, D., Sathishkumar, N., and Toley, B. J. (2018a). Experimental Measurement of Parameters Governing Flow Rates and Partial Saturation in Paper-Based Microfluidic Devices. *Langmuir : The ACS Journal of Surfaces and Colloids*, **34**(30), 8758–8766.

Rath, D., Sathishkumar, N., and Toley, B. J. (2018b). Experimental Measurement of Parameters Governing Flow Rates and Partial Saturation in Paper-Based Microfluidic Devices. *Langmuir*, **34**(30), 8758–8766.

Rath, D., Sathishkumar, N., and Toley, B. J. (2018c). Experimental Measurement of Parameters Governing Flow Rates and Partial Saturation in Paper-Based Microfluidic Devices. *Langmuir*, **34**(30), 8758–8766.

Rath, D., Sathishkumar, N., and Toley, B. J. (2018d). Experimental Measurement of Parameters Governing Flow Rates and Partial Saturation in Paper-Based Microfluidic Devices. *Langmuir*, **34**(30), 8758–8766.

Rath, D., and Toley, B. J. (2021). Modeling-Guided Design of Paper Microfluidic Networks: A Case Study of Sequential Fluid Delivery. *ACS Sensors*, **6**(1), 91–99.

Ray, B., Biswas, G., and Sharma, A. (2010). Generation of secondary droplets in coalescence of a drop at a liquid-liquid interface. *Journal of Fluid Mechanics*, **655**, 72–104.

Rhodes, F. H., and Barbour, C. B. (1923). The Viscosities of Mixtures of Sulfuric Acid and Water. *Industrial and Engineering Chemistry*, **15**(8), 850–852.

Rodriguez, E., Giacomelli, F., and Vazquez, A. (2004). Permeability-Porosity Relationship in RTM for Different Fiberglass and Natural Reinforcements. *Journal of Composite Materials*, **38**(3), 259–268.

Roof, J. G. (1970). Snap-Off of Oil Droplets in Water-Wet Pores. *Society of Petroleum Engineers Journal*, **10**(01), 85–90.

Roy, S., Das, S., Ray, A., and Parui, P. P. (2021). Fluorometric trace methanol detection in ethanol and isopropanol in a water medium for application in alcoholic beverages and hand sanitizers. *RSC Advances*, **11**(48), 30093–30101.

Saadat, F., and Rafizadeh, A. (2019). Rapid determination of methanol in herbaceous distillates for their safety evaluation by a new modified chromotropic acid method. *Iranian Journal of Pharmaceutical Research*, **18**(2), 696–703.

Sajid, M., Kawde, A. N., and Daud, M. (2015). Designs, formats and applications of lateral flow assay: A literature review. *Journal of Saudi Chemical Society*, **19**(6), 689–705.

Satpathi, N. S., Malik, L., Nandy, S., Sujith, T., Yeo, L. Y., and Sen, A. K. (2024). Surfing droplets on nanoscopic films driven by surface acoustic waves. *Physical Review E*, **110**(6), 65108.

Schneider, C. A., Rasband, W. S., and Eliceiri, K. W. (2012). NIH Image to ImageJ: 25 years of Image Analysis HHS Public Access. *Nat Methods*, **9**(7), 671–675.

Schwarz, W. H. (1987). The Rheology of Saliva. *Journal of Dental Research*, **66**(2_suppl), 660–666.

Sengupta, A., Dhar, J., Danza, F., Ghoshal, A., Müller, S., and Kakavand, N. (2022). Active reconfiguration of cytoplasmic lipid droplets governs migration of nutrient-limited phytoplankton. *Science Advances*, **8**(44).

Shah, S. K., Chatterjee, S. K., and Bhattarai, A. (2016). Effect of Methanol on Viscosity of Aqueous Solutions of Cationic Surfactants at 298.15 to 323.15 K. *Journal of Chemistry*, **2016**(1).

Sharratt, W. N., Brooker, A., Robles, E. S. J., and Cabral, J. T. (2018). Microfluidic solvent extraction of poly(vinyl alcohol) droplets: effect of polymer structure on particle and capsule formation. *Soft Matter*, **14**(22), 4453–4463.

Shenoy, S. A., Chaithanya, K. V. S., and Dayal, P. (2025). Shear-induced dynamics of an active Belousov–Zhabotinsky droplet. *Soft Matter*, **21**(10), 1957–1969.

Shi, H., Zhu, Q., Chen, Z., … Wu, K. (2023). Pore-scale modeling of water–gas flow in heterogeneous porous media. *Physics of Fluids*, **35**(7).

Shih, S. C. C., Mufti, N. S., Chamberlain, M. D., Kim, J., and Wheeler, A. R. (2014). A droplet-based screen for wavelength-dependent lipid production in algae. *Energy and Environmental Science*, **7**(7), 2366–2375.

Silva, R. A., Assato, M., and De Lemos, M. J. S. (2016). Mathematical modeling and

numerical results of power-law fluid flow over a finite porous medium. *International Journal of Thermal Sciences*, **100**, 126–137.

Soares, S., Torres, K. G., Pimentel, E. L., Martelli, P. B., and Rocha, F. R. P. (2019). A novel spot test based on digital images for determination of methanol in biodiesel. *Talanta*, **195**(August 2018), 229–235.

Sochi, T. (2010a). Flow of non-newtonian fluids in porous media. *Journal of Polymer Science, Part B: Polymer Physics*, **48**(23), 2437–2767.

Sochi, T. (2010b). Non-Newtonian flow in porous media. *Polymer*, **51**(22), 5007–5023.

Spreinat, A., Kunz, W., Maack, C. H., Wilczek, C., Nestler, B., and Ernst, A. (2025). Fluid propagation and protein adsorption patterns in porous nitrocellulose membranes for lateral flow assays. *Physics of Fluids*, **37**(3), 32022.

Środek, D., and Dulski, M. (2025). Hydroxyl group dynamics in defernite: Raman spectroscopy studies. *Spectrochimica Acta - Part A: Molecular and Biomolecular Spectroscopy*, **326**(October 2024).

Steinik, C., Picchi, D., Lavalle, G., and Poesio, P. (2024). Capillary imbibition of shear-thinning fluids: From Lucas-Washburn to oscillatory regimes. *Phys. Rev. Fluids*, **9**(2), 23305.

Strong, E. F., Pezzulla, M., Gallaire, F., Reis, P., and Siconolfi, L. (2019). Hydrodynamic loading of perforated disks in creeping flows. *Phys. Rev. Fluids*, **4**(8), 84101.

Takahashi, S., and Kovscek, A. R. (2010). Spontaneous countercurrent imbibition and forced displacement characteristics of low-permeability, siliceous shale rocks. *Journal of Petroleum Science and Engineering*, **71**(1–2), 47–55.

Tan, B. L., Sarafis, V., Beattie, G. A. C., White, R., Darley, E. M., and Spooner-Hart, R. (2005). Localization and movement of mineral oil in plants by fluorescence and confocal microscopy. *Journal of Experimental Botany*, **56**(420), 2755–2763.

Tan, Y.-C., Cristini, V., and Lee, A. P. (2006). Monodispersed microfluidic droplet generation by shear focusing microfluidic device. *Sensors and Actuators B: Chemical*, **114**(1), 350–356.

Tan, Y.-C., and Lee, A. P. (2005). Microfluidic separation of satellite droplets as the basis of a monodispersed micron and submicron emulsification system. *Lab on a Chip*, **5**(10), 1178.

Tang, Y., Yao, X., Chen, Y., … Peng, Y. (2020). Experiment research on physical clogging mechanism in the porous media and its impact on permeability. *Granular Matter*, **22**(2), 37.

Tang, Y., Yuan, J., Zhang, Y., Khan, I. M., Ma, P., and Wang, Z. (2024). Lateral flow assays based on aptamers for food safety applications. *Food Control*, **155**(August 2023), 110051.

Tangen, U., Sharma, A., Wagler, P., and McCaskill, J. S. (2015). On demand nanoliter-scale microfluidic droplet generation, injection, and mixing using a passive microfluidic device. *Biomicrofluidics*, **9**(1).

Tokihiro, J. C., Tu, W., Berthier, J., … Berthier, E. (2023). Enhanced capillary pumping using open-channel capillary trees with integrated paper pads. *Physics of Fluids*, **35**(8).

Toley, B. J., Das, D., Ganar, K. A., … Soni, S. (2018). Multidimensional Paper Networks: A New Generation of Low-Cost Pump-Free Microfluidic Devices. *Journal of the Indian Institute of Science*, **98**(2), 103–136.

Tuller, M., and Or, D. (2004). Retention of water in soil and the soil water characteristic curve. *Encyclopedia of Soils in the Environment*, **4**, 278–289.

Uozumi, N., and Takahashi, S. (2023). Hyper-mobile Water and Raman 2900 cm − 1 Peak Band of Water Observed around Backbone Phosphates of Double Stranded DNA by High-Resolution Spectroscopies and MD Structural Feature Analysis of Water.

van den Broek, J., Bischof, D., Derron, N., … Pratsinis, S. E. (2021). Screening Methanol Poisoning with a Portable Breath Detector. *Analytical Chemistry*, **93**(2), 1170–1178.

van den Broek, J., Keller, S. D., Goodall, I., … Agapios, A. (2024). Handheld methanol detector for beverage analysis: interlaboratory validation. *Analytical Methods*, **16**(24), 3859–3866.

Van der Westhuizen, J., and Prieur Du Plessis, J. (1996). An attempt to quantify fibre bed permeability utilizing the phase average Navier-Stokes equation. *Composites Part A: Applied Science and Manufacturing*, **27**(4), 263–269.

van Genuchten, M. T. (1980). A Closed-form Equation for Predicting the Hydraulic Conductivity of Unsaturated Soils. *Soil Science Society of America Journal*, **44**(5), 892–898.

Vasheghani Farahani, M., and Mousavi Nezhad, M. (2022). On the effect of flow regime and pore structure on the flow signatures in porous media. *Physics of Fluids*, **34**(11).

Verma, S., and Toley, B. J. (2024). Saturation Equation: An Analytical Expression for Partial Saturation during Wicking Flow in Paper Microfluidic Channels. *Langmuir*, **40**(22), 11419–11427.

WADA, S., NISHIYAMA, N., and NISHIDA, S. (1985). Modified Darcy's Law for Non-

Newtonian Fluids. *Bulletin of JSME*, **28**(246), 3031–3037.

Wang, C., and Otani, Y. (2013). Removal of Nanoparticles from Gas Streams by Fibrous Filters: A Review. *Industrial and Engineering Chemistry Research*, **52**(1), 5–17.

Wang, H., Zhao, H., Guo, Z., and Zheng, C. (2012a). Numerical simulation of particle capture process of fibrous filters using Lattice Boltzmann two-phase flow model. *Powder Technology*, **227**, 111–122.

Wang, H., Zhao, H., Guo, Z., and Zheng, C. (2012b). Numerical simulation of particle capture process of fibrous filters using Lattice Boltzmann two-phase flow model. *Powder Technology*, **227**, 111–122.

Wang, S., Chinnasamy, T., Lifson, M., … Alto, P. (2017). Flexible substrate-based devices for point-of-care diagnostics, **34**(11), 909–921.

Wang, X., Zhang, A., Zhi, M., Sokolov, A. V, and Welch, G. R. (2010). Glucose concentration measured by the hybrid coherent anti-Stokes Raman-scattering technique, **013813**, 2–7.

Washburn, E. W. (1921). The Dynamics of Capillary Flow. *Physical Review*, **17**(3), 273–283.

Wei, J., Long, Y., Li, T., Gao, H., and Nie, Y. (2024). Exploring hydrogen-bond structures in cellulose during regeneration with anti-solvent through two-dimensional correlation infrared spectroscopy. *International Journal of Biological Macromolecules*, **267**, 131204.

Whitaker, S. (1986). Flow in porous media I: A theoretical derivation of Darcy's law. *Transport in Porous Media*, **1**(1), 3–25.

Wiśniewska, P., Śliwińska, M., Dymerski, T., Wardencki, W., and Namieśnik, J. (2015). The Analysis of Vodka: A Review Paper. *Food Analytical Methods*, **8**(8), 2000–2010.

Wong, R., and Tse, H. (2008). *Lateral Flow Immunoassay*, Humana Press. Retrieved from https://books.google.co.in/books?id=D4-capuCoRUC

Xi, Y., Frank, B. D., Tatas, A., Pavlovic, M., and Zeininger, L. (2023). Multicompartment calcium alginate microreactors to reduce substrate inhibition in enzyme cascade reactions. *Soft Matter*, **19**(39), 7541–7549.

Xia, Y., Si, J., and Li, Z. (2016). Fabrication techniques for microfluidic paper-based analytical devices and their applications for biological testing: A review. *Biosensors and Bioelectronics*, **77**, 774–789.

Xiong, H., Sun, G., Liu, Z., … Qiao, Z.-A. (2021). Polymer Stabilized Droplet Templating towards Tunable Hierarchical Porosity in Single Crystalline Na3V2(PO4)3 for

Enhanced Sodium-Ion Storage. *Angewandte Chemie International Edition*, **60**(18), 10334–10341.

Xu, P., and Yu, B. (2008). Developing a new form of permeability and Kozeny–Carman constant for homogeneous porous media by means of fractal geometry. *Advances in Water Resources*, **31**(1), 74–81.

Xu, W., Huang, H., Ke, S. Z., Li, J. P., Zhang, H. F., and Hu, Y. B. (2022). An integral method for calculation of capillary pressure based on centrifuge data of tight sandstone. *Petroleum Science*, **19**(1), 91–99.

Yadav, S., and Pathak, B. (2024). Dynamics of impact of polymer droplets on viscoelastic surfaces. *Experiments in Fluids*, **65**(10), 145.

Yager, P., Edwards, T., Fu, E., … Weigl, B. H. (2006). Microfluidic diagnostic technologies for global public health. *Nature*, **442**(7101), 412–418.

Yan, C., Fan, J., and Xu, C. (2013). Chapter 5 - Analysis of Oil Droplets in Microalgae. In H. Yang and P. B. T.-M. in C. B. Li, eds., *Lipid Droplets*, Vol. 116, Academic Press, pp. 71–82.

Yang, C., Huang, H., Liu, W., … Chen, L.-Q. (2021). Explicit Dynamics of Diffuse Interface in Phase-Field Model. *Advanced Theory and Simulations*, **4**(1), 2000162.

Yang, L., Wang, S., Tao, Z., Leng, R., and Yang, J. (2019). The characteristics of oil migration due to water imbibition in tight oil reservoirs. *Energies*, **12**(21). doi:10.3390/en12214199

Yobas, L., Martens, S., Ong, W.-L., and Ranganathan, N. (2006). High-performance flow-focusing geometry for spontaneous generation of monodispersed droplets. *Lab on a Chip*, **6**(8), 1073.

YUE, P., ZHOU, C., and FENG, J. J. (2010). Sharp-interface limit of the Cahn–Hilliard model for moving contact lines. *Journal of Fluid Mechanics*, **645**, 279–294.

Zamani, N., Rafizadeh, A., Hassanian-Moghaddam, H., … Shariati, S. (2019). Evaluation of methanol content of illegal beverages using GC and an easier modified Chromotropic acid method; A cross sectional study. *Substance Abuse: Treatment, Prevention, and Policy*, **14**(1), 1–7.

Zec, H., Shin, D. J., and Wang, T.-H. (2014). Novel droplet platforms for the detection of disease biomarkers. *Expert Review of Molecular Diagnostics*, **14**(7), 787–801.

Zhang, Y., Liu, H., Nakagawa, Y., … Li, M. (2024). Enhanced CRISPR/Cas12a-based quantitative detection of nucleic acids using double emulsion droplets. *Biosensors and Bioelectronics*, **257**, 116339.

Zhao, C., Zholkovskij, E., Masliyah, J. H., and Yang, C. (2008). Analysis of electroosmotic flow of power-law fluids in a slit microchannel. *Journal of Colloid and Interface Science*, **326**(2), 503–510.

PUBLICATIONS FROM THE PRESENT THESIS

1. **Behera, P. P.,** Mehta, S. K., Arun, R. K., and Mondal, P. K. (2023). Solute imbibition in paper strip: Pore-scale insights into the concentration-dependent permeability. Physics of Fluids, 35 (12): 122007.
2. **Behera, P. P.**, Mehta, S. K., Arun, R. K., and Mondal, P. K. (2025). Pore-scale immiscible interfacial transport facilitates low-cost droplet generation. Soft Matter, 21(35), 6891–6909.
3. **Behera, P. P.**, Mehta, S. K., Arun, R. K., and Mondal, P. K. (2026). Liquid Imbibition in Paper Pathways: Rheology-Analyte Coupling Insights. Physics of Fluids, 38 (1): 012105. https://doi.org/10.1063/5.0305401
4. **Behera, P. P.**, Mehta, S. K., Agarwal, K., Bera, S., Arun, R. K., and Mondal, P. K. (2024). Paper-based lateral flow assays: Prediction of methanol content in alcoholic beverages. Physics of Fluids, 36(12), 123619.

Review paper:

5. **Behera, P. P.**, Kumar, N., Kumari, M., Kumar, S., Mondal, P. K., and Arun, R. K. (2023a). Integrated microfluidic devices for point-of-care detection of bio-analytes and disease. Sensor and Diagnostic, 2(6), 1437–1459.

Other Publications:

6. Mehta, S. K., **Behera, P. P.**, Dutta, A. and Mondal, P. K. (2025). Ion-partitioning effect promotes the electroosmotic mixing of non-Newtonian fluids in soft-patterned microchannels. Physical Chemistry Chemical Physics, 27(37), 19662–19676.